

MASTER OF SCIENCE THESIS

---

Jensen-Gaussian wake model extension  
considering the Atmospheric Boundary  
Layer effects for the Wind Farm Layout  
Optimization

A.A. Habiboella

---

03-04-2019

Faculty of Aerospace Engineering · Delft University of Technology



# Jensen-Gaussian wake model extension considering the Atmospheric Boundary Layer effects for the Wind Farm Layout Optimization

MASTER OF SCIENCE THESIS

For obtaining the degree of Master of Science in Aerospace  
Engineering at Delft University of Technology

A.A. Habiboella

03-04-2019



Copyright © A.A. Habiboella  
All rights reserved.

DELFT UNIVERSITY OF TECHNOLOGY  
DEPARTMENT OF  
AERODYNAMICS AND WIND ENERGY

The undersigned hereby certify that they have read and recommend to the Faculty of Aerospace Engineering for acceptance a thesis entitled “**Jensen-Gaussian wake model extension considering the Atmospheric Boundary Layer effects for the Wind Farm Layout Optimization**” by **A.A. Habiboella** in partial fulfillment of the requirements for the degree of **Master of Science**.

Dated: 03-04-2019

Head of department:

\_\_\_\_\_  
Dr.ir. M.I. Gerritsma

Supervisor:

\_\_\_\_\_  
Dr. ir. A.H. van Zuijlen

Reader:

\_\_\_\_\_  
S.M. Kaja Kamaludeen, MSc

Reader:

\_\_\_\_\_  
Dr.ir. C.J. Simao Ferreira



---

# Acknowledgements

This report is an acknowledgement of my efforts to obtain my Master of Science (MSc) degree in Aerodynamics at the Delft University of Technology. This thesis is about the influence of the Atmospheric Boundary Layer (ABL) on the turbine wake development and how it affects the Wind Farm Layout Optimization (WFLO). I went through a roller-coaster ride during this period and I would like to express my gratitude to those whom supported and encouraged to finish my thesis and obtain my MSc. degree.

Firstly, I would like to thank my daily supervisors dr. ir. A.H. van Zuijlen and MSc. S.M. Kaja Kamaludeen. Shaafi took it upon him to help and support me a lot with the cumbersome open software openFOAM and SOWFA. Sharing his cluster nodes with me and helping me through the simulation results. While dr. ir. A.H. van Zuijlen gave constructive suggestions to help further my research on the wake analysis, to improve my analysis and overcome certain programming issues. I would also like to thank the readers Dr.ir. M.I. Gerritsma and Dr.ir. C.J. Simao Ferreira for being in my committee and going through my thesis report. Important for me is to thank all of my friends that have always believed in me. Starting with the colleagues I met at the Delft University; Nabil, Talha, Hamza Ibrahim, Serhat, Qais and Yama. My childhood friends; Ashraf, Aziz, Hamid, Mohammed, Naima and Younes. And my friends from the Islamic Student Association; Hicham, Musa, Mutahar, Othman and especially Zubair.

Finally, I would like to thank my family. Starting with my brother and sister, Satisch and Sahira. My fiancée Rashana Hussain, whom supported me in the final steps of this thesis. But most importantly, my mom. She is the most important factor throughout my life, words will never describe the time, energy and effort she has put into me. May Allah grant you Jannat Firdaws.



---

# Abstract

To increase the total wind farm power output, the wind farm layout needs to be optimized. The power output of a wind turbine depends on the incoming velocity, while the velocity is influenced by the wake of the upstream wind turbines. Wind Farm Layout Optimization (WFLO) problems makes use of the so called low fidelity wake models, which predict the velocity downstream of a turbine. The analytical Jensen wake model with a top hat velocity wake profile is commonly used to perform the WFLO during the preliminary design phase of a wind farm. However a top hat velocity profile is not an accurate depiction of the actual velocity profile downstream of the turbine wake. To get a more accurate wake profile the model needs to be extended. To improve the wake model, the role of the stability of the Atmospheric Boundary Layer (ABL) on the development of the turbine wake is analyzed using the software openFOAM and SOWFA.

It is noticed that the analytical Jensen-Gaussian wake model is in better agreement with measurement data than the Jensen top hat wake model. It is verified that it is necessary to include the added Turbulence Intensity (T.I) induced by the wind turbine. For the Jensen-Gaussian wake model, the Gao turbulence model gives results that are in good agreement with the experimental data. The Jensen-Gaussian wake model is extended to be used inside a wind farm with multiple wakes. The power output for a row of 10 Vestas V-80 turbines in the Horns rev Wind farm is computed. Using the equivalent velocity by weighted area averaging over a discretized wake turbine-cross section in combination with the power curve, the power output of a turbine can be computed. Using the energy superposition method the equivalent velocity for aligned turbines can be computed. Comparison with measurement data shows that there still is a difference between the results from the wake model and the measurement data.

To further improve the Jensen-Gaussian wake model it is important to take into account the effect of the stability of the ABL on the wake. The different stabilities for an offshore ABL are simulated with SOWFA and the turbine wakes are computed. The different wake recovery rates and elliptical shapes due to the stability of the ABL are included in the extended model.

Using the offshore Horns rev wind farm data, the extended Jensen-Gaussian model in combination with the mixed-discrete Particle Swarm Optimization (MDPSO), the WFLO

is carried out. The WFLO predicts that it is important to take the stability of the different models into account. However it is concluded that the improvement cannot be quantified, due to the uncertainties in the computation in the power output of each wind turbine.

---

# Contents

<b>Acknowledgements</b>	<b>v</b>
<b>Abstract</b>	<b>vii</b>
<b>List of Figures</b>	<b>xiii</b>
<b>List of Tables</b>	<b>xv</b>
<b>Nomenclature</b>	<b>xvii</b>
<b>1 Introduction</b>	<b>1</b>
1.1 Background . . . . .	1
1.2 Motivation of the study . . . . .	1
<b>2 Literature Review</b>	<b>5</b>
2.1 Turbine Wake . . . . .	5
2.2 Atmospheric Boundary Layer . . . . .	6
2.3 Wake Meandering . . . . .	7
2.3.1 Wake meandering according to Ainslie . . . . .	7
2.4 Turbine wake models . . . . .	8
2.4.1 CFD Models . . . . .	9
2.4.2 Field models . . . . .	9
2.4.3 Ainslie . . . . .	9
2.4.4 Kinematic models . . . . .	11
2.4.5 Jensen . . . . .	11
2.4.6 Larsen model . . . . .	13
2.4.7 Frandsen Model . . . . .	14
2.4.8 Bastankhah and Porté-Agel Model . . . . .	16
2.4.9 Jensen-Gaussian . . . . .	18
2.5 Wind farm layout optimization . . . . .	20
2.5.1 The objective function . . . . .	20
2.5.2 Energy calculation of the wind farm . . . . .	20

<b>3</b>	<b>Validation Jensen-Gaussian Model</b>	<b>23</b>
3.1	Selected Wake model . . . . .	23
3.2	Single wake validation . . . . .	23
3.3	Turbulence intensity models . . . . .	24
3.4	Conclusion . . . . .	27
<b>4</b>	<b>Wind farm validation</b>	<b>29</b>
4.1	Wake summation . . . . .	29
4.1.1	Linear summation . . . . .	29
4.1.2	Root Sum of Squares . . . . .	30
4.2	The equivalent incoming wind velocity . . . . .	30
4.2.1	Rotor discretization . . . . .	30
4.2.2	Computation of the equivalent velocity . . . . .	31
4.3	Horns Rev Wind farm . . . . .	31
4.3.1	Velocity deficit superposition . . . . .	32
4.3.2	Energy deficit superposition . . . . .	33
4.3.3	T.I. validation . . . . .	33
4.4	Conclusion . . . . .	34
<b>5</b>	<b>SOWFA Large Eddy Simulation</b>	<b>39</b>
5.1	openFOAM . . . . .	39
5.2	SOWFA . . . . .	39
5.2.1	Governing equations . . . . .	40
5.3	Uniform flow . . . . .	41
5.3.1	Case setup . . . . .	41
5.3.2	Results . . . . .	42
5.4	ABL . . . . .	43
5.4.1	Precursor setup . . . . .	43
5.4.2	Validation ABL precursor . . . . .	46
5.4.3	Wind turbine case setup . . . . .	54
5.4.4	Turbine wake analysis . . . . .	55
5.5	Conclusion . . . . .	64
<b>6</b>	<b>Wind Farm Layout Optimization</b>	<b>65</b>
6.1	Optimization algorithm . . . . .	65
6.2	Results optimization: Horns REV OWF . . . . .	67
6.3	Conclusion . . . . .	68
<b>7</b>	<b>Conclusion</b>	<b>71</b>
7.1	Conclusions . . . . .	71
7.2	Recommendations for future work . . . . .	72
	<b>References</b>	<b>73</b>
<b>A</b>	<b>NREL-5MW</b>	<b>77</b>
<b>B</b>	<b>Flowchart: Optimization algorithm</b>	<b>79</b>

---

# List of Figures

2.1	Wake meandering effect [30]	8
2.2	Wake velocity [m/s] for single turbine computed with the Ainslie model (Eddy viscosity Model) [41]	10
2.3	The control volume for the Jensen wake model [26]	12
2.4	Wake velocity [m/s] for single turbine computed with the Jensen-Katic model [41]	13
2.5	Wake velocity [m/s] for single turbine computed with the Larsen model [41]	14
2.6	The cylindrical control volume that is considered for the Frandsen model [16]	15
2.7	Wake velocity [m/s] for single turbine computed with the Frandsen model [36]	16
2.8	Wake velocity [m/s] for single turbine computed with the BP model [24]	17
2.9	Left Jensen with top hat velocity profile, Right Jensen with Gaussian distributed velocity profile [19]	18
2.10	Wake velocity [m/s] for single turbine computed with the Jensen-Gaussian model	19
3.1	Comparison between the windtunnel measurements and wake models at 2.5D downstream	24
3.2	Comparison between the windtunnel measurements and wake models at 5D downstream	25
3.3	Comparison between the windtunnel measurements and wake models at 7.5D downstream	25
3.4	Comparison between the windtunnel measurements and wake models at 10D downstream	26
3.5	Comparison between the Nibe site measurements and Jensen-Gaussian with different turbulence models at 4.5D downstream	27
3.6	Comparison between the Nibe site measurements and Jensen-Gaussian with different turbulence models at 7.5D downstream	28
4.1	Discretized wake cross section using $N_r = 40$ and $N_t = 100$	31

4.2	Vestas V-80 $C_t - U$ curve, dashed lines represent the cut-in and rated velocity	32
4.3	Vestas V-80 $P - U$ curve, dashed lines represent the cut-in and rated velocity	33
4.4	Horns Rev offshore wind farm layout, consisting of 40 Vestas V80-2MW wind turbines [32]	34
4.5	Horns Rev wind farm case: Normalized power obtained from LES compared with the computations acquired from the Jensen-Gaussian wake model, with Gao's turbulence model and relative velocity superposition method	35
4.6	Horns Rev wind farm case: Normalized power obtained from LES compared with the computations acquired from the Jensen-Gaussian wake model, with Gao's turbulence model and relative energy superposition method	35
4.7	Horns Rev wind farm case: Turbulence intensity obtained from LES compared with Gao's turbulence model	36
4.8	Horns Rev wind farm case: Normalized power obtained from LES compared with the computations acquired from the Jensen-Gaussian wake model, with Frandsens turbulence model and relative energy superposition method	37
4.9	Horns Rev wind farm case: Turbulence intensity obtained from LES compared with Frandsens turbulence model	37
4.10	Horns Rev wind farm case: Normalized power obtained from LES compared with Gao and Frandsens turbulence model with the same matching T.I.	38
4.11	HornsRev wind farm case: Artificially subtracted 1% T.I of Gao's turbulence model and added 3.8% to Frandsens turbulence model	38
5.1	Comparison between SOWFA and Jensen-Gaussian wake model, top is 4D downstream and middle is 7D downstream and bottom is 10D. The dashed line is the turbine location	44
5.2	Predefined profiles by SOWFA, the dashed lines represent the upper and lower blade tip	45
5.3	Comparison between SOWFA and Akbar and Porté-Agel's results	47
5.4	The velocity at half the boundary layer height varying with time	48
5.5	Temperature profile based upon the boundary depth and logarithmic velocity profile, the dashed lines represent the upper and lower blade tip	49
5.6	Comparison between SOWFA's and Akbar & Porté-Agal ABL precursors.	50
5.7	Neutral ABL: Law of the wall comparison with SOWFA cases with varying $\delta$	51
5.8	Unstable ABL: Temperature profile by reducing initial temperature	51
5.9	Unstable ABL: Velocity profile by reducing initial temperature and increasing boundary layer height	52
5.10	Comparison between SOWFA's and Akbar & Porté-Agal ABL turbulence intensity	53
5.11	Stable case: Temperature and velocity profile using temperature flux as b.c.	54
5.12	Results of the precursor simulation for the three stability cases	56
5.13	Time-averaged streamwise velocity component in the x - z plane.	57
5.14	Time-averaged streamwise velocity component in the x - z plane.	58
5.15	Comparison of the normalized time-averaged streamwise velocity deficit 4D downstream, between SOWFA and the extended Jensen-Gaussian wake model.	59
5.16	Comparison of the normalized time-averaged streamwise velocity deficit 7D downstream, between SOWFA and the extended Jensen-Gaussian wake model.	60

---

5.17	Velocity profile for the stability conditions based upon the power law . . .	61
5.18	Curve fits for $\alpha$ vs the extended Jensen-Gaussian elliptical wake parameters	63
6.1	NREL-5MW power curve: $P - U$ , where the dashed lines represent the cut-in speed and rated speed. . . . .	66
6.2	Annual wind speeds for different wind direction in Horns Rev . . . . .	67
6.3	The annual percentages for each wind sector in Horns Rev . . . . .	68
6.4	Optimal layout for the different stability wake models . . . . .	69
A.1	. . . . .	77
A.2	. . . . .	77
B.1	. . . . .	80



---

# List of Tables

2.1	Initial conditions used to compute the wake velocity downstream . . . . .	19
3.1	Initial conditions used to compute the wake velocity downstream for the Garrad Hassan windtunnel . . . . .	24
3.2	Initial conditions Nibe site . . . . .	28
5.1	NREL 5-MW turbine specifications . . . . .	41
5.2	Initial conditions Uniform flow . . . . .	43
5.3	Initial parameters used solve the ABL . . . . .	45
5.4	Initial parameters for precursor simulation . . . . .	55
5.5	Initial conditions for each stability conditions . . . . .	62
5.6	Initial parameters used to compute the turbine wake according to the extended Jensen-Gaussian elliptical wake model . . . . .	62
6.1	Wind farm power output [ $kW \cdot 10^6$ ] . . . . .	68
6.2	Wind farm power output percentage difference % . . . . .	69



---

# Nomenclature

## Latin Symbols

$A$	Wake cross-sectional area	$[m^2]$
$a$	Axial induction factor	$[-]$
$C_T$	Thrust coefficient	$[-]$
$D$	Diameter of a wind turbine	$[m]$
$I$	Turbulence Intensity	$[-]$
$k$	Wake growth rate	$[-]$
$P$	Power	$[W]$
$p$	Pressure	$[N/m^2]$
$q$	Temperature flux	$[K/m^2/s]$
$r$	Radial coordinate	$[m]$
$r$	Radius of a wind turbine	$[m]$
$T$	Period of meandering motion	$[s]$
$T$	Thrust force	$[N]$
$U$	Downstream velocity	$[m/s]$
$V$	Radial velocity	$[m/s]$
$V$	Spanwise velocity	$[m/s]$
$W$	Vertical velocity	$[m/s]$
$x$	Downstream distance	$[m]$
$y$	Spanwise distance	$[m]$
$z$	Vertical distance	$[m]$

---

$z_0$	Roughness length	[ $m$ ]
-------	------------------	---------

## Greek Symbols

$\alpha$	Power law coefficient	[–]
$\alpha$	Wake decay coefficient	[–]
$\Delta$	Difference in variable	[–]
$\delta$	Boundary layer height	[ $m$ ]
$\kappa$	Von Karman Constant	[–]
$\omega$	Planetary rotation rate	[ $rad/s$ ]
$\phi$	Latitude	[°]
$\psi$	Atmospheric Stability Factor	[–]
$\rho$	Density	[ $kg/m^3$ ]
$\sigma$	Standard deviation	[–]
$\theta$	Potential temperature	[ $K$ ]
$\theta$	Wind direction	[°]
$g$	Gravitational constant	[ $m/s^2$ ]

## Subscripts

0	Initial condition
$\infty$	Free stream condition
<i>ad</i>	Advection
<i>a</i>	Ambient
<i>in</i>	Cut in
<i>out</i>	Cut out
<i>w</i>	Wake
<i>w</i>	Wall

## Superscripts

'	Subfiltered quantity
–	Mean quantity

---

# Chapter 1

---

## Introduction

### 1.1 Background

In a world with depleting energy resources and rising global temperature there is a need for new sustainable energy generation. One of the available options, is the installation of large offshore wind turbine farms. In recent years wind turbine farms have grown, however so has the demand for more efficient wind farms. Due to the fact that wind turbines are positioned relatively close to each other, the wind turbine wakes will influence the performance of turbines downstream in its wake. This results in significant power losses, up to 40% for a single wind turbine [38], due to reduced incoming wind speed for downstream wind turbines. When wind speeds are averaged over different wind directions, power losses up to 10-20% are measured [5]. Another effect of turbines inside a wake, is the reduced lifetime of the rotors due to increased unsteady loading, which is a consequence of the increased turbulence intensity.

As a consequence of these two major effects, wake losses and rotor lifetime, the layout of the wind turbines in the farm need to be optimized for power and/or cost. Changing the layout of the wind turbines can increase/reduce the effects of the multiple wakes on the wind turbine, but at the same time it could increase/decrease the electrical cable lengths. Increased cable lengths increase ohmic losses, cables costs and cables installation costs. All these factors need to be taken in consideration when designing the optimal wind farm layout.

### 1.2 Motivation of the study

The aerodynamic flow in the wind farm can be computed by solving the full or filtered Navier-Stokes equations. The Navier-stokes equations can be solved with Computational Fluid Dynamic (CFD) models. There are a number of different CFD models with varying complexity depending on the assumptions made. It is considered that with these models accurate simulation results can be acquired, that are in good agreement with experimental

results. However, the CFD models require a lot of computational resources and time, due to their complexity. To this end low fidelity turbine wake models are used to compute the velocity profile in the downstream wake. Using these low fidelity models however results in the loss of accuracy in predicting the wake velocity and consequently loss in efficiency when designing the wind farm layout. Therefore it is proposed to extend a low fidelity wake model, by analyzing significant physical phenomena that occurs at a wind farm. This is achieved by running simulations with CFD software, such as Open Source Field Operation and Manipulation (openFOAM) and Simulator for Wind Farm Applications (SOWFA), and comparing the results with the low fidelity model. Afterwards ways should be found to include the physics in the low fidelity model. In this way the relatively low computational time is preserved while supposedly adding accuracy to the wake model. It should be noted that after modification of the wake model, the efficiency of the wind farm does not necessarily improve. This is the case for the Jensen and modified FLORIS model, where due to chosen optimization technique, the unmodified Jensen model still gave the better solution [42].

This master thesis will answer the following research question: "*Which wind Farm flow field physics are dominant and can improve the accuracy of the low fidelity model by considering the dominant physical phenomena at minimal computational cost to increase the wind farm's power output through better optimization of the wind farm layout?*"

In order to answer the research questions the following sub-goals were set:

1. Perform a literature study in which we identify:
  - (a) The physics involving the wake development inside a wind farm
  - (b) The different available wind turbine models
  - (c) The application of these different wind turbine models in a wind farm
  - (d) The layout optimization for the wind farm
2. Program and validate the low fidelity wake model for a single turbine
3. Extend the wake model for the application in a wind farm
4. Run simulation of SOWFA and compare results obtained from the wake model
5. Identify and implement dominant wind farm physics in the low fidelity model
6. Perform a wind farm layout optimization with the modified low fidelity model and the original model and compare the power output.

The study performed to tackle this problem is presented in this report. First in chapter 2 the literature study performed on wind turbine farms will be reviewed. Secondly in chapter 3, the chosen wake model is programmed, implemented and validated. Thirdly in chapter 4 the wind turbine wake model is extended, such that it is suitable to be used in a wind farm. In chapter 5 the software openFOAM and SOWFA are used to compute the turbine wake. First precursor simulations are performed and validated to compute the Atmospheric Boundary Layer. And afterwards the turbine wake is computed by using

Large Eddy Simulations (LES) with the Actuator Line Model (ALM). Important physics will be identified and the chosen analytical wake model is extended to incorporate these effects. Finally in chapter 6, the wind farm layout optimization is performed with the original wake model and extended wake model and the results are compared. In chapter 7 the results and conclusions of this thesis are discussed.



# Literature Review

In order to answer the research question a literature study was performed and is presented in this chapter. The following learning goals were set to be obtained from the literature review: Identifying dominant flow physics or phenomena that influence the development of the wind turbine wake, learn about the different available wind turbine wake models and find appropriate wind farm layout optimization techniques. In section 2.1 the wake characteristics will be discussed. In section 2.2 - 2.3, the wind farm physics that play a role in the development of the wake will be discussed. In section 2.4, the different available wind wake models will be discussed. Finally in section 2.5 the layout optimization is described.

## 2.1 Turbine Wake

After the wind energy is extracted by the wind turbine, the wind becomes turbulent and has reduced wind speed. This trail of turbulent and reduced wind speeds is called the wind turbine wake. This wake influences the performance of the downstream turbines.

The wake can be divided into two regions: Near and far wake [37]. The near wake is the region just behind the wind turbine, this extends to approximately 2-4 rotor diameters downstream [15]. Here the turbine geometry determines the shape of the flow field and determines the performance of the turbine. The presence of the rotor is apparent by the number of blades, blade aerodynamics, including stalled flow, 3-d effects and tip vortices.

The far wake starts at the location where the tip vortex breaks down in the near wake. This region has the biggest influence on wind turbines in a farm. The far wake is the region of interest for this thesis, here the focus will be put on. In the far wake there are two main mechanisms determining the wake development, convection and turbulent diffusion [44]. It is expected that far enough downstream the momentum deficit and increased turbulence will vanish because of turbulent diffusion of the wake. From measurements from wind farms and experimental setups it is concluded, that in the far wake both the velocity deficit profile and turbulence intensity profile are axi-symmetric and have self

similar distributions in the cross-section of the wake [44]. This property of self-similarity is the basis of the kinematic models describing wind turbine wakes.

For both these regions the velocity deficit can be computed with different models and techniques. However since the far region is of most importance we will discuss the physical properties that influence the flow field in this region.

## 2.2 Atmospheric Boundary Layer

To compute the velocity deficit by means of the wake models, certain initial conditions are required. Such as the velocity profile of in the incoming flow over the turbine and the ambient Turbulence Intensity (T.I.).

The wind turbine operates in the lowest part of the atmospheric boundary. This means that the atmospheric properties influences the wind turbine wake. One of these important aspects is the velocity profile of the Atmospheric Boundary Layer (ABL). The Atmospheric Boundary Layer can be computed numerically for example with SOWFA. It can also be modeled by either a logarithmic profile or the power law, however the latter has no theoretical background unlike the logarithmic. The logarithmic velocity profile is as follows:

$$\bar{u}(z) = u^* (\ln(z/z_0) + \psi) / \kappa. \quad (2.1)$$

where  $\bar{u}$  is the mean wind speed,  $z$  the height,  $z_0$  the surface roughness length,  $\psi$  a factor that depends on the atmospheric stability and  $\kappa$  the von Karman constant (0.4). The atmospheric stability plays an important role on the shape of the velocity profile. Stable ABL have a larger velocity gradient w.r.t. height, than an unstable ABL which has a more uniform shape.

For the power law the following approximation is given:

$$\bar{u}(z) = \bar{u}(H) \left( \frac{z}{H} \right)^\alpha, \quad (2.2)$$

where  $\alpha$  is either 0.14 or between 0.1-0.25 [22]. And  $\bar{u}(H)$  is the given mean wind speed at hub height.

The stability of the ABL was also a parameter in equation 2.1. The stability of the ABL depends on the rate of change in temperature with height, also called the lapse rate, and is compared with the adiabatic lapse rate. There are 3 states: Unstable, stable and neutral. The ABL is unstable when  $\frac{dT}{dz} < (\frac{dT}{dz})_{ad}$ , stable when  $\frac{dT}{dz} > (\frac{dT}{dz})_{ad}$  and neutral if  $\frac{dT}{dz} = (\frac{dT}{dz})_{ad}$ . When the ABL is unsteady this will result in large scale turbulent eddies and a thick boundary layer.

With these factors the Turbulence Intensity (T.I.) of the ABL can be computed, which is defined as:

$$I = \frac{\sigma}{\bar{u}}, \quad (2.3)$$

where  $I$  is the turbulence intensity,  $\sigma$  is the standard deviation of the wind velocity and  $\bar{u}$  is the average wind velocity. There are also analytical models to compute the atmospheric turbulence, such Mann's model [13] or Panofsky and Dutton's model. Ambient turbulence intensity plays a role in the turbulent mixing and velocity profile recovery in the wake.

Higher ambient turbulence will lead to faster wake recovery. This can be clearly seen when comparing off-shore wind farms with on-shore. Offshore Wind Farms (OWF) have more persistent wakes, because of the lower ambient turbulence. It can be concluded that the ABLs velocity profile and ambient Turbulence Intensity play an important role in the development of the turbine wake. First is that the T.I. plays a role in the rate of the recovery of the wake. When a wake recovers faster, wind turbines can be positioned relatively closer to each other. Faster wake recovery also leads to an increase in the wind farm power production. However, higher T.I. also leads to higher unsteady loading of the wind turbine blades, resulting in earlier failure due to fatigue.

## 2.3 Wake Meandering

When considering the kinematic wake models, it can be noticed that the wake models do not consider meandering nor yawing of the wake. According to Sanderse B. [37], yawing will cause the wake downstream to become skewed. This means that the downstream wake is not symmetrical with the turbine axis anymore. However the kinematic wake models are modelled with the assumption that the velocity profile is symmetrical with the turbine axis and self similar. During the thesis the assumption will be made that the wind turbine is exactly aligned with the direction of the flow, thus eliminating the effect of yawing.

It is said that due to relatively large eddies in the atmosphere the wake is to move in its entirety, this motion is greatly influenced by the atmospheric stability [1]. This motion is called wake meandering and has great influence on wind turbines in a wind farm. This motion can cause a downstream wind turbine to be partially merged in a wake. One of the consequences is that the wind turbines have significant change in loads on the blade. However another consequence in wind farms is that wake meandering can lead to increased recovery of the wake.

### 2.3.1 Wake meandering according to Ainslie

Meandering is considered to be a time dependant phenomenon, see figure 2.1, however Ainslie [3] developed a correction for the original Ainslie model which is time independent. The meandering of the wake was considered to be a fluctuation of the centerline of the wake. For a fixed observer point on the turbine hub height, the period T can be computed, which is the air travelling time from turbine to this observer point.

$$T = \frac{x}{U_w}. \quad (2.4)$$

The observer point is assumed to sample the centerline of the wake with a Gaussian probability distribution:

$$p(r) = \frac{1}{\sqrt{2\pi}r_0} e^{-(r^2/2r_0^2)}, \quad (2.5)$$

and remembering that the velocity deficit profile for the Ainslie model was as follow:

$$d(r) = d_0 \cdot e^{-3.56(r/b)^2}, \quad (2.6)$$

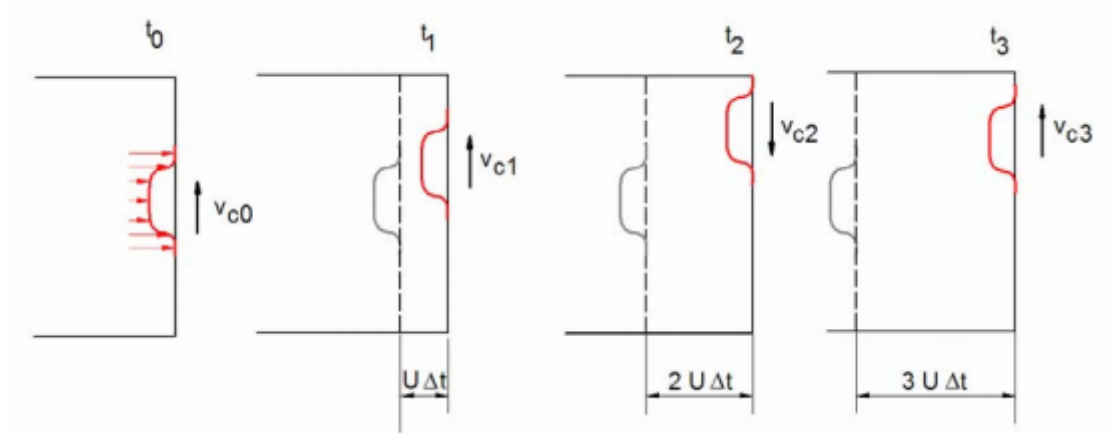


**Figure 2.1:** Wake meandering effect [30]

where  $r$  is the radial coordinate,  $d_0$  is the normalized velocity deficit at the centerline of the wake,  $d(r)$  is the velocity deficit in the wake normalized to the free stream velocity,  $r_0$  is the standard deviation of the wake centerline displacement and  $b$  the half width radius of the wake. The effective velocity deficit at the fixed observer point is considered to be the average over the period  $T$ . From these expressions the effective velocity deficit at the observer point can be computed with the following expression:

$$\begin{aligned} \hat{d} &= \int_{-\infty}^{\infty} d(r) \cdot p(r) dr \\ &= [1 + 7.12(r_0/b)^2]^{-1/2}, \end{aligned} \quad (2.7)$$

where  $r_0$  can be approximated, when assuming that the standard deviation of wind direction fluctuation  $\sigma_\theta$  is dominated by time scale not much less than the period, with the following expression:

$$r_0 \approx x\sigma_\theta, \quad (2.8)$$

where  $\sigma_\theta$  needs to be determined from field measurements.

Besides the Ainslie's meandering correction, also a Dynamic Wake Meandering (DWM) model is available, since this model is time dependant it will increase the computational time of the wind farm. However B. Hu [24] performed a study researching the effect of the DWM model on the power output of a wind farm. From his study he concluded that the DWM model had no significant effect on the annual output of a wind farm. He also mentioned that DMW is computationally expensive and not suitable for wind farm layout optimization. Therefore it is concluded to not include the wake meandering in this thesis.

## 2.4 Turbine wake models

The flow field behind wind turbines has been a topic for a long time. The modelling techniques used over the course of time differ a lot. In this chapter the different models that are available will be discussed. The models can be separated into three categories:

The CFD models, Field models and the Kinematic models. Where the CFD models are usually the highest fidelity models and the Kinematic the lowest fidelity models.

### 2.4.1 CFD Models

There are different type of CFD models available. The most known models are the Direct Numerical simulation (DNS), Reynolds Averaged Navier-Stokes, Large-Eddy Simulation (LES) and Detached Eddy Simulation (DES). However it is known that these models have high computational costs, e.g. LES can take up to several weeks to compute solutions. There have been attempts to use CFD models with decreased computational times. One of these CFD models is the FUGA model. According to [39], this model mimics the full CFD model behaviour very well in regions where perturbations are small and it does this  $10^4$  to  $10^5$  faster than the corresponding CFD model. It also gives reasonable momentum deficits in the far field. However, none of the CFD models, not even FUGA, will be feasible for the WFLOP. These models require a lot of computational resources and time to compute the flow field for a wind farm, which are not available. These computations have to be iterated to find the optimal layout, meaning that for this project the CFD models will not be taken into consideration for optimizing the wind farm layout.

### 2.4.2 Field models

The field models are of lower fidelity when compared to the CFD models. The field models are based upon approximations of the Navier-Stokes equations, such as the Ainslie model [4]. These differential equations need to be solved numerically at each point of the chosen mesh. This means it also requires a certain amount of computational power, however this is still less than for the CFD models.

### 2.4.3 Ainslie

Ainslie model is based upon Navier-Stokes equations [4], which is simplified with the following assumptions: The wake is assumed to be axisymmetric, fully turbulent, wake flow with zero circumferential velocities (since swirl is small) and the flow field will be assumed to be stationary with time. Also the pressure gradients in the co-flowing field outside of the wake is assumed to be negligible. The Navier-Stokes equation will be replaced with its equivalent thin shear layer approximation, with the viscous term dropped, the following equation is derived:

$$U \frac{\partial U}{\partial x} + V \frac{\partial U}{\partial r} = -\frac{1}{r} \frac{\partial (r\overline{uv})}{\partial r}, \quad (2.9)$$

where  $U$  and  $V$  are respectively the axial and radial velocity. Also  $x$  is the distance in the axial direction and  $r$  the coordinate in the radial direction, where the origin of both axis are at the turbine wake center. The turbulent viscosity concept is used to describe the Reynolds averaged shear stresses with an eddy viscosity as following:

$$-\overline{uv} = \varepsilon \frac{\partial U}{\partial r}. \quad (2.10)$$

Inserting equation 2.10 into equation 2.9, the following equation is derived:

$$U \frac{\partial U}{\partial x} + V \frac{\partial U}{\partial r} = \frac{\varepsilon}{r} \left( \frac{\partial U}{\partial r} + r \frac{\partial^2 U}{\partial r^2} \right). \quad (2.11)$$

When combining Equation 2.11 with the continuity equation 2.12, the solution for the unknowns  $U$  and  $V$  can be computed.

$$\frac{\partial U}{\partial x} = -\frac{1}{r} \left( r \frac{\partial V}{\partial r} + V \right) \quad (2.12)$$

Equations 2.11 and 2.12 are not solely restricted to the Ainslie model but they are the governing equation to many field models, they are referred to as eddy viscosity models (EVMod). The major difference between these field models is the way the eddy viscosity  $\varepsilon$  is modelled. Ainslie [4] described the eddy viscosity with the following equation:

$$\varepsilon = l_w(x) \cdot U_w(x) + \varepsilon_a, \quad (2.13)$$

where  $l_w$  and  $U_w$  are respectively the suitable length and velocity scales that describe the wake shear layer. Here  $\varepsilon_a$  is the ambient turbulence contribution to the eddy viscosity. For these equations no analytical solution is available thus it had to be solved numerically. The necessary inputs to solve the equation are the initial velocity deficit  $D_M$  and wake width  $b$ . The solution was envisaged to start at distance of 2 diameters downstream of the rotor, because the assumption was made that at that distance the pressure gradients no longer dominate the flow. For the initial velocity deficit a Gaussian profile is used.

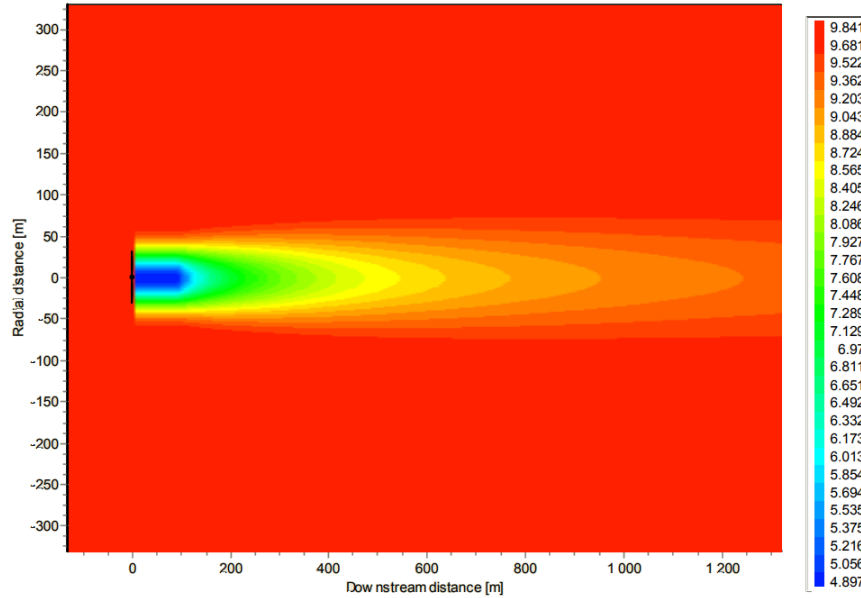


**Figure 2.2:** Wake velocity [m/s] for single turbine computed with the Ainslie model (Eddy viscosity Model) [41]

The solution for this model shows that the velocity deficit profile is self-similar, this can be seen in figure 2.2. So along the axial direction the initial Gaussian velocity profile is retained and only the depth and width changes.

### 2.4.4 Kinematic models

The kinematic models are considered the lowest fidelity models. These models can compute the wake expansion and velocity deficits, without having to solve the cumbersome differential equations, as was the case for the Field models. These kinematic models are usually based upon the mass momentum conservation and turbulence mixing. Due to their simplicity, the computational times are lower when compared to CFD and field models. The kinematic models make use of self-similar velocity deficit profiles, where Lissaman [31] was the first with this approach. Lissaman used velocity profiles obtained from experiments, while Vermeulen [45] assumed Gaussian type of profile and where Katic et al. [27] even simplified it further by assuming a top-hat profile everywhere. The most used kinematic models are the Jensen model [26] which was improved by Katic [27], Larsen model [21] and the Frandsen model [15]. Also two relatively new and promising kinematic model will be discussed first one is the Bastankhah and Porté-Agel [6] model and the second is the Jensen-Gaussian model [19]

### 2.4.5 Jensen

The Jensen model is a simple kinematic model proposed by N.O. Jensen [26] and further improved by Katic [27]. This model is also implemented into the Park model, in the software WAsP by Risø. Where it is used for wind farm planning and to estimate annual energy productions in preliminary studies.

The single wake Jensen model assumes that the far wakes starts immediately after the rotor, thus neglecting the near wake region. This means that for the near region, the velocity field cannot be computed accurately. But since the turbines will be placed in the far wake region, this is not a issue. The model assumes linear expansion of the wake diameter starting from the rotor, where the wake starts with a diameter equal to that of the rotor. The model also assumes a constant velocity in the wake, the so called top-hate profile instead of the commonly used Gaussian distribution. This means that the actual velocity at certain points is not accurate, however the model is used to give an estimate of the energy content in the flow field, rather than to accurately model the velocity field. The model also neglects the blockage due to the ground surface, thus the wake can expand freely. The Jensen model is based upon mass conservation, see figure 2.3 for a description of the Jensen model, where the following equation can be derived:

$$\left(\frac{D_r}{2}\right)^2 u_r + \left[\left(\frac{D_w}{2}\right)^2 - \left(\frac{D_r}{2}\right)^2\right] u_0 = \left(\frac{D_w}{2}\right)^2 u_w, \quad (2.14)$$

where  $u_0$ ,  $u_r$  and  $u_w$  are respectively the undisturbed inflow velocity at hub height, rotor velocity just after the rotor and wake velocity at location  $x$  downstream of the rotor. Also  $D_r$  is the rotor diameter and  $D_w$  the wake diameter also at distance  $x$  downstream of the rotor. The wake is assumed to linearly expand with the downstream distance  $x$  with the following expression:

$$D_w = D_r + 2\alpha x, \quad (2.15)$$

where  $\alpha$  is the wake decay coefficient, which is an empirical parameter.

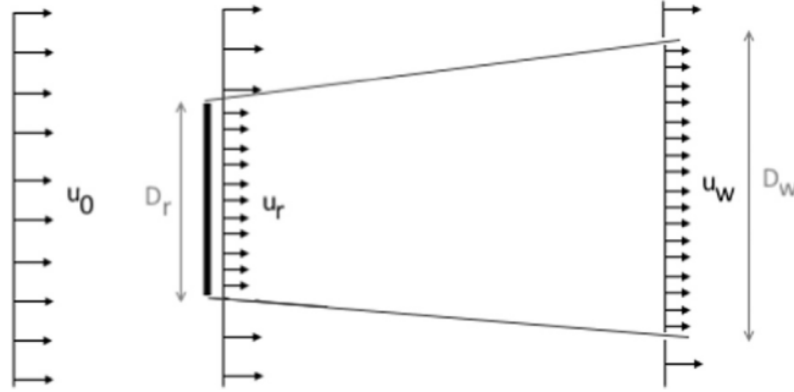


**Figure 2.3:** The control volume for the Jensen wake model [26]

With the momentum theory,  $\frac{U_r}{U_0}$  can be defined as a function of the axial induction factor, which is the fractional decrease in wind speed, and is expressed as following:

$$\frac{U_r}{U_0} = 1 - 2a, \quad (2.16)$$

where:

$$a = \frac{u_0 - u_r}{u_0}, \quad (2.17)$$

is an alternate expression for the axial induction factor can be used with the following assumptions; There is an ideal axial symmetry, no rotation, no turbulence and a conic shape wake profile. The axial induction factor can then be expressed as a function of the thrust coefficient  $C_T$ :

$$a = \frac{1 - \sqrt{1 - C_T}}{2}. \quad (2.18)$$

Inserting equations 2.15 - 2.18 into equation 2.14 and after re-arranging, the following expressions can be derived:

$$\frac{u_w}{u_0} = 1 - \frac{1 - \sqrt{1 - C_T}}{(1 + 2\alpha x/D_r)^2} \quad (2.19)$$

$$\frac{u_w}{u_0} = 1 - \frac{2 \left( \frac{u_0 - u_r}{u_0} \right)}{(1 + 2\alpha x/D_r)^2} \quad (2.20)$$

From equation 2.20 it can be seen that the velocity, distance  $x$  downstream of the rotor, depends on the wake decay coefficient  $\alpha$ . Or from equation 2.19 on the thrust coefficient  $C_T$ . The wake decay coefficient is an empirical parameter and according to [33] the semi-empirical equation 2.21 can be used to compute the wake decay coefficient. This yields a different value than the most commonly used 0.075 for on-shore and 0.04 for off-shore wake decay coefficients [34].

$$k_w = u_{free}/u_{hfree}, \quad (2.21)$$

where  $u_{free}$  is the free friction velocity and  $u_{hfree}$  the free hub height wind speed. These expression are a function of surface roughness length, local atmospheric stability correction

at hub height and turbulence intensity. The expressions for  $u_{free}$  and  $u_{hfree}$  can be found in [34]. An example of the velocity profile computed with the Jensen-Katic model can be found in figure 2.4.

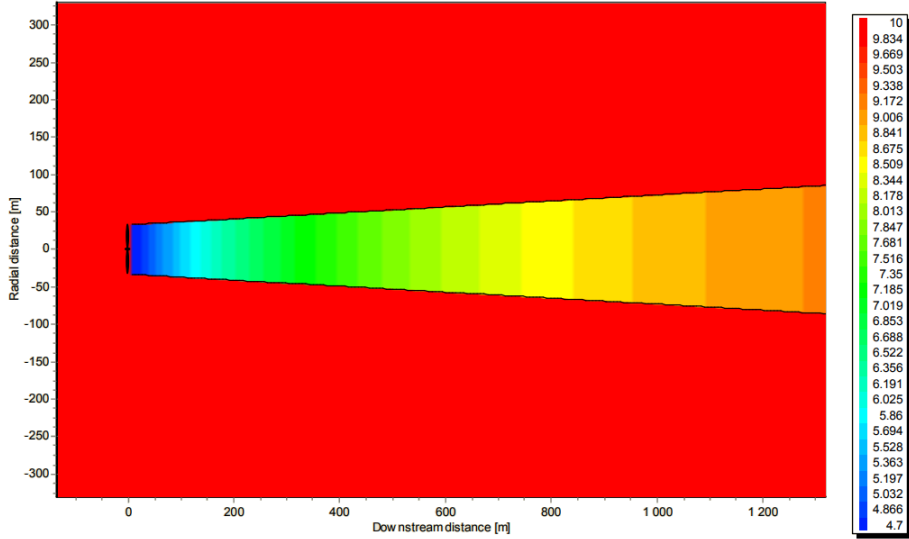


**Figure 2.4:** Wake velocity [m/s] for single turbine computed with the Jensen-Katic model [41]

### 2.4.6 Larsen model

Larsen introduced a semi analytical wake model, based on the assumptions that the wake flow is steady, incompressible, axi-symmetric and self-similar along the perpendicular direction to the flow [29]. He also neglected wind shear and thermal effects. This leads to the following equations:

$$\frac{\partial}{\partial x}((U_{\infty} + u_x)r) + \frac{\partial}{\partial x}(u_r r) = 0 \quad (2.22)$$

$$(U_{\infty} + u_x) \frac{\partial}{\partial x}(U_{\infty} + u_x) + u_r \frac{\partial}{\partial x}(U_{\infty} + u_x) = -\frac{1}{\rho} \frac{\partial p}{\partial x} - \frac{1}{r} \frac{\partial}{\partial r}(r \overline{u_x^* u_r^*}). \quad (2.23)$$

According to Larsen for first and second order solutions the pressure term can be neglected. Also the second term in equation 2.23, the Reynolds stresses, can be represented by Prandtl's mixing length theory which simplifies the equations to:

$$\frac{\partial}{\partial x}(u_x r) + \frac{\partial}{\partial r}(u_r r) = 0, \quad (2.24)$$

$$(U_{\infty} + u_x) \frac{\partial u_x}{\partial x} + u_r \frac{\partial u_x}{\partial x} = \frac{1}{r} \frac{\partial}{\partial r} \left[ l^2 r \left( \frac{\partial u_x}{\partial r} \right)^2 \right], \quad (2.25)$$

where  $x$  is the axial coordinate,  $r$  the radial coordinate,  $U_{\infty}$  is the free stream velocity and  $u_r$  &  $l$  represents the mixing length. Based upon Prandtl's idea, it is assumed that

for large Reynolds numbers the velocity in section perpendicular to the direction of flow are the same. This leads to the assumption that the local wake radius is proportional to  $x^n$  and the velocity profile in the cross-section of wake is self-similar according to:

$$u_x \equiv x^m f\left(\frac{r}{x^n}\right). \quad (2.26)$$

Larsen derived that  $n = \frac{1}{3}$  and that  $m + 2n = 0$ , thus leading to  $m = -\frac{2}{3}$ . From equations 2.24 - 2.26, the local wake radius  $r_w$  and the induced velocities in axial and radial direction, respectively  $u_x$  and  $u_r$  can be computed. In figure 2.5 an example of the wake velocity profile can be seen computed with the Larsen wake model.

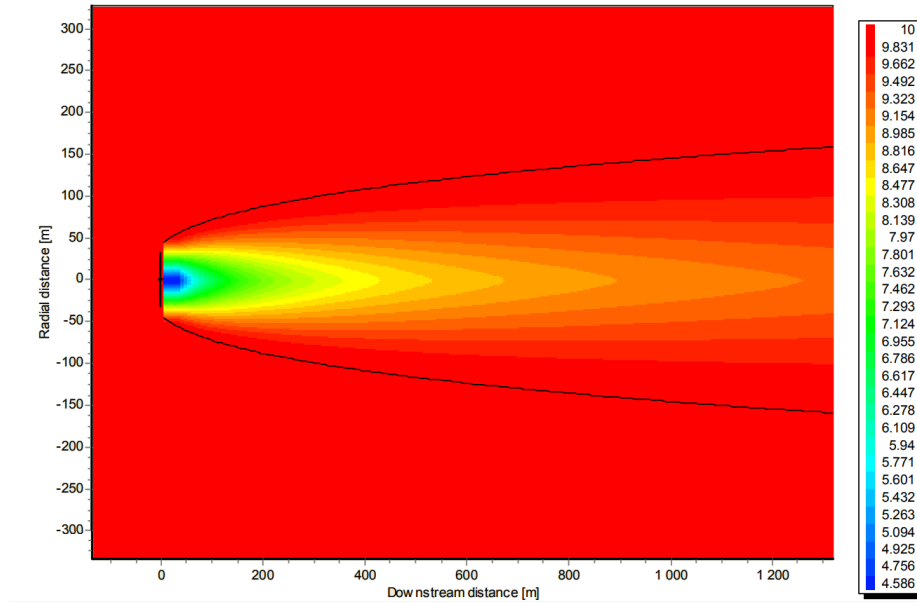


Figure 2.5: Wake velocity [m/s] for single turbine computed with the Larsen model [41]

### 2.4.7 Frandsen Model

This model was developed by Frandsen [16], it is designed for a specific layout of the turbines in a wind farm:

- It is assumed that the wind turbines are in a rectangular geometry with straight rows of wind turbines
- Each wind turbine is assumed to be spaced evenly at distance  $x$  and a dimensionless separation between turbines is defined as:  $s = \frac{x}{R}$ , where  $R$  is the radius of the turbine
- The wind direction is parallel to the rows

The analytical expression for the single wake model is derived from the momentum conservation. The momentum conservation is applied over a cylindrical control volume

around the wind turbine rotor with a diameter equal to that of the wake. The flow acceleration, pressure force, turbulent shear and gravity are neglected and the momentum equation in axial direction can be written as:

$$T = \int_A \rho U (U_0 - U) dA, \quad (2.27)$$

where  $A$  is the wake cross-sectional area,  $U_0$  the undisturbed wind speed,  $U$  the wake speed and  $T$  the thrust force of the rotor. The latter can be expressed as:

$$T = \frac{1}{2} C_T \rho A_0 U_0^2, \quad (2.28)$$

where  $C_T$  is the dimensionless thrust coefficient,  $\rho$  the density at hub height and  $A_0$  is the swept area by the rotor. Frandens model assumes that the wake expands before it reaches the rotor, this point after the initial expansion is considered the origin of the axial  $x$ -axis. An illustration of the control volume used for the momentum conservation equation can be seen in figure 2.6. Assuming a circular wake cross section is assumed with uniform velocity

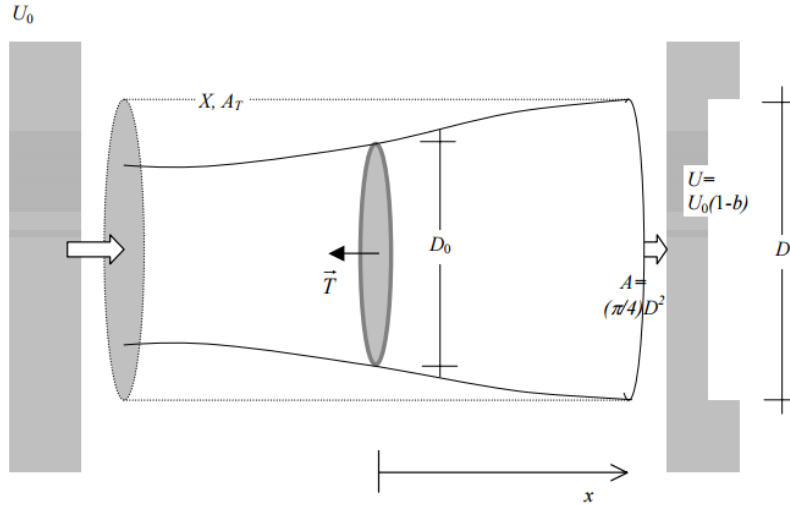


**Figure 2.6:** The cylindrical control volume that is considered for the Frandens model [16]

distribution Frandens derived the following equations:

$$D(s) = (\beta^{n/2} + \alpha \cdot s)^{1/n} D_0, \quad (2.29)$$

$$\beta = \frac{1}{2} \cdot \frac{1 + \sqrt{1 - C_T}}{\sqrt{1 - C_T}}, \quad (2.30)$$

$$\frac{U}{U_0} = \frac{1}{2} \pm \frac{1}{2} \sqrt{1 - 2 \frac{A_0}{A} C_T}, \quad (2.31)$$

where  $\alpha$  is the decay constant, which has to be determined from experiments.  $n$  is the parameter defining the shape of the wake expansion which is suggested to be equal to 3 according [33]. It should be noted that equation 2.31 will use the plus sign when  $1 - \sqrt{1 - C_T} \leq 0.5$  and the minus sign when  $1 - \sqrt{1 - C_T} > 0.5$ . An example of the wake velocity profile can be seen in figure 2.7

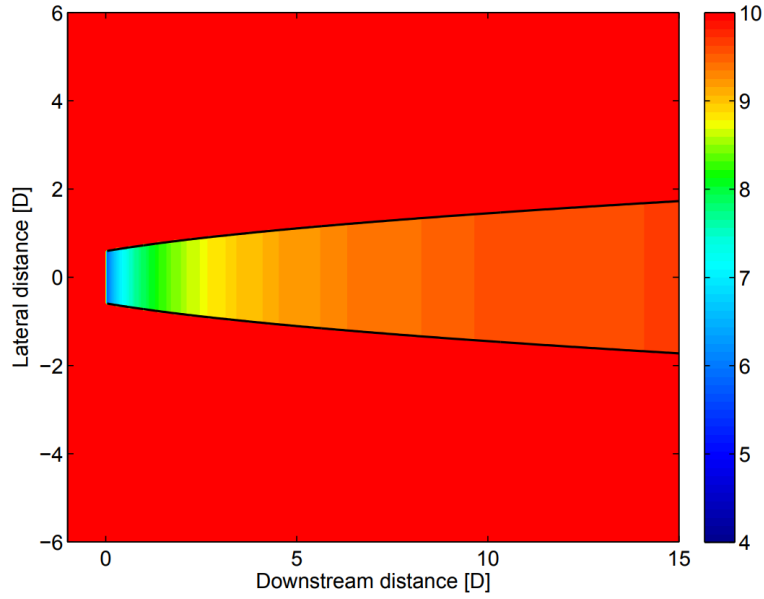


**Figure 2.7:** Wake velocity [m/s] for single turbine computed with the Frandsen model [36]

#### 2.4.8 Bastankhah and Porté-Agel Model

The Bastankhah and Porté-Agel Model (BP model), was developed in 2014 by Bastankhah and Porté-Agel [6]. This model is derived from the momentum equation just as the Frandsen model. The important difference is the velocity profile that is assumed in the wake cross-section. In the Jensen and Frandsen model a top hat velocity profile was assumed, however this is not in accordance with wind tunnel measurements [8], numerical solutions [47] and from wind farm measurements [20]. From these measurements it is seen that a Gaussian velocity profile is more suitable, which is the reason for implementing it in the BP model. The Gaussian distribution is assumed to be self-similar leading to a closed form solution of equation 2.27. The velocity deficit in the wake can be described with the following equation:

$$\frac{\Delta U}{U_\infty} = f(r/\delta(x))e^{-\frac{r^2}{2\sigma^2}}, \quad (2.32)$$

where  $C(x)$  is the maximum normalized velocity deficit at each downwind location which occurs at the center of the wake. Here  $r$  is the radial distance from the center of the wake and  $\delta(x)$  is the characteristic wake width at each  $x$ . The wake is assumed to have a Gaussian shape thus the equation can be re-written as:

$$\frac{\Delta U}{U_\infty} = C(x)e^{-\frac{r^2}{2\sigma^2}}, \quad (2.33)$$

where  $\sigma$  is the standard error of the Gaussian like velocity deficit profile at each  $x$ . Inserting equations 2.33 and 2.28 into equation 2.27 and integrating it from 0 to  $\infty$  will give the following equation:

$$8\left(\frac{\sigma}{d_0}\right)^2 C(x)^2 - 16\left(\frac{\sigma}{d_0}\right)^2 C(x) + C_T = 0. \quad (2.34)$$

When solving equation 2.34 two solution for  $C(x)$  are obtained, only the one that predicts a lower value of the two is physically acceptable. The solution is as following:

$$C(x) = 1 - \sqrt{1 - \frac{C_T}{8(\sigma/d_0)^2}}. \quad (2.35)$$

When assuming linear expansion just as Jensen the following expression can be used:

$$\frac{\sigma}{d_0} = k^* \frac{x}{d_0} + \varepsilon, \quad (2.36)$$

here  $k^* = \frac{\partial \sigma}{\partial x}$ , which is the growth rate and  $\varepsilon$  is the value that  $\frac{\sigma}{d_0}$  reaches, when  $x$  approaches zero. Inserting equations 2.35 and 2.36 into equation 2.33 the following expression for the velocity wake deficit can be derived:

$$\frac{\Delta U}{U_\infty} = \left(1 - \sqrt{1 - \frac{C_T}{8(k^*x/d_0 + \varepsilon)^2}}\right) \cdot \exp\left(-\frac{1}{2(k^*x/d_0 + \varepsilon)^2} \left\{ \left(\frac{z - z_h}{d_0}\right)^2 + \left(\frac{y}{d_0}\right)^2 \right\}\right), \quad (2.37)$$

where  $y$  and  $z$  are the spanwise and vertical components and  $z_h$  is the hub height. The above equation requires the value of  $\varepsilon$ , which can be determined by equation the total mass flow between this model and the Frandsen model. This can be done since both models are derived from the same governing equations. The following relationship for  $\varepsilon$  is derived:

$$\varepsilon = 0.25\sqrt{\beta}, \quad (2.38)$$

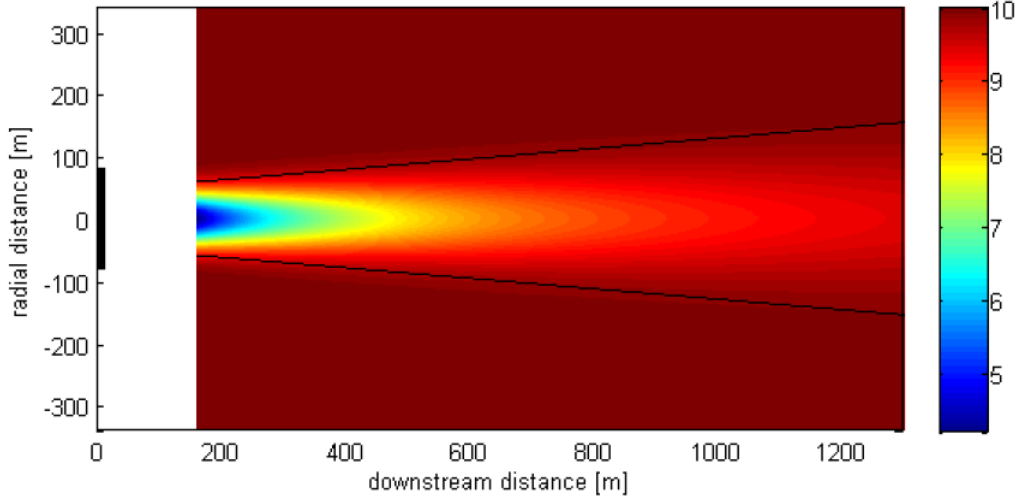


**Figure 2.8:** Wake velocity [m/s] for single turbine computed with the BP model [24]

where  $\beta$  was given in equation 2.30. The only thing that remains is to compute the wake-growth rate  $k^*$ . From LES results it was proposed by Porté-Agel [6], for the range of  $(0.065 < I_a < 0.15)$ , to calculate the wake growth with the following empirical equation:

$$k^* = 0.3837I + 0.003678, \quad (2.39)$$

where  $I_a$  is the ambient turbulence intensity and  $I$  is the local turbulence intensity at the turbine rotor. An example of the BP model can be found in figure 2.8.

### 2.4.9 Jensen-Gaussian

Multiple studies were performed to compute the optimal wind farm layout ([35], [17]). These studies computed the layout with the same wake model and objective function but different optimization algorithms. The studies were performed with the Jensen-Katic model which assumes a top hat velocity profile, this assumption causes inaccuracies in the computation. From wind-tunnel experiments and on site wind farm measurement [43] [8] it was found that a Gaussian velocity distribution in the wake is more realistic. To this extent, Jensen's wake model was modified by [19] to incorporate the Gaussian velocity distribution into its model instead of the top hat velocity profile. In figure 2.9 the difference between the two models can be found. The expression for the improved model

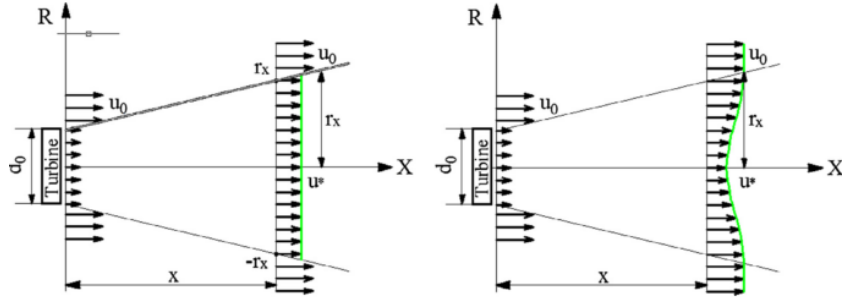


**Figure 2.9:** Left Jensen with top hat velocity profile, Right Jensen with Gaussian distributed velocity profile [19]

is as following:

$$u = A \left( \frac{1}{\sigma\sqrt{2\pi}} \cdot e^{-\frac{r_x^2}{2\sigma^2}} \right) + B. \quad (2.40)$$

With the help of the following three assumptions the parameters A,B and  $\sigma$  can be found:

- Using the properties of a Gaussian distribution it is proposed to have  $2.58\sigma = r_x$ , to obtain an 99% of the Gaussian distribution, here  $r_x$  is the wake radius of the original Jensen model.
- Now having the same wake radius, directly outside of the wake radius the velocity is equal to the free stream velocity:

$$u_0 = A \left( \frac{1}{\sigma\sqrt{2\pi}} \cdot e^{-\frac{(\pm r_x)^2}{2\sigma^2}} \right) + B. \quad (2.41)$$

- Across the wake tube with radius  $r_x$ , the Jensen model and Jensen-Gaussian are assumed to have the same mass flow flux leading to:

$$\int_{-r_x}^{r_x} \left( A \left( \frac{1}{\sigma\sqrt{2\pi}} \cdot e^{-\frac{(y)^2}{2\sigma^2}} \right) + B \right) dx = u^* 2r_x. \quad (2.42)$$

Solving these equations leads to the following expressions for A,B and  $\sigma$ :

$$\begin{cases} \sigma = \frac{r_x}{2.58} \\ B = u_0 \\ A = (u^* - u_0) \cdot 2r_x \end{cases} \quad (2.43)$$

So for the Jensen-Gaussian wake model the following formulae describes the velocity profile at a distance  $x$  downstream of the rotor:

$$\begin{cases} u^* = u_0 \left[ 1 - 2a/(1 + kx/r_1)^2 \right] \\ u = u_0 - (u_0 - u^*) \frac{5.16}{\sqrt{2\pi}} \cdot e^{-r^2/2 \cdot (r_x/2.58)^2} \end{cases} \quad (2.44)$$

Where  $k$  is rate of the wake expansion, which can be computed with equation 2.45. This relationship will be discussed later on in chapter 3, where the programmed model will be validated. Using the radius of a Vestas V-80 wind turbine, an uniform incoming flow and the initials conditions shown in table 2.1, the wake velocity for the Jensen-Gaussian model is computed and can be seen in figure 2.10. The black lines in figure 2.10 represent the linear expansion of the wake, with the rate of growth  $k$ .

$$k = 0.5 / \ln \left( \frac{z}{z_0} \right) \quad (2.45)$$

**Table 2.1:** Initial conditions used to compute the wake velocity downstream

Parameter	Value	Unit
$U_0$	10	[m/s]
$I_0$	0.08	[-]
D	80	[m]
k	0.07	[-]

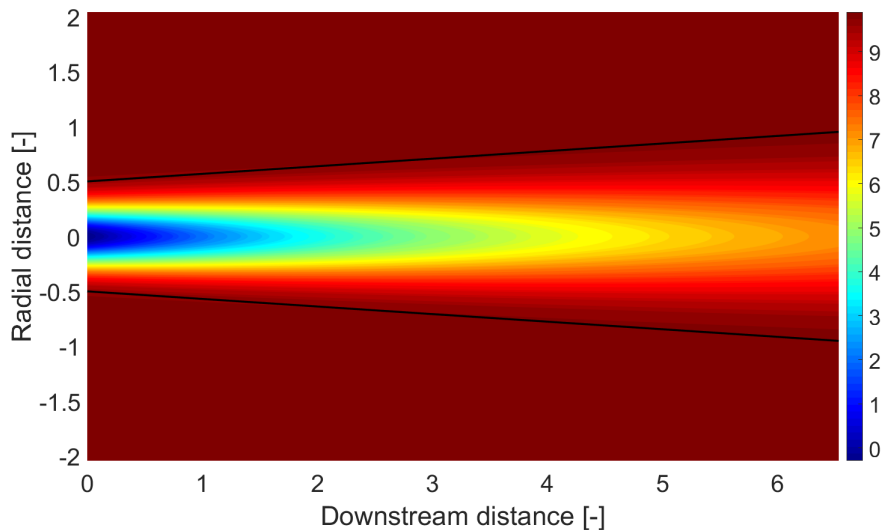


**Figure 2.10:** Wake velocity [m/s] for single turbine computed with the Jensen-Gaussian model

## 2.5 Wind farm layout optimization

In this section objective function for optimizing the wind farm layout will be discussed.

### 2.5.1 The objective function

In the paper that proposed the Jensen-Gaussian wake model [19], the optimization technique Multiple Population Genetic Algorithm (MPGA) was used to optimize the wind farm layout. The objective function used by MPGA is to find the minimum Cost Of Energy (COE).

The Costs of the wind farm consists of multiple components, the EPRITAG method [28] is used to approximate the COE with the following expression:

$$COE = \frac{(C_{Tur} + C_{SS} + C_{TS}) \cdot FCR + OM}{power}, \quad (2.46)$$

where  $C_{Tur}$  is the turbine costs,  $C_{SS}$  is the cost of the support structure,  $C_{TS}$  is the transmission cost, FCR is the fixed charge rate, a present value factor that includes debt and equity costs, taxes, and insurance and OM is the operation and maintenance costs.

### 2.5.2 Energy calculation of the wind farm

The MPGA model makes use of the Wind Farm Power Generation Calculation Tools (WFPGCT) [18], which is a code that computes the wind farms energy yield. According to Gao et al. [18]: "In the WFPGCT program, the wake effect at different wind directions of each wind turbine is considered instead of considering the prevailing wind direction only." However the methodology of how the code computes the actual wind energy in the farm is not described.

According to Lackner [28], the wind speed probability density at a site is commonly approximated with a Weibull function. With this probability function the Annual Energy ( $E_a$ ) output over a total time per year T of a wind turbine can be computed with the following equation:

$$E_a = T \int_{U_{ci}}^{U_{co}} P(U) \cdot f(U) dU, \quad (2.47)$$

where the integration is performed from cut in velocity to cut out velocity, and where  $f(U)$  is the Weibull distribution, which is given as:

$$f(U) = \frac{k}{c} \left( \frac{U}{a} \right)^{k-1} \cdot e^{-\left(\frac{U}{c}\right)^k}, \quad (2.48)$$

where k is the shape factor and c is the scale factor, these are chosen such that they fit the wind speed distribution obtained from measurements. The function  $P(U)$  is the power as a function of the velocity at hub height, this is usually given for a specific wind turbine as a P-V Curve.

The above energy equation 2.47, yields the annual energy for a single wind turbine in one direction for different wind speeds. To extend this to the case where the wind direction has to be taken into account, use is made of the wind rose. The Power and weibull distribution are now a function of both  $U$  and  $\theta$ , where  $\theta$  is the wind direction. In this way the Annual Energy for a wind farm can be calculated with the following equation:

$$E_{a,windfarm} = T \int_0^{360} \int_{U_{ci}}^{U_{co}} \left( \sum_{i=1}^N P_i(U, \theta) \right) \cdot f(U, \theta) dU d\theta, \quad (2.49)$$

where  $i$  is the turbine that is considered and  $N$  is the number of turbines in the wind farm.



# Validation Jensen-Gaussian Model

In this chapter the chosen wake model will be modeled and validated. First the reasoning behind selecting the Jensen-Gaussian will be discussed. Second the Jensen-Gaussian model will be validated using the field measurements of a single turbine wake. And finally the different turbulence models will be modelled and discussed.

### 3.1 Selected Wake model

From the literature study it was concluded, that the Jensen-Gaussian model is most suitable to tackle the wind farm layout optimization problem in this thesis. The first reason is that the Jensen-Gaussian model, being a kinematic model, is relatively computational inexpensive. The second reason is, that the Jensen-Katic model is extensively used in papers for preliminary analysis of the optimum wind farm layout problem. Thus using the extended Jensen-Gaussian wake model for the WFLOP, might yield better results. The final reason is that it is relatively easy to program and will be easier to adjust according to the effects of the ABL on the wind farm physics.

### 3.2 Single wake validation

In chapter 2.4.9 the theory behind the Jensen-Gaussian wake model is explained. The Jensen-Katic wake model is based upon the mass conservation principle, it assumes a constant velocity in the wake, the so called top-hat profile. The Jensen-Gaussian model refined the top-hat profile, based on observation of measurements and numerical computations, into a Gaussian distributed profile. Using measurement data acquired from the Garrad Hassan wind tunnel, the performance of both the Jensen-Gaussian and Jensen-Katic wake model will be analyzed. Using equations 2.20, 2.44 and 2.45, with the initial conditions of table 3.1, the velocity deficits at  $2.5D$ ,  $5D$ ,  $7.5D$  and  $10D$  downstream can be computed using the Jensen-Gaussian and Jensen-Katic wake model. The results can be found in figures 3.1-3.4.

It can be seen that the Jensen-Gaussian model has a better performance than the Jensen model, with respect to the velocity deficit. The wake models are not capable of accurately capturing the near wake, this can be seen in figure 3.1 where at  $2.5D$  downstream the model underestimates the velocity deficit. However in the far wake  $5D$ ,  $7.5D$  and  $10D$ , the Jensen-Gaussian model is in good agreement with the wind tunnel measurements.

It should be noticed that the wake model did not take the added turbulence intensity into account. The ambient turbulence intensity (T.I.) inside a wind farm can play an important role in the recovery of the wake, the higher the T.I. the faster the wake will recover. To improve the performance of the wake models, a closer look into turbulence intensity models will be taken.

**Table 3.1:** Initial conditions used to compute the wake velocity downstream for the Garrad Hassan windtunnel

Parameter	Value	Unit
$U_0$	5.3	[m/s]
$D$	43.2	[m]
$C_T$	0.62	[-]
$z$	0.07	[m]
$z_0$	0.62	[m]

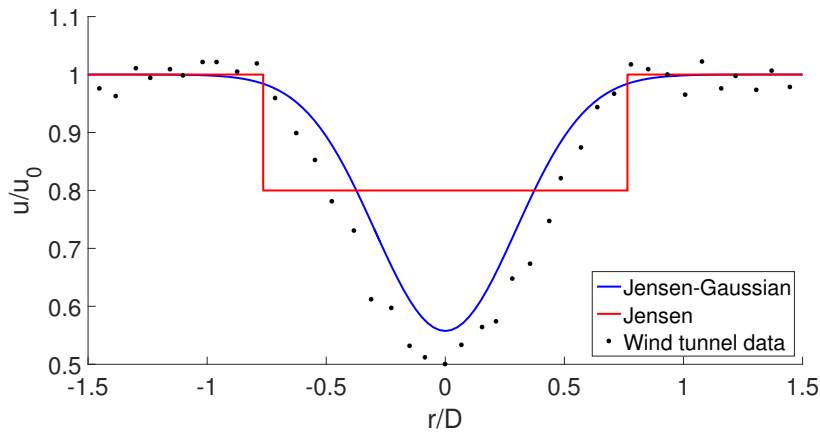


**Figure 3.1:** Comparison between the windtunnel measurements and wake models at  $2.5D$  downstream

### 3.3 Turbulence intensity models

When computing the wake recovery, the wake decay coefficient  $k$  is an important parameter to consider. One of the factors influencing the wake decay coefficient is the turbulence intensity. The Ambient T.I. was already mentioned, but also turbine induced T.I. should be considered. This means that the turbulence intensity varies at different locations of

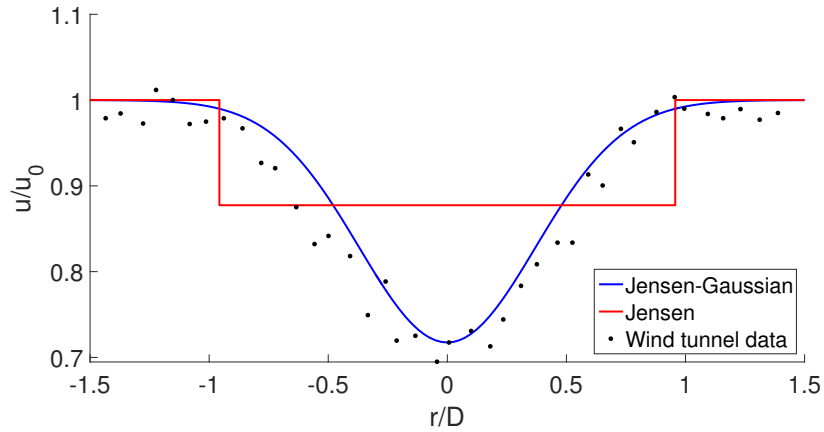


**Figure 3.2:** Comparison between the windtunnel measurements and wake models at 5D downstream

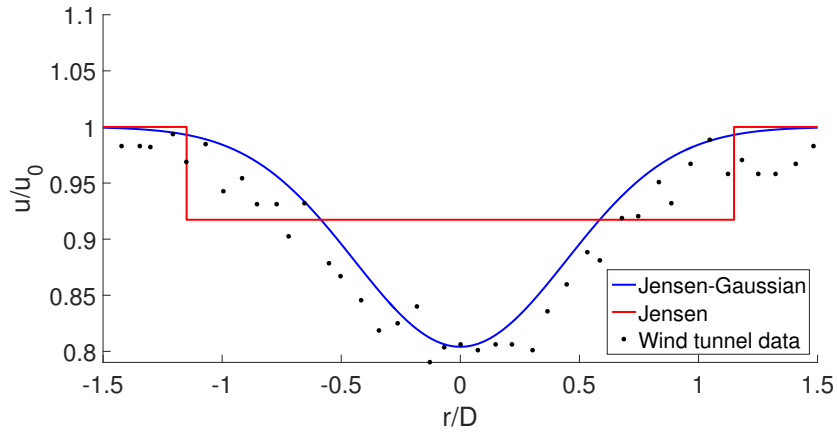


**Figure 3.3:** Comparison between the windtunnel measurements and wake models at 7.5D downstream

the wind farm, due to different turbine wakes merging and dissipation of the turbulence intensity. This increased turbulence intensity can be computed with different models. Not taking the added T.I. into consideration can lead to underestimation of the wake recovery.

Three different turbulence models will be discussed: Crespo and Hernandez, Frandsen and Gao's model.

Crespo and Hernandez (C&H) introduced based on both numerical and experimental data the following empirical equation to compute the added turbulence  $I_+$  [12]:

$$I_+ = 0.73a^{0.8325}I_a^{0.0325}(x/D)^{-0.32}, \quad (3.1)$$

$$I_{wake} = \sqrt{I_0^2 + I_+^2}, \quad (3.2)$$

where  $a$  is the axial induction factor specific to the turbine,  $x$  is the downwind distance

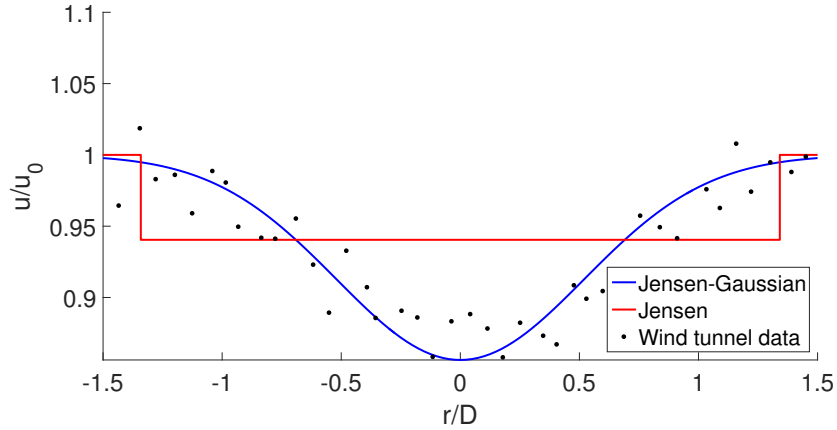


**Figure 3.4:** Comparison between the windtunnel measurements and wake models at 10D downstream

and  $D$  the turbine diameter. Also it should be said that the empirical equation holds for the following range:

- $5 < x/D < 15$
- $0.07 < I_a < 0.14$
- $0.1 < a < 0.4$

Frandsen et al. [14] suggested a different model for the turbulence intensity in the wake, the following expression was given:

$$I_w = \sqrt{K_n \frac{C_T}{(x/D)^2} + I_a^2}. \quad (3.3)$$

For the Jensen-Gaussian wake model a separate turbulence model was proposed by Gao et al [19]. This model was created to balance the effects of ambient turbulence intensity and turbulence intensity in the wake. The following empirical equations are given:

$$I_w = \left( K_n \frac{C_T}{(x/D)^{0.5}} + I_a^{0.5} \right)^2 \quad (3.4)$$

$$k_{wake} = k \frac{I_{wake}}{I_a}. \quad (3.5)$$

The different turbulence models will be validated with field measurement data acquired from the Nibe site [40]. Using the initial conditions from table 3.2, the wake velocity deficit was computed for the above discussed turbulence models. The results can be seen in figures 3.5 and 3.6, for respectively  $4.5D$  and  $7.5D$  downstream.

### 3.4 Conclusion

It can be concluded that without the turbulence models, there is a large discrepancy between the measurements and the Jensen-Gaussian wake model. Of the three turbulence models, the Gao turbulence model performs best and is in good agreement with the measurement data in the range of  $-0.5 < r/D < 0.5$ . However, moving further in the radial direction the wake model and the measurement data deviate and a maximum error of 2% occurs. The Frandsen en C&H turbulence model almost show the same performance. They perform worse than the Gao turbulence model. However, it is shown that implementing the Frandsen and C&H turbulence models, leads to a better approximation of the velocity deficit than the unimproved wake model. It can be seen in figure 3.5, that there is a maximum difference of 15% at the center of the wake between the measurements and both these models. The only difference is that the relative difference between the field measurements and Frandsens turbulence model slightly increases, while that of C&H stays around 15%. This means that Frandsens turbulence model underestimates the turbine induced turbulence downstream. This can be seen in Frandsens turbulence equation 3.3, where  $C_T$  is divided by  $(x/D)^2$ , compared to C&H turbulence model where they divide by  $(x/D)^{-0.32}$ . Where a lower turbine induced turbulence, will result in a slower recovering wake. In conclusion, the model suggested by Gao et al. performs the best out of the three models. The results obtained with this model are in good agreement with the field measurements at  $4.5D$  as well as at  $7.5D$ . Therefore it is chosen for the remainder of the thesis to combine the Jensen-Gaussian model with the turbulence model suggested by Gao et al.

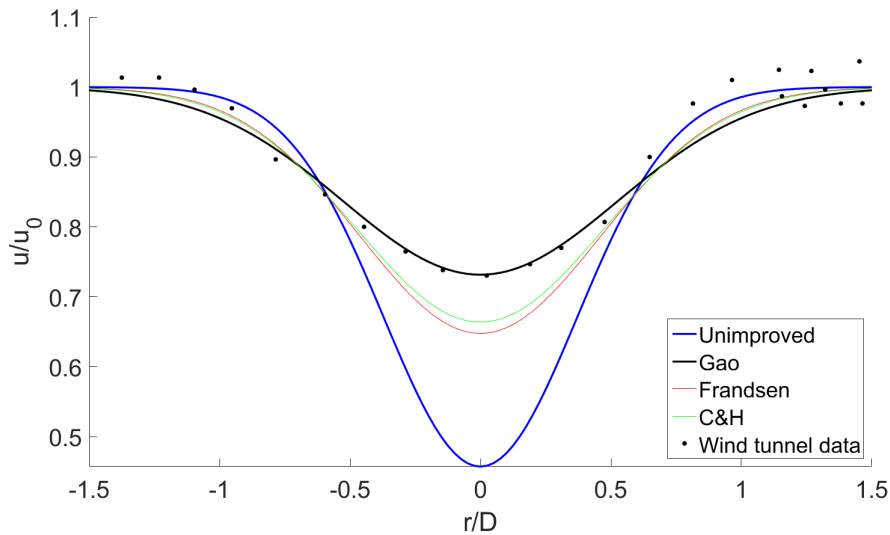


**Figure 3.5:** Comparison between the Nibe site measurements and Jensen-Gaussian with different turbulence models at  $4.5D$  downstream

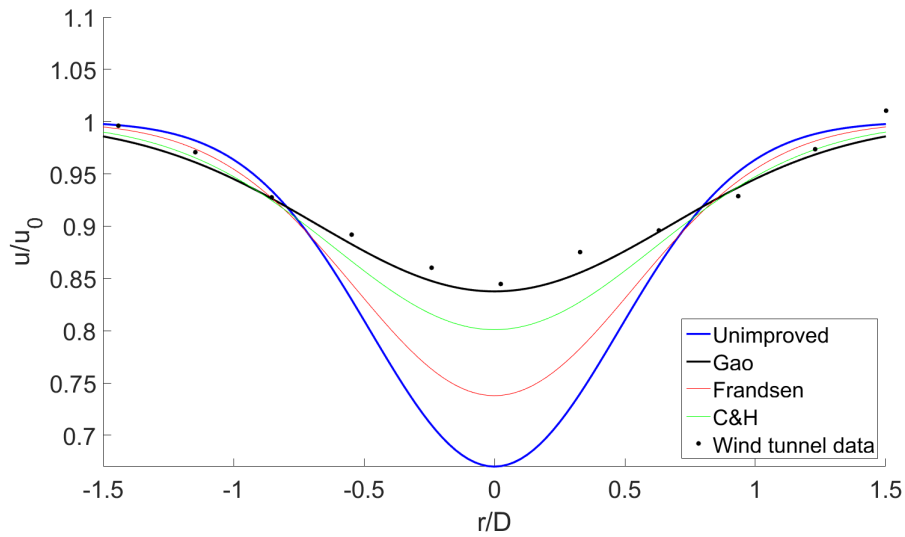


**Figure 3.6:** Comparison between the Nibe site measurements and Jensen-Gaussian with different turbulence models at 7.5D downstream

**Table 3.2:** Initial conditions Nibe site

Parameter	Value	Unit
$U_0$	8.55	[m/s]
$D$	40	[m]
$C_T$	0.82	[-]
$I_0$	10	[%]

# Wind farm validation

In this chapter the Jensen-Gaussian model will be extended such that it can compute the velocity deficit and power output in a wind farm. First the different wake summation methods will be discussed. Second the discretization of the velocity deficit, in order to compute the equivalent velocity, will be treated. Finally the extended wake model will be validated with results obtained from the Horns Rev wind farm.

## 4.1 Wake summation

Wake summation plays an important role when computing the velocity deficit in a wind farm. Because both the power output and  $C_T$  depend on the velocity. From the literature study it was concluded that there are two suitable super position methods, linear and Root Mean Square (RSS) summation. These super position models do not have any constraints, however most of them are not based on any physics and are just theoretical assumptions.

### 4.1.1 Linear summation

Linear summation of the velocity deficit was proposed by Lissaman [31]. Lissaman said he justified his method based on the following: "The linear superposition of the wakes is justified using an analogy between turbine wakes and pollution plumes, whose Gaussian concentration distribution can be superimposed due to the linearity of the process. Since pollutant mass is conserved by applying superposition, in the same way superposition of velocity deficit conserves the linearized momentum deficit." The following equation was used:

$$U_i = U_\infty - \sum_k (U_\infty - U_{k,i}), \quad (4.1)$$

where  $U_i$  is the velocity at turbine  $i$  and  $U_{k,i}$  is the wake velocity at turbine  $i$  by the wake of turbine  $k$ . A couple of slightly different linear superposition models are available, such as the one proposed by and Niayafar and Porte-Age [32]. Niayafar had an adjustment

w.r.t. the aforementioned linear summation method. Instead of the velocity difference between the undisturbed flow and  $U_{k,i}$ , the relative velocity deficit is used:

$$U_i = U_\infty - \sum_k (U_k - U_{k,i}) \quad (4.2)$$

, here  $U_k$  is used instead of  $U_\infty$ , which is the inflow velocity of turbine  $k$ .

#### 4.1.2 Root Sum of Squares

The RSS model, also sometimes referred to as the energy balance method was proposed for the Jensen model by [27]. This wake summation model assumes that the kinetic energy deficit of a superimposed wake equals the sum of the energy deficit of each wake with the following equation:

$$U_i = U_\infty - \sqrt{\sum_k (U_\infty - U_{k,i})^2}. \quad (4.3)$$

As mentioned before, this model it is often called the energy balance method but this is not entirely correct since:

$$U_\infty^2 - U_{k,i}^2 \neq (U_\infty - U_{k,i})^2. \quad (4.4)$$

Just as for the linear superposition model also a couple of variations exist for the RSS model. Voutsinas et al. [46] proposed a RSS model where instead of the absolute difference the relative velocity difference is used:

$$U_i = U_\infty - \sqrt{\sum_k (U_k - U_{k,i})^2}. \quad (4.5)$$

## 4.2 The equivalent incoming wind velocity

The turbulence intensity in equation 3.4 depends on the thrust coefficient. The thrust coefficient on its turn depends on the incoming velocity. The  $C_t - U$  curve of the Vestas V-80 wind turbine can be seen in figure 4.2. Besides the thrust coefficient also the power depends on the incoming velocity. However the incoming velocity across a turbine cross section is not uniform. In order to compute the  $C_t$ , the non-uniform velocity needs to be transformed into a single equivalent velocity.

### 4.2.1 Rotor discretization

The first step in computing the equivalent velocity, is to discretize the turbine cross section. Since the turbine cross section is circular, a polar discretization scheme will be implemented. The radius is uniformly divided by  $N_r$  number of elements and by  $N_t$  number in tangential direction. The velocity is computed in the center of the elements area  $A_i$ , an example can be seen in figure 4.1.

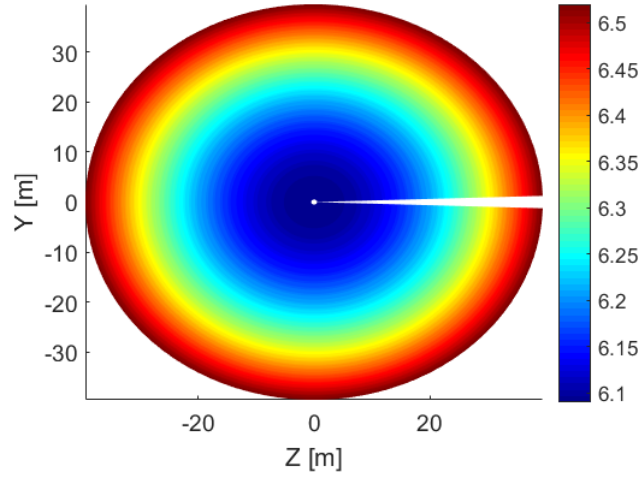


**Figure 4.1:** Discretized wake cross section using  $N_r = 40$  and  $N_t = 100$

### 4.2.2 Computation of the equivalent velocity

In the region between the cut-in velocity and rated velocity, the power holds a cubic relationship while the thrust coefficient has a quadratic relationship with the wind speed. It was concluded by B.Hu [24] that equations 4.6 and 4.7 can be used to compute the equivalent velocity ( $U_{eq}$ ), for respectively the thrust coefficient and the power.

$$U_{Cteq} = \sqrt[2]{\frac{\sum_{i=1}^{i=N_r \cdot N_t} A_i \cdot U_i^2}{\sum_{i=1}^{i=N_r \cdot N_t} A_i}} \quad (4.6)$$

Equation 4.6 makes use of the quadratic relationship between the thrust coefficient and the discretized velocity in each element. Where  $A_i$  is the area of the element and  $U_i$  is the velocity computed in the center of the element.

$$U_{Peq} = \sqrt[3]{\frac{\sum_{i=1}^{i=N_r \cdot N_t} A_i \cdot U_i^3}{\sum_{i=1}^{i=N_r \cdot N_t} A_i}} \quad (4.7)$$

Where equation 4.7 assumes a cubic relationship between the equivalent velocity for the power and the incoming wind speed.

## 4.3 Horns Rev Wind farm

The Jensen-Gaussian wake model needs to be combined with one of the proposed wake summation methods. In order to determine which summation method will produce the

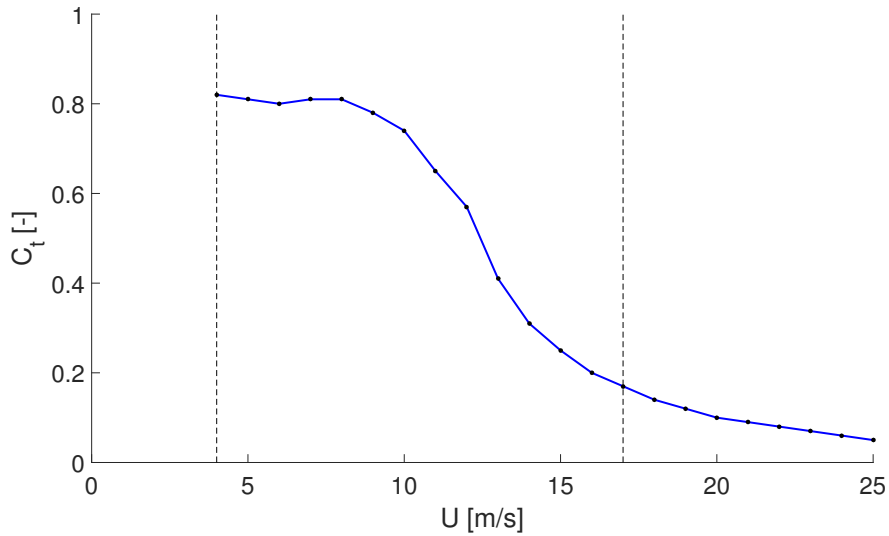


**Figure 4.2:** Vestas V-80  $C_t - U$  curve, dashed lines represent the cut-in and rated velocity

best results. The wake model will be compared with data obtained from the Horns Rev wind farm. The Horns Rev offshore wind farm consists of 80 Vestas V80-2MW wind turbines, achieving a 160 MW total rated power output. The turbines have a hub height of 70 m and diameter of 80 m. The wind farm layout has a rhomboid shape, which can be seen in figure 4.4. The wind farm has 8 columns and 10 rows, with a spacing of 7 diameters between two turbines. LES data from the paper of Niayifar and Porte-Agel [32] is used to validate the Jensen-Gaussian wake model. The surface roughness length for the Horns Rev wind farm is approximately 0.05m, with a T.I. of 7.7% and velocity of 8m/s at hub height.

### 4.3.1 Velocity deficit superposition

The linear summation method is also known as the velocity deficit superposition method. The equations 4.1 and 4.2 will be validated by using the LES data from Niayifar [32]. It is immediately found that using equation 4.1, leads to overestimation of the wake deficit. This results into an incoming wind speed of 1 m/s at the fourth turbine downstream. Since this leads to unrealistic results it is proposed to use the relative linear summation method, equation 4.2. The results for the relative linear summation can be found in figure 4.5.

It can be seen that using the relative velocity deficit summation, the generated power of the second turbine is overestimated. While after the second turbine the generated power of the remaining downstream wind turbines are underestimated. The LES data shows an important trend that needs to be simulated, which is that the wake recovers faster behind the second wind turbine and the remaining downstream turbines reach a certain equilibrium. It can be concluded that the Jensen-Gaussian wake model in combination with Gao's turbulence model and the relative velocity deficit summation does not predict the correct velocity deficit in a wind farm.

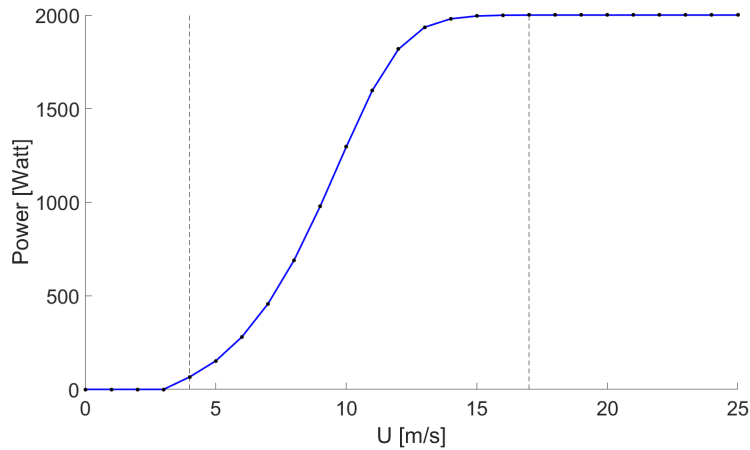


**Figure 4.3:** Vestas V-80  $P - U$  curve, dashed lines represent the cut-in and rated velocity

### 4.3.2 Energy deficit superposition

The energy summation method can be seen in equations 4.3 and 4.4. Just as in the linear case it is concluded that only the relative superposition method is suitable, because of the aforementioned reason. The results for the relative energy deficit superposition method can be seen in figure 4.6.

It can be concluded that yet again the generated power at the second downstream turbine is overestimated. This is logical since both equations compute the same velocity at the second turbine. The reason the power generated is overestimated, is because the velocity deficit recovers faster. The wake recovery depends on the T.I. as mentioned in chapter 3.3. The higher the T.I. the faster it recovers. However the energy deficit method reaches an equilibrium after the third turbine, which is in better agreement with the LES data.

### 4.3.3 T.I. validation

Since the wake deficit recovers too fast at the second turbine, the T.I. will be validated. The corresponding T.I. data is also obtained from the LES performed by Niafayar [32]. The LES data is compared with Gao's turbulence model and can be seen in figure 4.7. It can be noticed that the turbulence intensity at each turbine position is higher compared to the LES data. This explains why in the relative energy summation method, the power is overestimated for each turbine. However this faster recovery does not hold up for the linear summation method. Thus it can be concluded that the linear superposition equation 4.2, is not suitable in combination with the Jensen-Gaussian model and Gao's turbulence model.

To further investigate the effect of the T.I. on the generated power. The relative energy summation method is combined with the Frandsen turbulence model, equation 3.3. It was mentioned in chapter 3.3, that the Frandsen turbulence model underestimates the wake recovery. The results for the normalized power can be found in figure 4.8 and the computed T.I. can be found in figure 4.9. As previously mentioned it can be seen that the

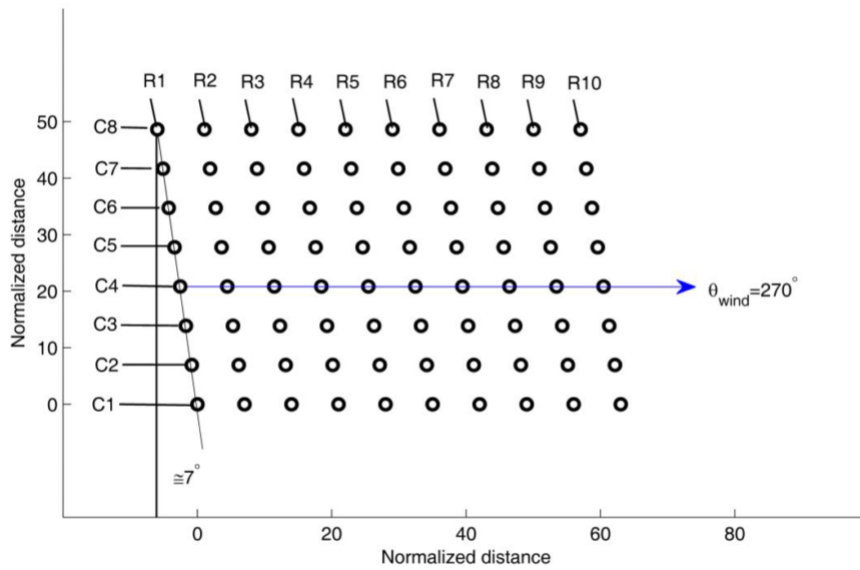


**Figure 4.4:** Horns Rev offshore wind farm layout, consisting of 40 Vestas V80-2MW wind turbines [32]

generated power is underestimated, which is related to the fact that also the T.I. at each position is underestimated.

Comparing the LES and turbulence model in figures 4.7 and 4.9, a constant T.I. difference is noticed. In order to see to what degree the T.I. effects the generated power, this difference will be artificially compensated. This is achieved by reducing the T.I. overall in the wake by 1% and increasing it by 3.8%, for respectively the Gao and Frandsen turbulence models. In figure 4.11, it can be seen that the T.I. for both turbulence models are in good agreement with the LES data. However it can be seen in figure 4.10, that even with the correct T.I. the normalized power does not agree with the LES Data.

## 4.4 Conclusion

It can be concluded that the Gao turbulence model overestimates the turbulence intensity and also the normalized power output is overestimated. However when the turbulence intensity is in good agreement, the Jensen-Gaussian model with energy deficit superposition method still overestimates the generated power. This could be explained due to using the power curve 4.3. The technique used to model the Vestas V-80 power curve is unknown, this could lead to incorrect values when not used properly. An alternative approach to compute the generated power, is to use the actuator line method. However for the Vestas V-80 the blade data is not readily available. Another reason for the difference could be due to the effect of the ABL on a wind farm. The stability of the ABL can influence the wake development in a wind farm, which is not accounted for in the wake model. This could lead to a different wake deficit and hence explain the difference in the computed generated power. Since these factors cannot be validated without the blade and ABL data, it is chosen to run the LES with an ABL ourselves. It is chosen to use the energy

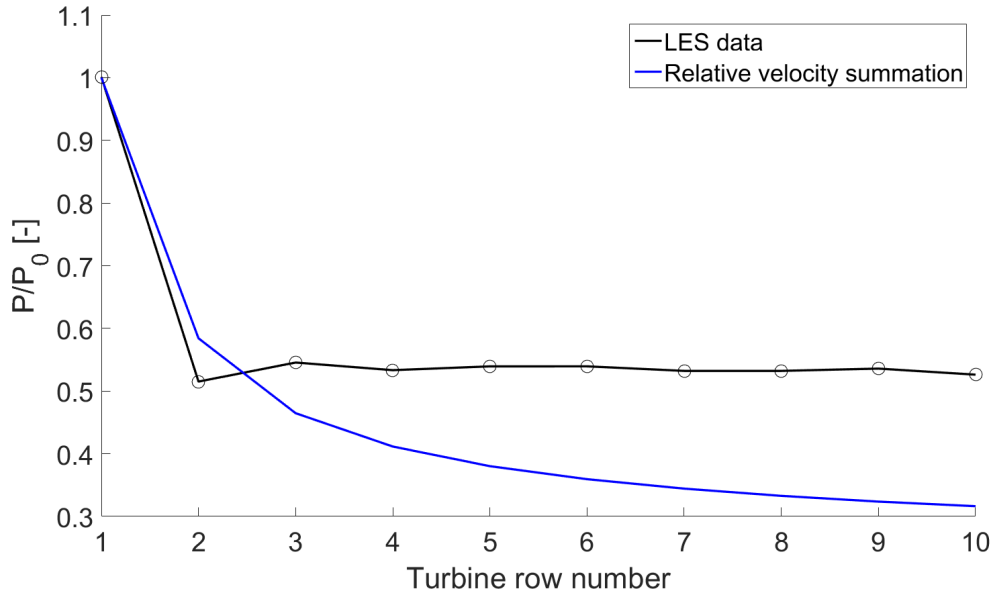


**Figure 4.5:** Horns Rev wind farm case: Normalized power obtained from LES compared with the computations acquired from the Jensen-Gaussian wake model, with Gao's turbulence model and relative velocity superposition method

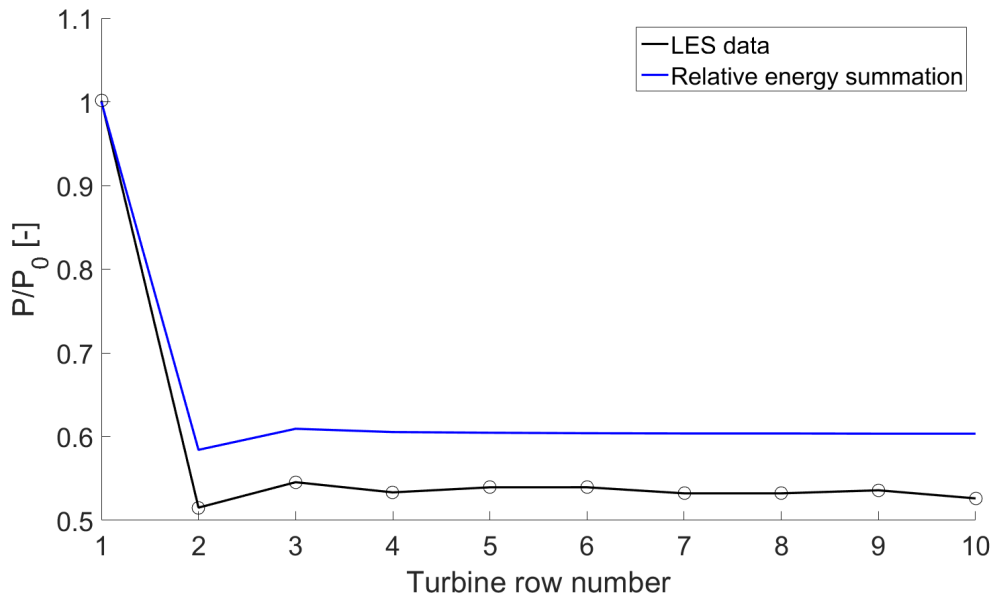


**Figure 4.6:** Horns Rev wind farm case: Normalized power obtained from LES compared with the computations acquired from the Jensen-Gaussian wake model, with Gao's turbulence model and relative energy superposition method

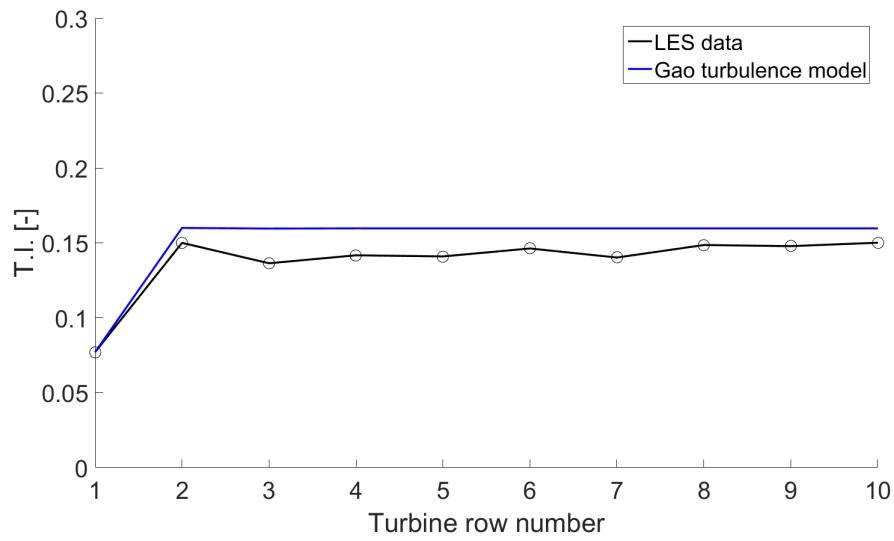


**Figure 4.7:** Horns Rev wind farm case: Turbulence intensity obtained from LES compared with Gao's turbulence model

deficit superposition method, since it shows the right generated power trend in a wind farm with aligned wind turbines.

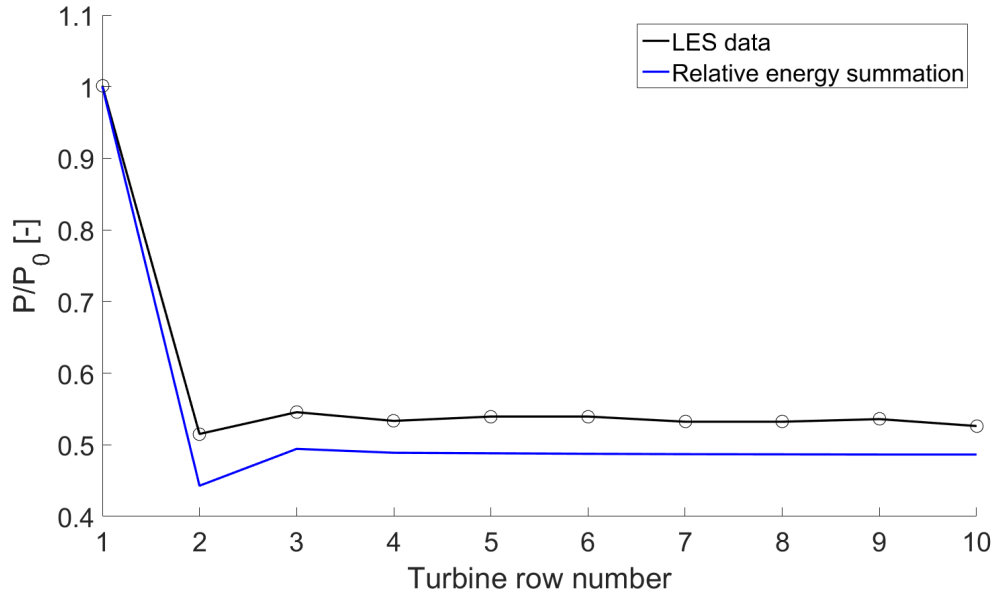


**Figure 4.8:** Horns Rev wind farm case: Normalized power obtained from LES compared with the computations acquired from the Jensen-Gaussian wake model, with Frandsens turbulence model and relative energy superposition method

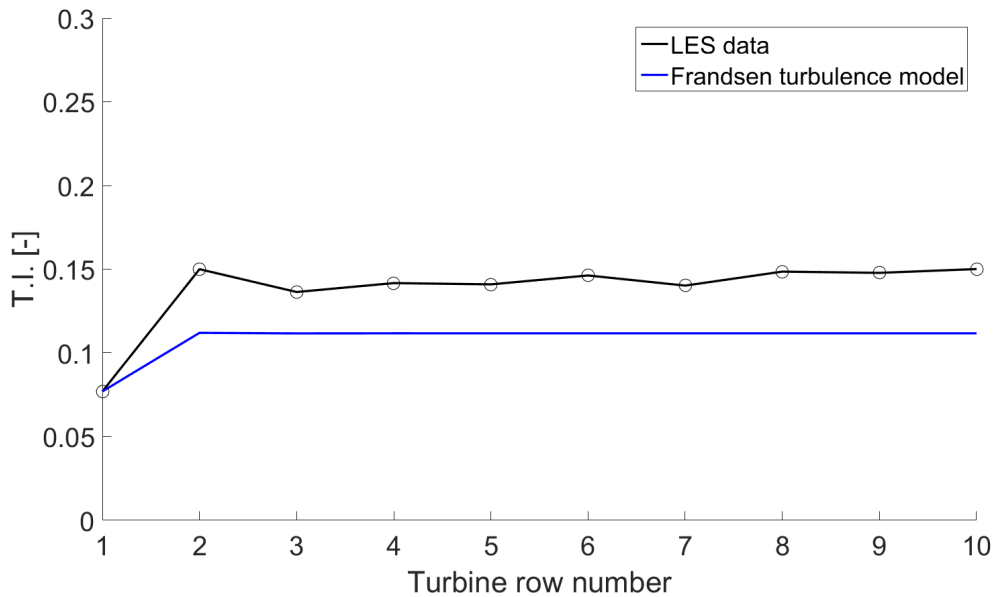


**Figure 4.9:** Horns Rev wind farm case: Turbulence intensity obtained from LES compared with Frandsens turbulence model

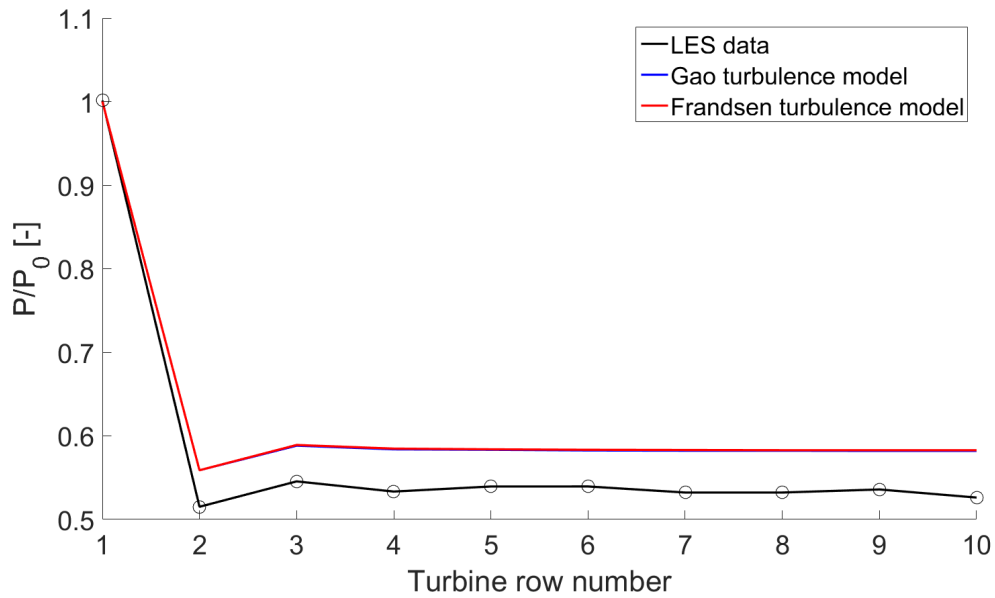


**Figure 4.10:** Horns Rev wind farm case: Normalized power obtained from LES compared with Gao and Frandsens turbulence model with the same matching T.I.

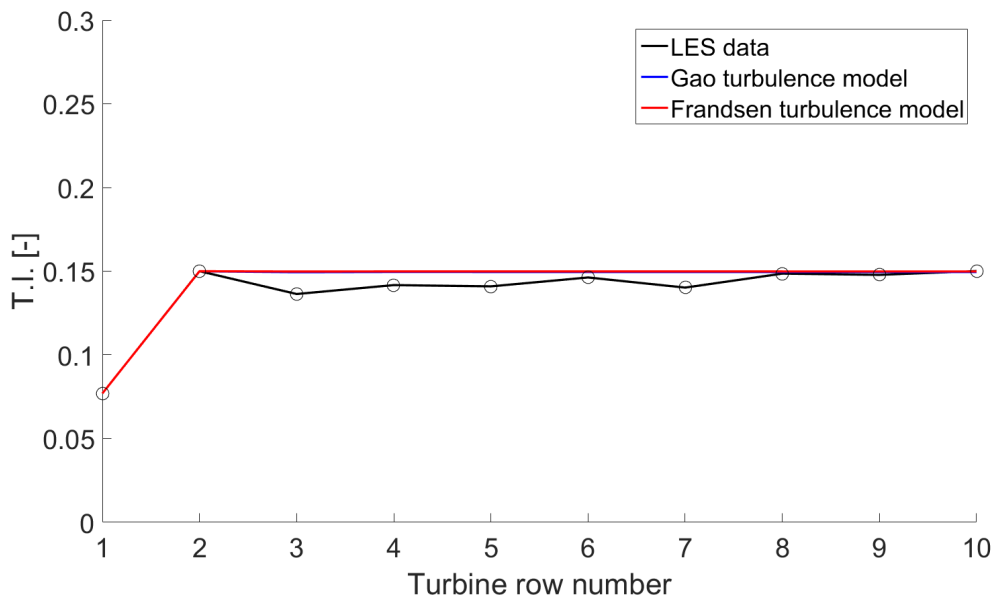


**Figure 4.11:** HornsRev wind farm case: Artificially subtracted 1% T.I. of Gao's turbulence model and added 3.8% to Frandsens turbulence model

# SOWFA Large Eddy Simulation

In this chapter the Large Eddy Simulation (LES) is discussed. First an insight into openFOAMs background is given. Second the openFOAM extension SOWFA, which is used to simulate the turbine models, is explained. Third an uniform flow LES case in SOWFA is treated and the results are discussed. Afterwards the ABL precursor for different stabilities is simulated, validated and discussed. Finally the wake model is extended according to the findings.

## 5.1 openFOAM

In order to solve the flow for the wind turbine cases, the free Open-source Field Operation and Manipulation CFD software OpenFOAM<sup>®</sup> is used. OpenFOAM is written in C++, it makes use of finite volume formulation to solve the governing equations of a certain CFD case. Tools in OpenFOAM can be run in parallel by using Message-Passing Interface (MPI), making it suitable to run large cases. Each case directory in OpenFOAM has three directories: constant, system and initial time directory. These folders contain the data required to initialize and run the simulation. The constant folder contains the mesh, boundary conditions and physical models. The initial time directory contains the initial and boundary conditions for the flow variables. The system directory holds the data that has to be executed during the run.

## 5.2 SOWFA

Simulator fOr Wind Farm Applications (SOWFA), is based upon the Open-source CFD toolbox OpenFOAM. SOWFA adds necessary utilities in order to simulate a wind turbine, which are the actuator disk model (ADM) and actuator line model (ALM). SOWFA also includes tools to initialize an ABL, convert precursor boundary data to inflow data and adds new or improved LES models suitable for the ADM and ALM models. Using

OpenFOAM with SOWFA enables us to simulate the ABL for different stability cases and compute the wake of the NREL offshore 5-MW wind turbine. The NREL 5-MW turbine is a three bladed wind turbine and its specification can be found at [25].

### 5.2.1 Governing equations

One of the solver used in this thesis is called the ‘ABLSolver’. This solver can be used for either RANS or LES, however in this thesis LES is used. The governing equations to simulate the fluid dynamics are the incompressible and spatially filtered Navier-Stokes equations. The incompressible, spatially filtered continuity equation, can be seen in equation 5.1.

$$\frac{\partial \bar{u}_i}{\partial x} = 0, \quad (5.1)$$

here  $\bar{u}$ , represents the spatially filtered velocity vector. The instantaneous velocity vector  $u_i = \bar{u}_i + u'_i$ , where  $u'_i$  is the sub-filtered velocity vector.

The incompressible, filtered momentum equation can be seen in equation 5.2 [10].

$$\frac{\partial \bar{u}_i}{\partial t} + \frac{\partial}{\partial x_j} (\bar{u}_i \bar{u}_j) = -2\varepsilon_{i3k} \Omega_3 \bar{u}_k - \frac{\partial \tilde{p}}{\partial x_i} - \frac{\partial}{\partial x_i} \left\langle \frac{\bar{p}_0(x, y)}{\rho_0} \right\rangle - \frac{\partial}{\partial x_j} (\tau_{ij}^D) - g_3 z \frac{\partial}{\partial x_i} \left( \frac{\rho_k}{\rho_0} \right) + \frac{1}{\rho_0} f_i^T \quad (5.2)$$

Where the first and second term on the l.h.s. are respectively the rate of change and convection. On the r.h.s. the first term is the Coriolis force due to planetary rotation. The equation for the Coriolis force is actually given by equation 5.3.

$$F_{coriolis} = -2\varepsilon_{ijk} \Omega_j \bar{u}_k, \quad (5.3)$$

$$\Omega_j = \omega \begin{bmatrix} 0 \\ \cos \phi \\ \sin \phi \end{bmatrix}, \quad (5.4)$$

where  $\varepsilon_{ijk}$  is the alternating tensor,  $\omega$  is the planetary rotation rate and  $\phi$  the latitude. However with the assumptions that  $\Omega_1 = 0$ ,  $\bar{u}_3$  is small and the vertical Coriolis force is neglectable. With these assumptions the Coriolis force is reduced to  $-2\varepsilon_{i3k} \Omega_3 \bar{u}_k$ , which can be seen in equation 5.2. The second term is the pressure gradient normalized with the density, hence  $\tilde{p}$ . The third term is the horizontal-mean driving pressure gradient, where  $\rho_0$  is the constant air density. The fourth term are the viscous and SGS/Reynolds stresses. The fifth term is the buoyancy, to account for buoyancy while assuming a incompressible flow Boussinesq’s approximation is used. Here  $g_3$  is the gravitational constant. The last term are forces that are normalized with the density, such as the forces from the actuator line model.

The last equation is the filtered potential transport equation 5.5.

$$\frac{\partial \bar{\theta}}{\partial t} + \frac{\partial}{\partial x_j} (\bar{u}_j \bar{\theta}) = -\frac{\partial}{\partial x} (q_j) \quad (5.5)$$

Where the first term on the l.h.s is the rate of change of the filtered potential temperature, where  $\bar{\theta}$  is the filtered potential temperature. The second term is the convection. The term on the r.h.s is the viscous and SGS/Reynolds temperature fluxes, where  $q_j$  is the temperature flux.

Depending on the case that is ran, different boundary conditions are required. For example, the precursor simulation has cyclic boundary conditions for the lateral planes. While simulating with a turbine the inlet plane is set to time-varying boundary conditions, with the saved slices from the precursor simulation as inlet.

## 5.3 Uniform flow

The wind turbine wake will be first computed for a case with uniform flow. This case will be used as benchmark against the cases where the ABL is present. This way it can be seen what physics is added due to the presence of the ABL. It will also be compared with the Jensen-Gaussian model. It should be noticed that an uniform flow case does not exist in reality.

### 5.3.1 Case setup

The wake for the uniform case is computed using LES with the ALM. The ALM will simulate the NREL-5MW turbine. Some of the turbine specifications can be found in table 5.1. The bounded dynamic Lagrangian turbulence model will be used. This turbulence model is chosen, because it is also suitable for the case where the ABL is introduced. It was found that some other turbulence models gave convergence issues during the computation of the wake when the ABL is introduced. The effect of different turbulence models is not investigated, because it out of the scope of this thesis.

**Table 5.1:** NREL 5-MW turbine specifications

Parameter	Value	Unit
Rating	5	[MW]
Hub height	90	[m]
Roter diameter	126	[m]
Cut-In, Rated, Cut-Out speed	3, 11.4, 25	[m/s]
Rated Tip Speed	80	[m/s]

The wind turbine is placed in a rectangular domain. The horizontal domain has a downstream distance and lateral distance of respectively 3000 *m* and 1500 *m*, while the domain has a vertical distance of 1000 *m*. To capture the far wake an uniform grid of  $\Delta 10$  *m* is implemented. However to capture the near wake, the grid is locally refined twice around the wind turbine, resulting in a grid size of  $\Delta 2.5$  *m*.

The incoming flow is set to 8 *m/s*, just as was done in chapter 4. A suitable time step needs to be chosen. For the ALM it is required that during a time step, the turbine blade

does not pass more than one grid cell in either the  $y$  and  $z$ -direction. Thus the time step depends on the rotation speed and grid size of the turbine. In appendix A, it can be seen that the rotor speed for an inflow speed of  $8 \text{ m/s}$  is equal to  $9.1 \text{ rpm}$ . In order to satisfy the time step requirement, with a  $\text{rpm}$  of  $9.1$  and radius of  $63 \text{ m}$ , a time step of  $0.022 \text{ s}$  is necessary. For the ALM in SOWFA also the number of blade points and Gaussian parameter  $\epsilon$  need to be decided. Typically the distance between two blade points needs to be less than grid size around the turbine. The blade has a size of  $30 \text{ m}$ , thus the number of blade points is set to  $32$  to satisfy the requirement. The blade force also needs to be projected on the flow. SOWFA makes use of a Gaussian projection on the grid, where  $\epsilon$  controls the Gaussian width. As a rule of thumb  $\epsilon$  can be approximated by multiplying the grid size with a factor two. Using the rule of thumb results in  $\epsilon = 5$ .

Once the simulation starts a suitable time needs to be chosen to start averaging the flow. It is chosen to start averaging when the flow has passed the domain at least twice. With an uniform flow with a velocity of  $8 \text{ m/s}$  and downstream domain length of  $3000 \text{ m}$ , the time to average is set to  $750 \text{ s}$ . The variables are outputted after every  $50$  turbine rotations. With  $9.1 \text{ rpm}$  the variables are outputted every  $330 \text{ s}$ . With these settings the flow can be simulated.

### 5.3.2 Results

The results of the LES are compared with the Jensen-Gaussian wake model. In order to compute the velocity with the Jensen-Gaussian wake model it is necessary to have an ambient T.I. However for an uniform case the T.I. is equal to zero by definition. It can be seen in equation 3.5, that the ambient turbulence intensity should be known in order to compute  $k$ , the rate of the wake expansion, and thus the velocity deficit in the wake. Thus in order to compute the velocity deficit with the Jensen-Gaussian model, it was chosen to just use the initial  $k$  computed with equation 2.45. Using the initial conditions from table 5.2, the velocity deficit in the wake is computed. The results of the Jensen-Gaussian wake model is compared with the results of SOWFA, which can be seen in figure 5.1.

When comparing the wake model with SOWFA at  $4D$  downstream, it can be concluded that at the location of the hub, the wake model has a larger velocity deficit. This can be explained by the fact that the wake model is only valid for the far wake. This means that in an uniform case, the breakdown of the tip vortex has not yet occurred at  $4D$  downstream. At  $7D$  downstream the wake model and SOWFA are in better agreement with each other, especially in the region of the hub location. However it can be seen that the wake model slightly underestimates the wake recovery. This could be due to the fact that the wake expansion depends on the ambient turbulence intensity, which can be seen in equation 3.5. Since the ambient T.I. is zero in the uniform case, this cannot be computed, resulting in a slower recovery of the wake. In contrast at  $10D$  the velocity deficit is slightly overestimated by the wake model. This can also be attributed due to neglecting the ambient T.I. The T.I. in the wake depends on the downstream distance, which can be seen in equation 3.4. The T.I. in the wake dampens further downstream, thus lowering the recovery rate. It can be concluded that for an uniform case, the wake model matches the shape of the wake simulated in SOWFA. However the velocity deficit is slightly underestimated. It was noticed that it is important to have a correct ambient

T.I. The T.I. in the wake depends on downstream distance and will influence the recovery of the wake, which is important to match the velocity deficit.

**Table 5.2:** Initial conditions Uniform flow

Parameter	Value	Unit
$U_0$	8	[m/s]
$D$	126	[m]
$C_T$	0.80	[-]
$z_0$	0.002	[%]

## 5.4 ABL

The case where there is uniform flow in the atmospheric boundary layer does not exist. The velocity profile depends on the stability of the ABL. During a diurnal cycle the stability of the ABL changes, three different cases are identified: stable, neutral and unstable stratification. A brief explanation of stability can be found in section 2.2. It was identified that each stability case has a different velocity profile thus wind shear, different turbulence intensity in stream-wise, span-wise and vertical direction and turbulent stress. These flow characteristics play an important role in the development of the wind wakes and specifically the wake velocity and wake recovery rate. Thus it is necessary to validate the ABL stability cases, before performing the wake analysis.

The computation of the turbine wake in the ABL will consist of two phases: The first phase is to run a LES to solve the ABL. To simulate different stabilities of the ABL, the initial values for the wall temperature flux ( $q_3|_{wall}$ ) and boundary layer height ( $\delta$ ) are varied. Also an initial velocity and temperature profile are needed to initialize the ABL. The solver then computes the atmospheric turbulent wind velocities. This so called 'precursor simulation' is ran until quasi-equilibrium is reached. After quasi-equilibrium is reached, the inlet planes are saved for each time-step. Depending on the wind direction, different inlet planes need to be saved. During the second phase, wind turbines are placed in the precursor flow field, which is initialized from the moment quasi-equilibrium is reached. The saved planes are used at the inlet as boundary conditions, which will act as the 'time-varying boundary' condition.

### 5.4.1 Precursor setup

The first step for the precursor is to solve the flow field until quasi-equilibrium is reached for the stable, neutral and unstable ABL. The results obtained from the ABL solver presented by SOWFA will have to be validated. The results will be compared and validated with the results from the paper by Akbar and Porté-Agel [2].

The initial conditions that are used in the paper can be seen in table 5.3. It should be noted that the boundary layer height  $\delta$  is given, however in SOWFA you have to specify the inversion layer thickness and the center location of the inversion layer thickness. The

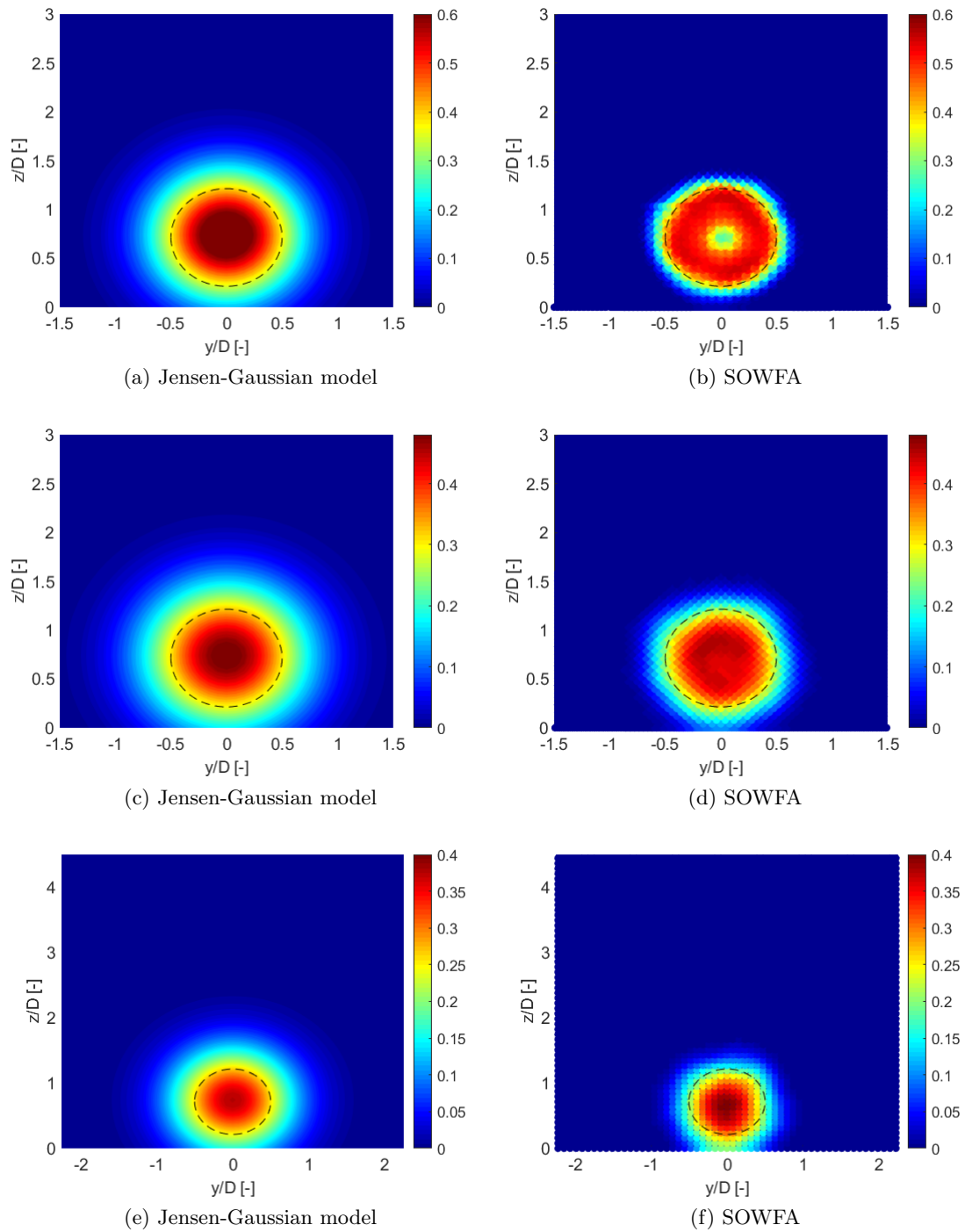


**Figure 5.1:** Comparison between SOWFA and Jensen-Gaussian wake model, top is 4D downstream and middle is 7D downstream and bottom is 10D. The dashed line is the turbine location

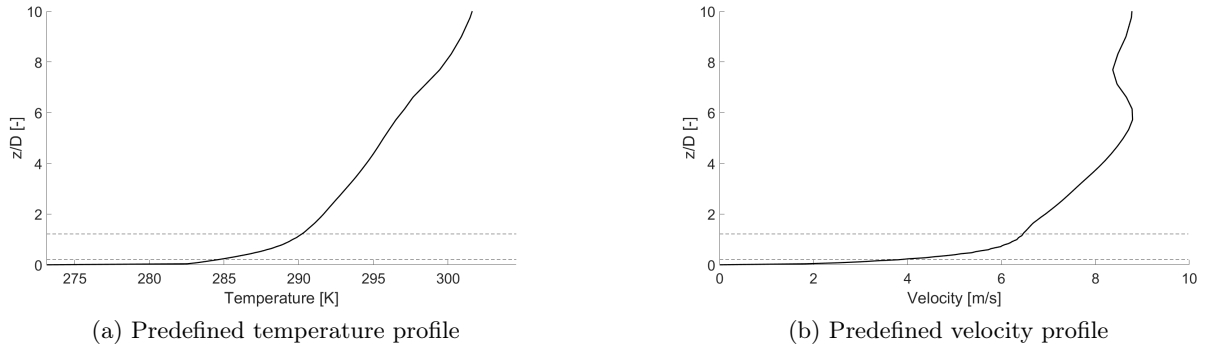


**Figure 5.2:** Predefined profiles by SOWFA, the dashed lines represent the upper and lower blade tip

start of the inversion layers height caps the height of the ABL. An inversion layer thickness of  $100\text{ m}$  is used and the center of the boundary layer height is equal to the values in table 5.3. The solver should match a velocity of  $8\text{ m/s}$  at hub height. Akbar Porté-Agel use a Vestas-V80 windturbine, with a hub height of  $70\text{ m}$ . The roughness length for each case is  $0.05\text{ m}$ . There are two important parameters that are not given in the paper: the initial temperature and velocity profile. SOWFA gives two options for the initial temperature profile. The first option is to use a preset temperature profile given by SOWFA, which is plotted in figure 5.2. The second option is to set an uniform temperature up until the start of the inversion height. From there until the upper part of the inversion height, the temperature increases towards a given value, and afterwards increases with a constant temperature gradient. There are also two options available for the velocity profile. The first one is a predefined velocity profile, which can be seen in figure 5.2. The second option is to initialize a velocity profile based upon the logarithmic velocity equation 2.1. Where  $u_*$  is computed by equating the velocity to  $8\text{ m s}^{-1}$  at hub height.

**Table 5.3:** Initial parameters used solve the ABL

Stability	$q_3 _{wall}$	$\Delta$	$u_*$
Unstable	-0.048	750	0.46
Neutral	0	500	0.4
Stable	0.015	250	0.31

Using the predefined velocity and temperature profile, the ABL flowfield for the three stability cases are computed. A domain of  $3000\text{ m}$ ,  $1500\text{ m}$  and  $1000\text{ m}$  is used, in respectively the x, y and z-direction, with a uniform grid size of  $\Delta 10\text{ m}$ . The simulation is ran until quasi-equilibrium is reached. Quasi-equilibrium can be defined as the moment when the velocity at half the boundary height fluctuates around a mean. The time to reach quasi-equilibrium varies with each stability case.

### 5.4.2 Validation ABL precursor

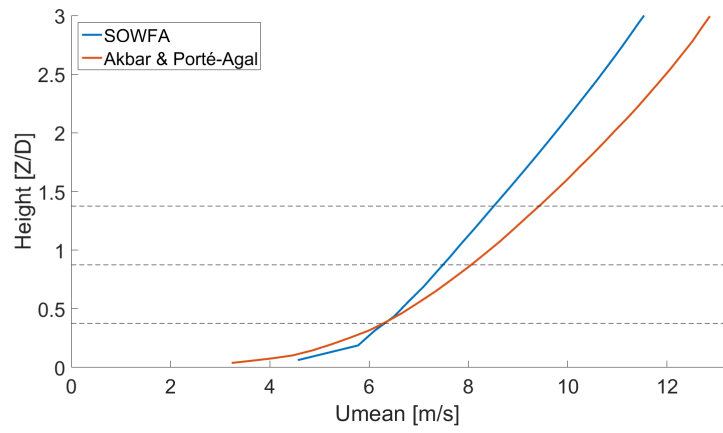
The SOWFA ABL solver automatically averages certain variables, such as the velocity, in the x- and y-direction. The averaged variables are then given as a function of time and height. To assure quasi-equilibrium, each case is ran for 50000s. The velocity profiles for the three stability cases are compared with the results obtained from Akbar and Porté-Agel [2].

The velocity profile obtained from the solver is averaged over a time-span of 2000s, after reaching quasi-equilibrium. The velocity profiles are compared with the results in the paper, which can be seen in figure 5.3. It can be noticed that for each stability case the velocity profile is not in agreement with the results obtained by Akbar and Porté-Agel. The difference between the results of the paper and SOWFA can especially be seen in the neutral case. Where Akbar and Porté-Agel is in good agreement with the law of the wall, this does not seem to be the case for SOWFA's simulation. This is an important indication that the neutral case is not simulated correctly. The stable and unstable case, which can be seen in figure 5.3a and 5.3c, seem to be in better agreement with the results from the paper than the neutral case. However there is still a disagreement between the results. There could be a number of reasons that SOWFA does not match the results of Akbar and Porté-Agel; the difference in the solver, quasi-equilibrium has not been reached, or wrong initial conditions for the velocity and temperature profile. It can be assumed that there will always be slight differences between the SOWFA solver and the solver described in [2]. However the neutral case should at least match the law of the wall.

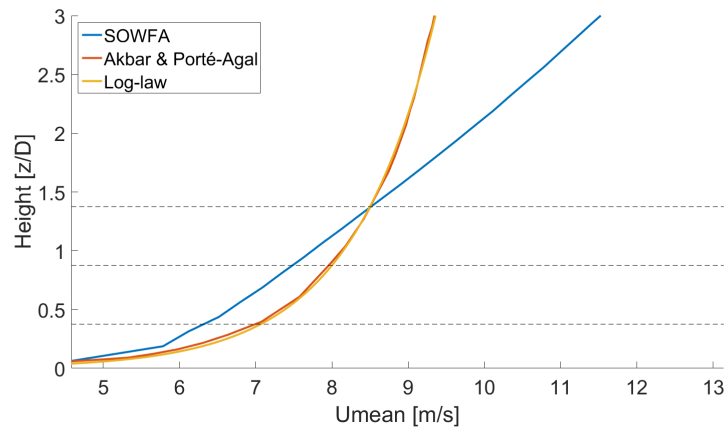
First it will be checked if quasi-equilibrium has been reached. It is assumed that quasi-equilibrium is reached, when the velocity at half the boundary layer height fluctuates around a mean. It is known that the more stable the ABL is, the longer it takes to reach quasi-equilibrium. According to Churchfield [11] it takes around 50000s for the stable case to reach quasi-equilibrium, which indicates that the neutral and unstable case should have reached quasi-equilibrium before 50000s. To validate if each case has actually reached quasi-equilibrium, the velocity at half the boundary layer height is plotted against time. The results can be found in figure 5.4. It can be concluded that the precursor simulations, for the the neutral and unstable ABL, have reached quasi-equilibrium when simulating for 50000s. Further more it can be concluded that the precursor simulation for neutral and unstable reach quasi equilibrium, around respectively 25000s and 15000s. For the stable case, it can be see that around 45000s the velocity starts to fluctuate around a mean. This agrees with the observations made by Churchfield. Thus it can be concluded that the difference between the results obtained from SOWFA and the paper by Akbar and Porté-Agel is not due to not reaching quasi-equilibrium.

So the difference between SOWFA's result and the paper could be due to the initial velocity and temperature profile. The precursor simulation will be performed using different initial temperature and velocity profiles. For the temperature, an uniform temperature of 293K across the domain is used, up until the boundary height from where it is increased to 295.5K. The velocity profile is based upon the logarithmic law 2.1, where the velocity at hub height should match  $8 \text{ m s}^{-1}$ . The temperature and velocity profile can be seen in figure 5.5.

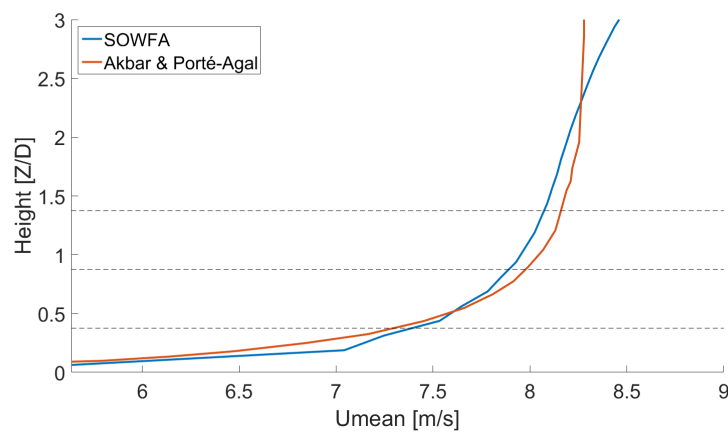
The resulting velocity profiles and temperature profiles for the three stability cases can be seen in figure 5.6. For the stable case it can be seen, in figures 5.6a and 5.6b, that



(a) Stable case

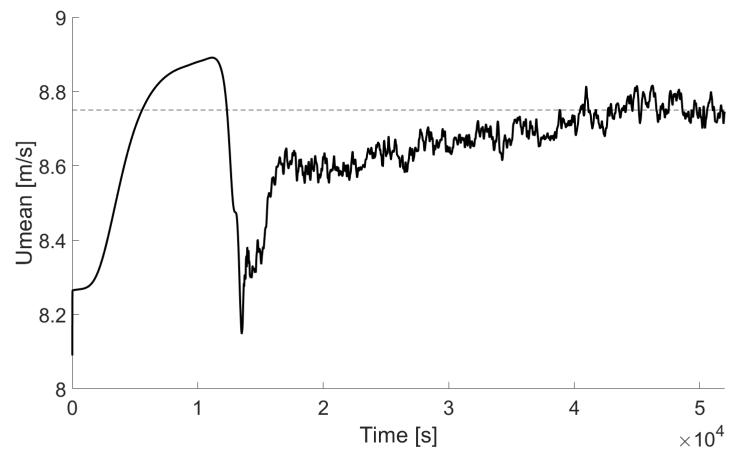


(b) Neutral case

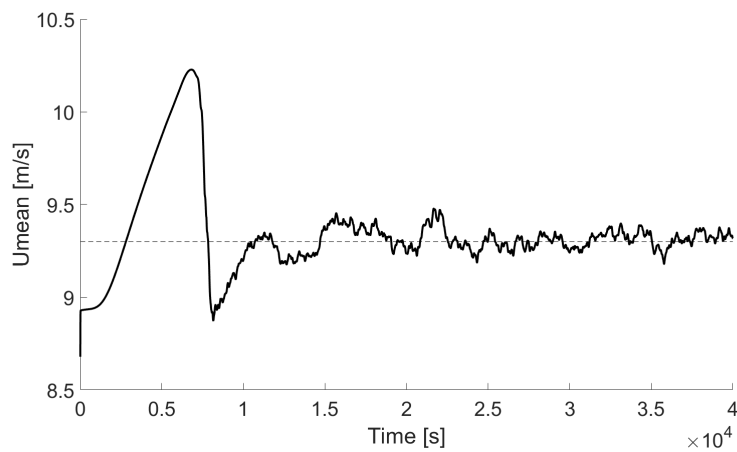


(c) Unstable case

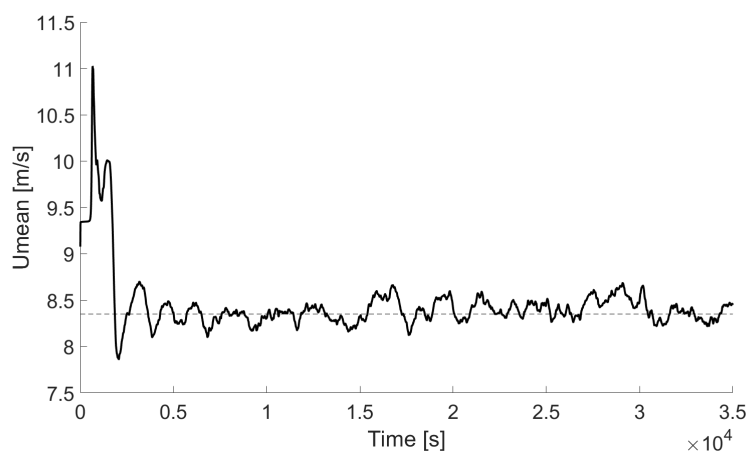
**Figure 5.3:** Comparison between SOWFA and Akbar and Porté-Agal's results



(a) Stable case



(b) Neutral case



(c) Unstable case

**Figure 5.4:** The velocity at half the boundary layer height varying with time

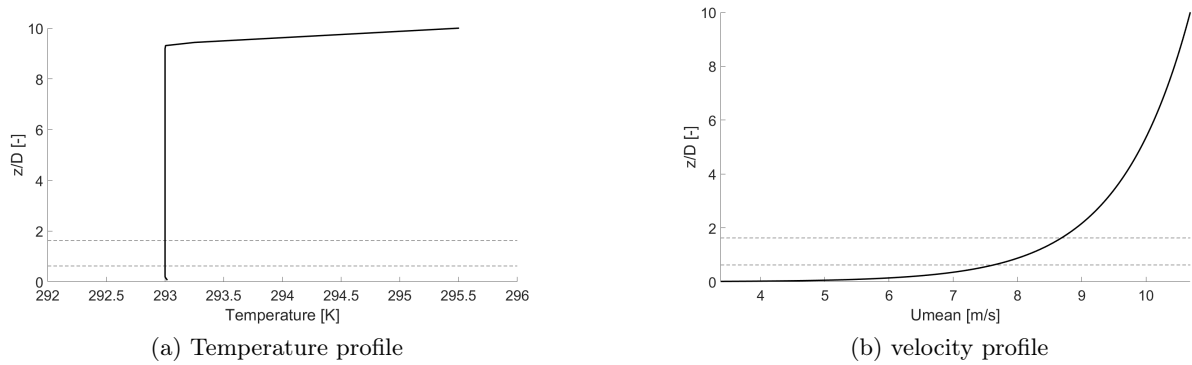


**Figure 5.5:** Temperature profile based upon the boundary depth and logarithmic velocity profile, the dashed lines represent the upper and lower blade tip

there is no improvement in matching the paper. The velocity profile even deviates more with respect to the paper, when comparing it with figure 5.3c. The temperature profile does not match the shape nor the values. The neutral case is in good agreement with the results of the paper. The velocity profile matches the shape of the law of the wall, however there is a slight deviation starting at  $2.5 z/D$ . The temperature profile also shows a good agreement with what is expected of the neutral case. Which is an uniform temperature with respect to height. The temperature and velocity profile for the unstable case can be seen in figures 5.6e and 5.6f. The shape of the velocity profiles matches, but the values start to deviate at hub height. The same can be said for the temperature profile, it has the same shape however there is a mismatch of 3 degrees.

In conclusion it can be said, that using the same initial and boundary conditions in SOWFA as in the paper results in a different stable ABL. The stable case has both a different velocity and temperature profile. In contrast the neutral velocity profile and temperature profile shows to be in good agreement with the paper. The unstable case shows the same trend-line, however there is a small mismatch in the actual values. Following the conclusion it will be tried to match the values in the neutral and unstable case by playing around with the parameters which were uncertain. Also ways to simulate a stable ABL in SOWFA will be investigated.

To get a better match for the neutral and unstable case, it is tried to play around with the initial values that were not specifically given, such as the temperature and boundary layer height location. The temperature for the unstable case will be decreased by  $3 K$  to a value of  $296 K$ , since this is the temperature difference between the temperature profiles of the paper and SOWFA. Also the boundary layer heights will be increased, since in SOWFA when using  $\delta$  it is actually the middle of the boundary layer height which might not be the same location as in the paper. It will be increased, such that the boundary layer height starts at the values found in table 5.3. For the neutral case, instead of  $\delta = 500m$  as mentioned in the paper, it is chosen to increase it. Two cases have been simulated, with  $\delta = 700m$  and  $\delta = 800m$ . Using a inversion layer thickness of  $100m$ , the actual boundary layer height in SOWFA equals  $600m$  and  $700m$ . It can be seen in figure 5.7, that increasing the boundary layer height in SOWFA results in gaining a velocity profile that is in good agreement with the results mentioned in the paper. In particular the case

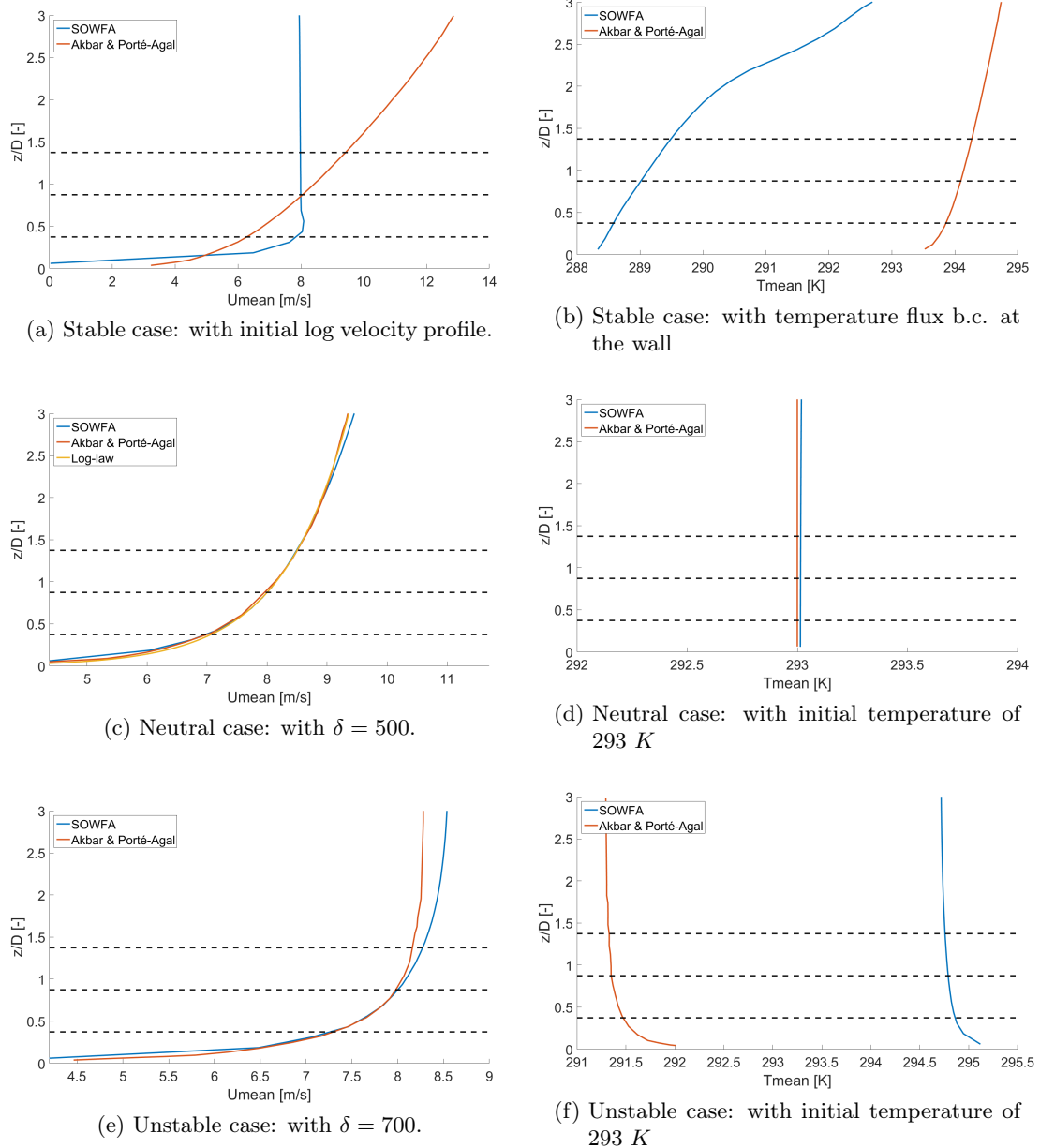


**Figure 5.6:** Comparison between SOWFA's and Akbar & Porté-Agal ABL precursors.

where  $\delta = 800m$  is in good agreement.

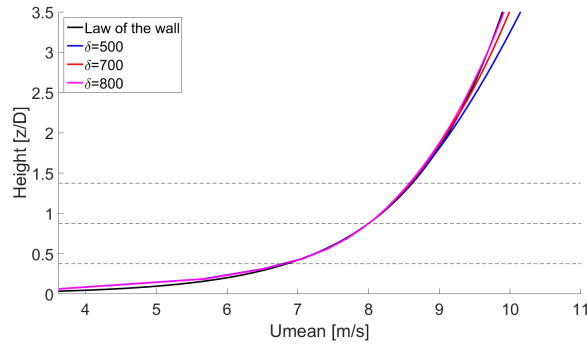


**Figure 5.7:** Neutral ABL: Law of the wall comparison with SOWFA cases with varying  $\delta$

For the unstable case it is first tried to see if matching the temperature profile at quasi-equilibrium will result in a velocity profile that is in better agreement with the results of Akbar and Porté-Agel. As you can see in figure 5.8, the temperature profile is in good agreement when the initial temperature is reduced. However there is no improvement in matching the velocity profile, which can be seen in figure 5.9. The second option is to use the same approach that was used in the neutral case: increasing the boundary layer height  $\delta$ . Noticing that in the neutral case an increase of  $200m$  achieved the best result, it is also used in this case. The result can be seen in figure 5.9. It can be seen that by increasing the boundary layer height  $\delta$ , will result in a good agreement between the velocity profiles.

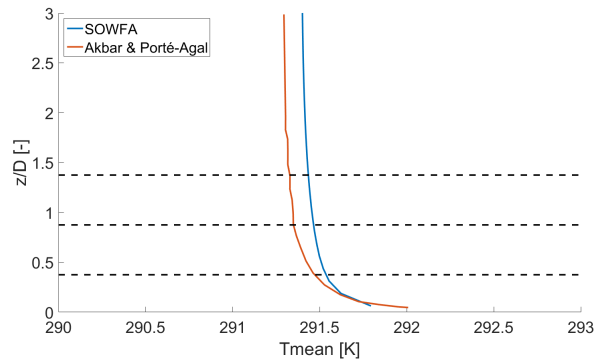


**Figure 5.8:** Unstable ABL: Temperature profile by reducing initial temperature

To be able to simulate a stable ABL in SOWFA a different approach is required. It is found that in SOWFA the b.c. at the wall has to be chosen differently. It is necessary to use a rate of change of temperature instead of a temperature flux as b.c. at the wall, this is described in the paper by S. Basu et al. [7]. As mentioned in the paper, an iterative approach is used to compute the temperature flux from the rate of change of temperature. Since it is not possible to compute the temperature flux from the given rate of change of temperature manually, it is chosen to use a typical rate of change of temperature for the stable case. The rate of change of temperature for the stable case is set to  $5.6e^{-5}K/s$ , which is a typical value for the stable ABL according to Churchfield [11]. Since it was noticed that the boundary layer height  $\delta$  should be higher for the neutral and unstable

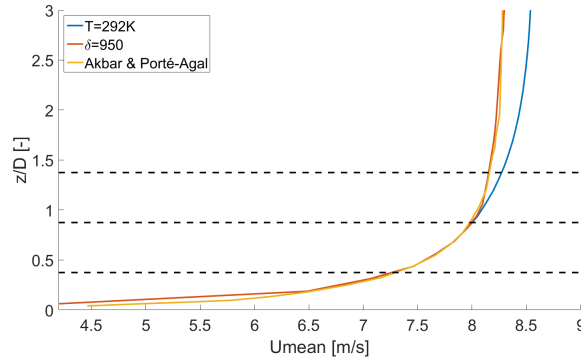


**Figure 5.9:** Unstable ABL: Velocity profile by reducing initial temperature and increasing boundary layer height

case, it is decided to increase it as well for this case. For this case it is chosen to use a  $\delta = 350$  instead of the value from table 5.3. The results can be seen in figure 5.11. It can be seen in figure 5.11a that using a rate of change of temperature as b.c. in SOWFA, yields results that are in better agreement with the paper. The temperature profile does not exactly result in the same temperature values, however the shape does match. The reason the values do not match could be due to the fact that the the temperature flux of table 5.3 is not the same as the temperature flux of  $5.6e^{-5}K/s$ . The velocity profiles are in good agreement with each other up until  $2D$ . As seen before the boundary layer height plays an important role in matching the results of the velocity profile. Increasing  $\delta$  even more could result in a better match of the velocity profile.

Besides the temperature and velocity profile also the turbulence intensity in streamwise, spanwise and vertical direction and kinematic shear stress between SOWFA and Akbar and Porté-Agel can be compared. On the left side In figure 5.10 the turbulence intensity of Porté-Agel can be compared with the results obtained from SOWFA on the right side. It can be noticed that for the streamwise turbulence intensity SOWFA shows the same profile as Akbar and Porté-Agel. However the values at lower tip, hub height and upper tip are overestimated for the stable case. The maximum difference between the paper and SOWFA in this region is 15%. For the neutral case, between the lower and upper tip region, the values are in good agreement. The maximum difference occurs at hubheight and is 5%. Close to the wall the streamwise turbulence intensity overshoots. This could be the fact that the grid size is too coarse, which makes it unable to capture a correct turbulence intensity close to the wall. The streamwise turbulence intensity for the unstable stability case has the largest maximum difference of the three stability cases. The maximum difference in the unstable case is 18%. For the spanwise turbulence intensity it can be seen that the stable and neutral case are in good agreement. The unstable case however shows a large difference between the paper and SOWFA. The vertical turbulence intensities seem to be in good agreement with each other. When comparing the kinematic shear stress it can be immediately be noticed that the neutral and unstable case have much larger values when computed in SOWFA. The stable case is in good agreement with the results of the paper.

It can be concluded that SOWFA is capable of simulating a stable, neutral and unstable atmospheric boundary layer. However the initial conditions used in the paper of Akbar

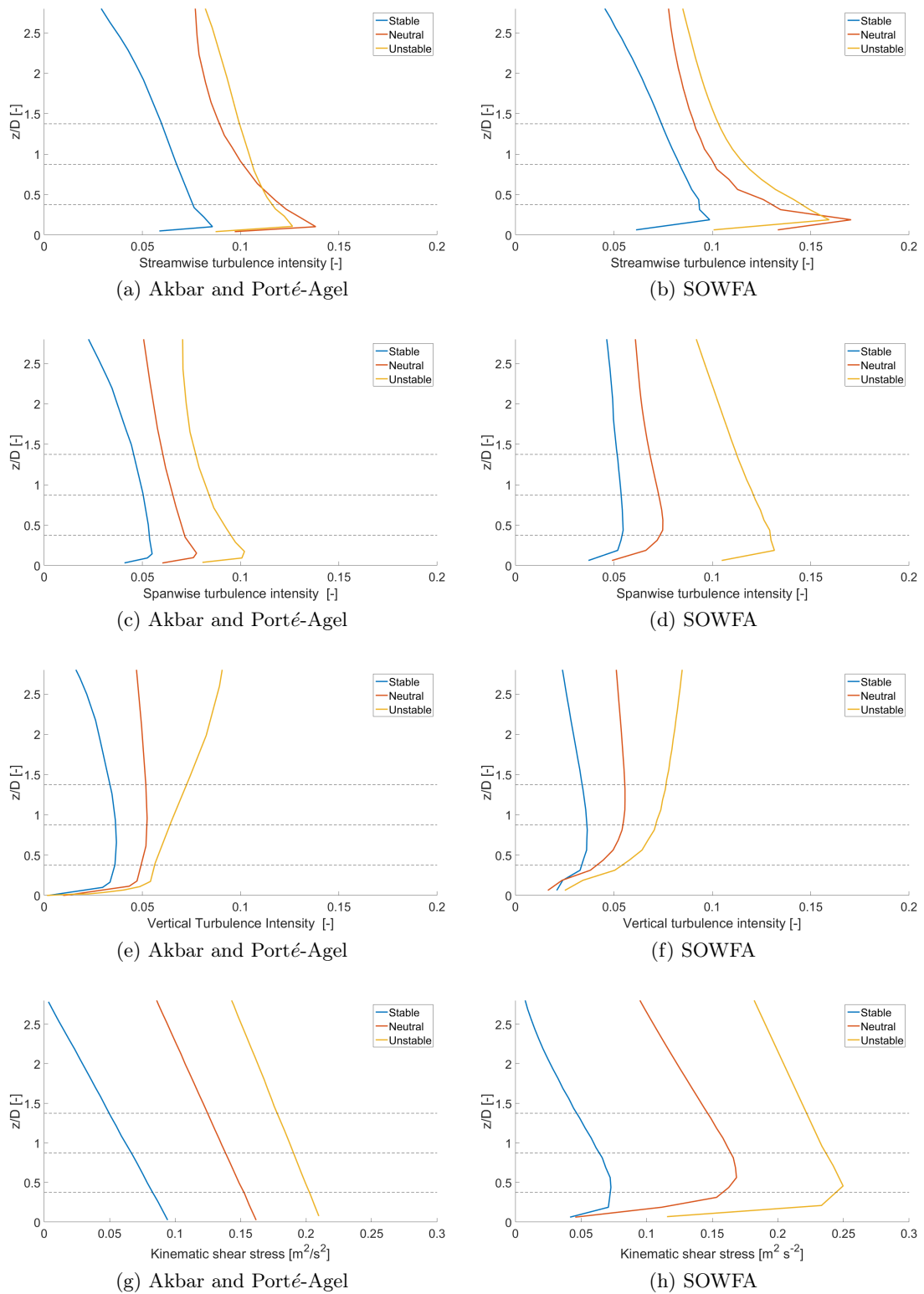


**Figure 5.10:** Comparison between SOWFA's and Akbar & Porté-Agel ABL turbulence intensity

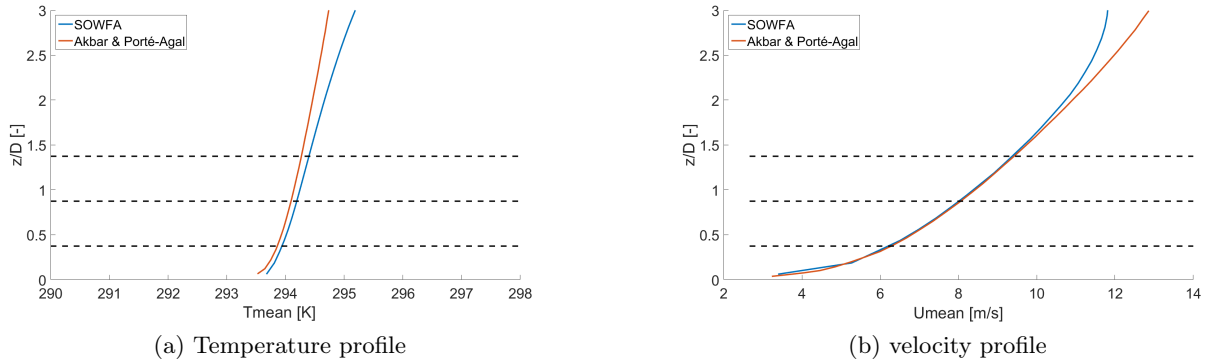


**Figure 5.11:** Stable case: Temperature and velocity profile using temperature flux as b.c.

and Porté-Agel do not yield the same results in SOWFA. To match the temperature and velocity profile with SOWFA, it is important to increase the boundary layer height  $\delta$  for all three stability cases. The boundary layer height mentioned in the paper of Akbar and Porté-Agel [2] should be increased by 200m. Also in SOWFA it is important to use a rate of change of temperature as b.c. at the wall for the stable case, but a temperature flux for the neutral and unstable case. Also the initial temperature and velocity profile must be chosen carefully for all three cases.

### 5.4.3 Wind turbine case setup

The ABL precursor simulation that was validated in section 5.4.2 will not be used to perform the turbine wake analysis. The ABL precursor simulation of the paper of Akbar & Porté-Agal [1] was set to match a velocity of 8 m/s at hub height for the Vestas V-80 wind turbine. In SOWFA this wind turbine is not available, only the NREL 5-MW wind turbine is available. The specification of this NREL 5-MW wind turbine can be found in table 5.1. It can be seen that the hub height for the NREL 5-MW is 90m. Thus the three stability cases will be set to match 8 m/s at 90m height. Taking into consideration the findings of section 5.4.2, the NREL 5-MW turbine and characteristics of the Horns Rev Offshore Wind Farm the precursor simulation is performed. The initial conditions used to simulate the three stability cases can be found in table 5.4. The same domain used in section 5.4.2 will also be implemented here. The resulting velocity, temperature, turbulence intensity and kinematic shear stress profiles for the three stability cases can be seen in figure 5.12. The resulting profiles are in line with what is expected of each stability case. The unstable case has the highest turbulence intensity and an uniform velocity profile in the turbine region. While the stable case has the lowest turbulence intensity and the largest velocity gradient. Using these precursor simulation the NREL 5-MW turbine wake is computed.

The second phase after the precursor simulation consists of introducing the wind turbine into the precursors flow field and creating the inflow slice data from the precursor simulation. The wind turbine is modeled using the actuator line method. The undisturbed velocity at hub height is 8m/s, which results in a fixed RPM of 9.1 according to appendix A. The RPM for the NREL 5-MW turbine will be a fixed value. The time step, averaging

time and number of blade is the same as in section 5.3.1. It is chosen to use the same mesh of the ABL precursor simulation, which has a uniform size of  $\Delta 10m$ . It is chosen to copy the precursor mesh instead of mapping the variables onto a new mesh for the turbine case. It was noticed that mapping onto a new grid in SOWFA caused the solution to diverge. Because the ABL mesh is used, it needs to be refined twice. This due to the fact that a grid size of  $\Delta 2.5m$  is needed around the wind turbine, which was also mentioned in section 5.3.1. The mesh is locally refined twice around the turbine, using the built-in command "RefineHexMesh". This refines a hex mesh by 2x2x2 cell splitting. The mesh gradually increases from  $\Delta 2.5m$  to  $\Delta 5m$  in the near wake and to  $\Delta 10m$  at 6D downstream in the far wake. With a RPM of 9.1, minimum grid size of  $\Delta 2.5 m$  and turbine diameter of  $126m$ , the time step is set to  $0.02s$ .

To start computing the wind turbine wake in SOWFA, the ABL precursor simulation also needs to be processed. The momentum source and temperature source files need to be created. This is done by using the source data conversion tools provided by SOWFA. These files are linked with the wind turbine case. The inlet planes are linked and also created using the SOWFA boundary data conversion tools. The last step is to change the boundary conditions of the flow variables. During the ABL precursor simulation the east and west b.c. are set to cyclic. However to be able to simulate the turbine wake when introducing the ABL, the boundary conditions need to be changed. The b.c. of the west inlet plane are set to timeVaryingMappedFixedValues, which indicate that the planes obtained from the precursor simulation are used for the inlet. The east b.c. is set to inletOutlet, which is almost the same as a zero-gradient b.c., but switches to a fixed value when backwards flow occurs. After these pre-processing steps, the wind turbine case with an ABL is almost ready to be simulated. The final thing is to chose a LES model. OpenFOAM has a number of LES models readily available. However when some LES models are implemented it results in diverging solutions. It was out of the scope of the thesis to investigate the impact of the different LES models. It was chosen to use the dynLagrangianCsBound LES model, this model was developed for SOWFA.

**Table 5.4:** Initial parameters for precursor simulation

Stability	$q_{3 wall}$	$T_{flux}$	$\Delta$	$z_0$	$t_{sim}$
Stable	-	$5.6e^{-5}$	950	0.002	50000
Neutral	0	-	700	0.002	25000
Unstable	-0.048	-	450	0.002	15000

#### 5.4.4 Turbine wake analysis

After setting up the ABL with the ALM the simulation can be started. The simulation is run for  $2000s$  and the variables start averaging when the flow has passed the domain twice, which is around  $660s$ . Plotting the turbine wake and analyzing the results, important factors will be incorporated into the analytical Jensen-Gaussian wake model.

The contours of the time-averaged streamwise velocity at hub-height and through the center of the turbine are plotted for all three stability cases and can be seen in respectively

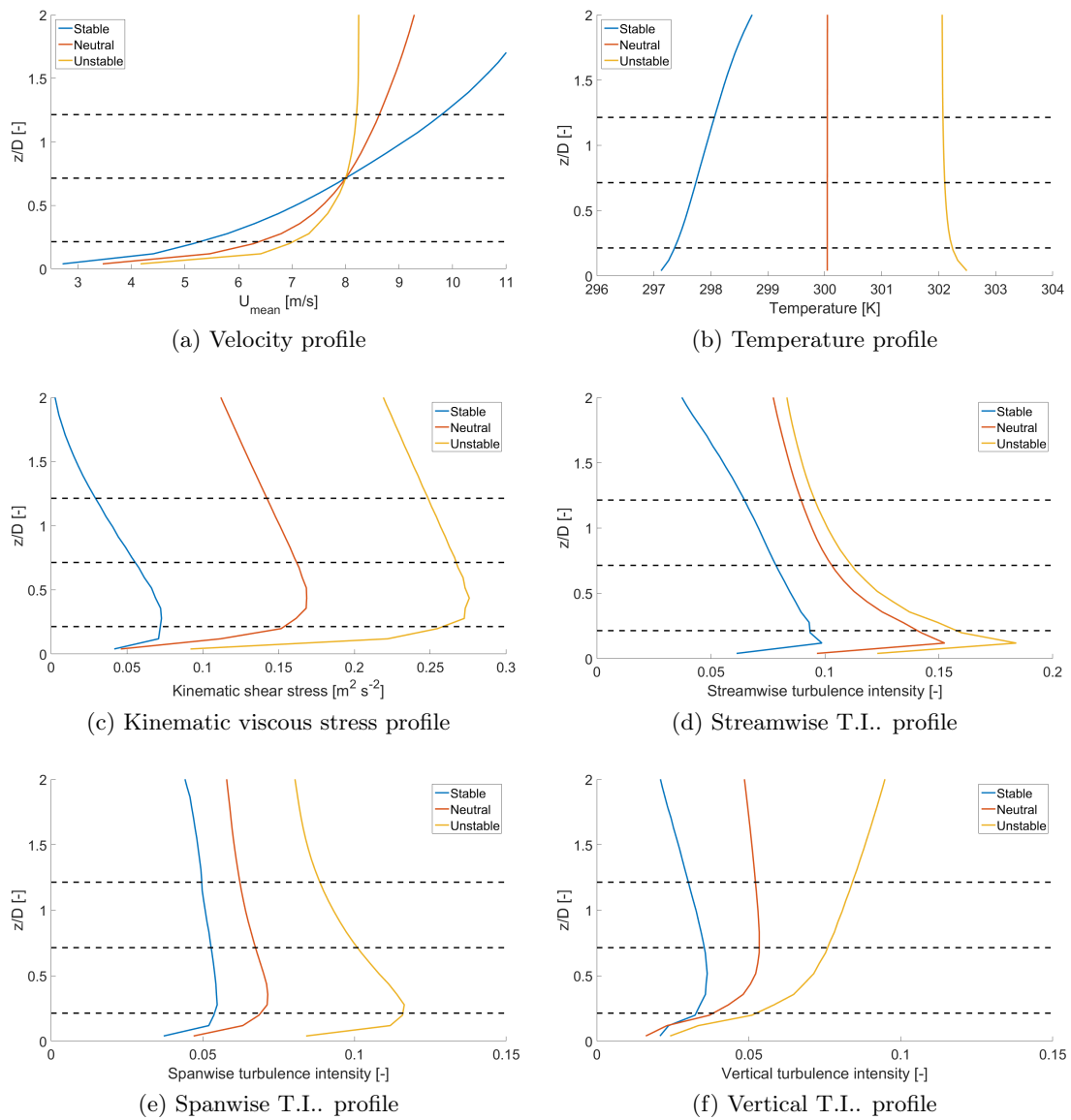


**Figure 5.12:** Results of the precursor simulation for the three stability cases

figures 5.13 and 5.14. First thing that can be noticed from the  $x-y$  plane and  $x-z$  plane in figures 5.13 and 5.14, is that the wind turbine wake recovers fastest in the unstable case and takes the longest distance in the stable case. This is as expected, because in the unstable case the turbulence intensity is higher and the wake should recover faster. This is due to the fact that in the unstable case the heating at the wall causes thermal instabilities, which increases the turbulent kinetic energy thus increasing the turbulent mixing. While the opposite can be said for the stable case. The surface cools down, resulting in a downwards buoyancy flux, thus in a reduction of the turbulent mixing. The difference in the rate of wake recovery for the three stability cases should be taken into account when using an analytical wake model. The analytical Jensen-Gaussian wake model 2.44 takes into the account the turbulence intensity which controls the rate of recovery of the wake. The analytical model however only takes the streamwise turbulence intensity into account. It could be important to also take the lateral and vertical component into consideration. The difference between the stream-wise T.I. of the neutral and unstable case is only 1%. However for such a small difference between the turbulence intensities, the wake for the unstable condition recovers much faster than can be accounted for. The difference in the spanwise and vertical turbulence intensity between the neutral and unstable condition is much larger, which could indicate that it is important to also take these into account.

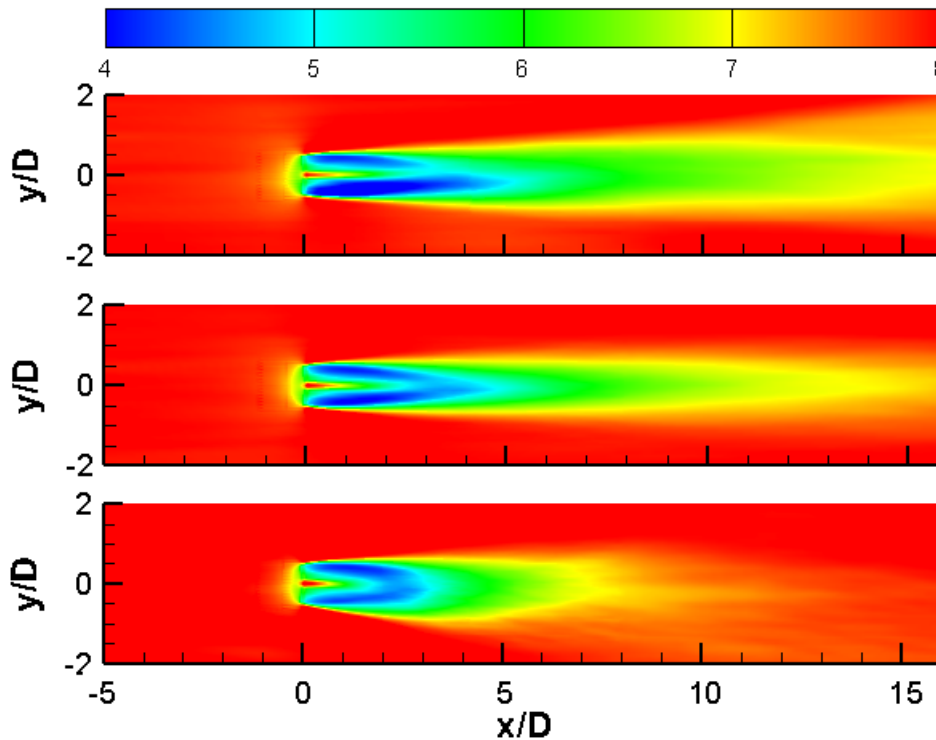


**Figure 5.13:** Time-averaged streamwise velocity component in the  $x-z$  plane.

The contours of the normalized time-averaged streamwise velocity deficit in the  $y-z$  plane computed by SOWFA for the stability conditions, can be seen in figures 5.15 and 5.16. As seen in figures 5.15 and 5.16 two things can be noticed. First it can be seen that the resulting wakes for the stability cases are not axi-symmetrical. The wake seems to have an elliptical and not circular shape. Second it can be seen that there is a rotation of the

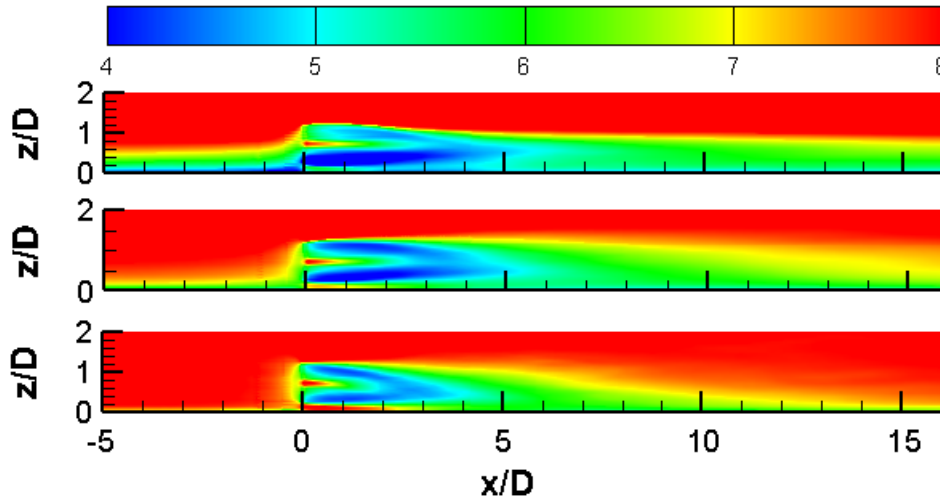


**Figure 5.14:** Time-averaged streamwise velocity component in the  $x - z$  plane.

elliptical shaped wind turbine wake, which depends on the stability condition of the wake. The unstable case for example does not have a rotation angle, while the neutral and stable conditions are rotated. An explanation for the elliptical shape could be due to the fact that the turbulence intensity in lateral direction is larger than in vertical direction. As a result the wake might expand faster in the lateral direction than the vertical direction. Also the presence of the ground might obstruct the expansion of the wake in vertical direction. The different rotation angles of the elliptical wake can be explained by analyzing the differences in the velocity profiles for the stability conditions, see figure 5.12a. The unstable velocity profile has a very small velocity gradient in the turbine region. In contrast, the neutral and stable case have a stronger velocity gradient in this region. This indicates that the upper region has higher energy flow than the lower regions. Due to the clockwise rotation, the higher energy upper region are mixed with the lower region and other way around. This could be an explanation for the rotation in the wake shape. It is also noticed that the unstable wake shape does not start in at the turbine center. This could be due to the wrong time-averaging in the unstable case. This can also be found in the  $x - y$  plane, where you can see that the wake has a slight yaw angle.

From the contour plots of the time-averaged streamwise velocity deficit, three important phenomena need to be taken into consideration. First is that the stability cases have a different rate of wake recovery, the more unstable the case the faster the wake recovers. Second is that the axi-symmetrical circular shape of the analytical wake model needs to be adjusted to match an elliptical shape. Third is that the elliptical wake is rotated with an angle around the  $x$ -axis, where the angle depends on the stability condition. In order to extend the analytical wake model for different stability conditions, it is chosen to characterize the stability cases with the parameter  $\alpha$  from equation 2.2. The parameter  $\alpha$  is chosen such that it matches the ABL velocity profiles of figure 5.12a. The values for  $\alpha$  are 0.34, 0.12, 0.02 for respectively the stable, neutral and unstable conditions and the plots can be seen in figure 5.17. It can be seen that the power law is in good agreement with the ABL velocity for the neutral and stable condition. However for the unstable condition the power law can't match the ABL velocity profile over the full height. However the

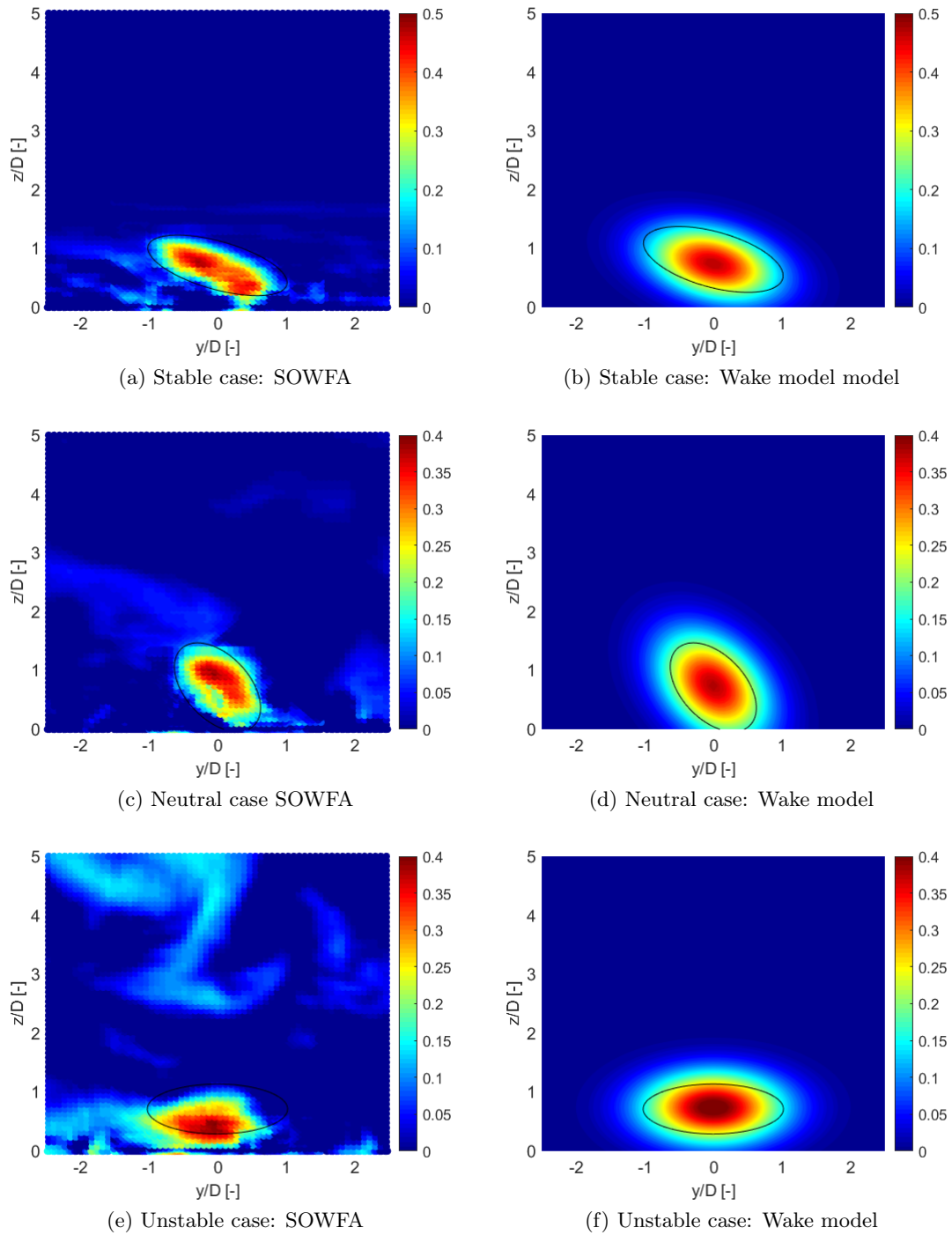


**Figure 5.15:** Comparison of the normalized time-averaged streamwise velocity deficit  $4D$  downstream, between SOWFA and the extended Jensen-Gaussian wake model.

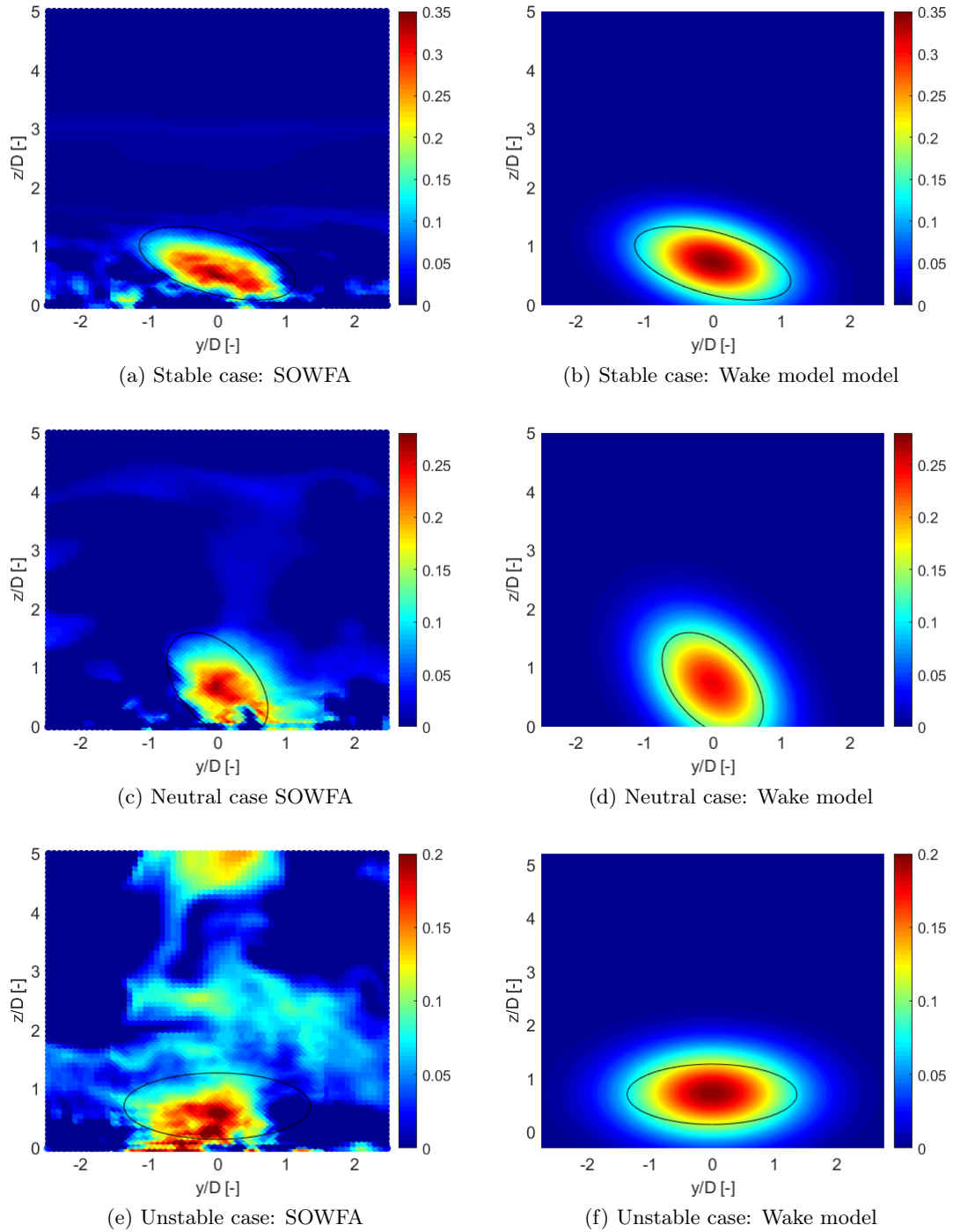


**Figure 5.16:** Comparison of the normalized time-averaged streamwise velocity deficit  $7D$  downstream, between SOWFA and the extended Jensen-Gaussian wake model.

parameter  $\alpha$  is chosen such for each stability condition that is in good agreement at the turbine region. The maximum error found in each case in the turbine region was around 1.5%.

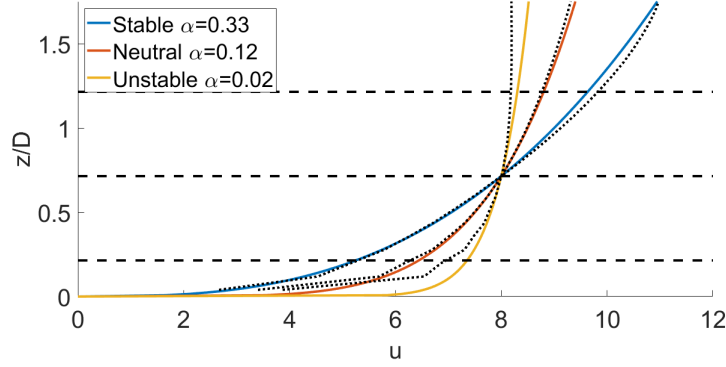


**Figure 5.17:** Velocity profile for the stability conditions based upon the power law

The analytical jensen-Gaussian wake model equation will be extended by substituting the following equations in equation 2.44:

$$r^2 = x^2 + y^2, \quad (5.6)$$

$$\begin{aligned} x' &= x \cos \varphi + y \sin \varphi, \\ y' &= -x \sin \varphi + y \cos \varphi, \end{aligned} \quad (5.7)$$

$$1 = \frac{x^2}{a^2} + \frac{y^2}{b^2}, \quad (5.8)$$

$$\sigma = \sqrt{\sigma_x \sigma_y}, \quad (5.9)$$

where equation 5.6 is used to convert the radius into x and y coordinates, since the Jensen-Gaussian wake model only depends on the radius due to the axi-symmetrical shape. Equation 5.7 is used to rotate the Jensen-Gaussian wake model counter clockwise with angle  $\phi$  w.r.t. the z-axis. Working in Cartesian coordinates will make it easier during the optimization of the wind farm layout. Equation 5.8 is used to transform the axi-symmetrical circular wake model into an elliptical shaped wake. Where  $a$  is the semi-major axis and  $b$  is the semi-minor axis of the elliptical shape. Using the relationship in equation 5.9, the semi-major axis and semi-minor axis can be expressed in relationship with the standard deviation  $\sigma$ . Where  $\sigma$  is equal to:

$$\sigma = \frac{r_x}{2.58}. \quad (5.10)$$

These equations results in the extended Jensen-Gaussian elliptical wake model, which can be seen in equation 5.11:

$$u_{deficit} = (u_0 - u_*) \cdot \frac{5.16}{\sqrt{2\pi}} \cdot \exp\left(\frac{\frac{\sigma_x}{\sigma} \cdot (x \cos \varphi + y \sin \varphi)^2 + \frac{\sigma_y}{\sigma} \cdot (x \sin \varphi - y \cos \varphi)^2}{2 \cdot \left(\frac{r_x}{2.58}\right)^2}\right), \quad (5.11)$$

where  $u^*$  can be found in equation 2.44.

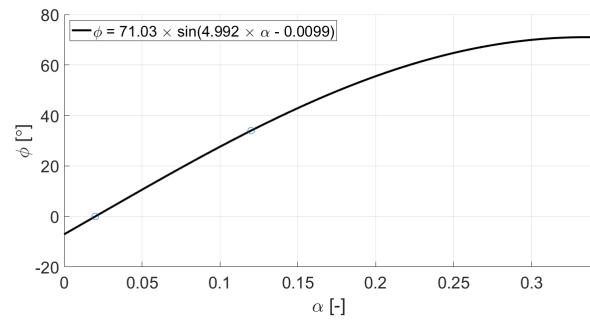
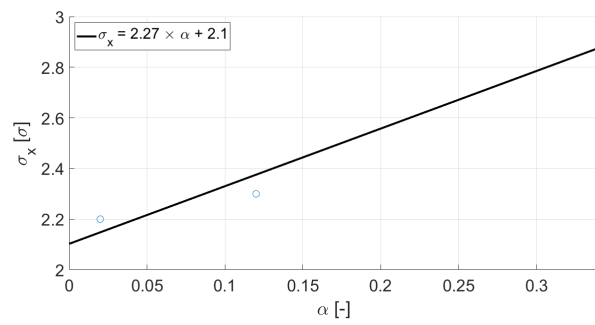
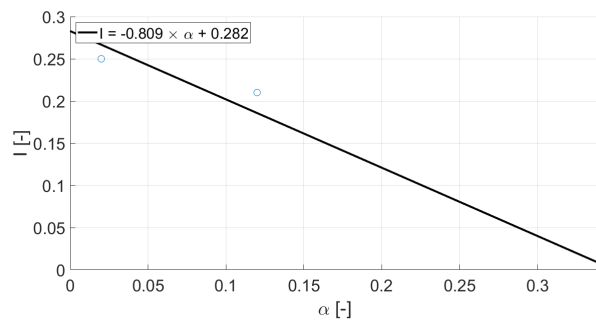
To match the shape for each stability case, the values for the parameters  $a$ ,  $b$  and  $\phi$  need to be found. To take this rate of recovery into account it is chosen to add an % turbulence intensity  $I_{stability}$  depending on the stability case. These values are found by iterating for each stability condition and comparing the analytical wake model with the results obtained from SOWFA. In table 5.6 the parameter values for the extended wake model can be found. These parameters are plotted against the stability parameter  $\alpha$ , which can be seen in figure 5.18. Using the stability parameter  $\alpha$ , the wake for each stability condition can be computed. Using the parameters from table 5.6 with the initial conditions from table 5.5, the wake can be computed with the extended Jensen-Gaussian elliptical wake model. The contours of the velocity deficit downstream in the far wake can be seen in figures 5.15 and 5.16. It can be noticed that the extended wake model does follow the shape and contour values for the neutral and stable cases. The stable case seems to have a longer part with higher velocity deficit than the wake model computes. The neutral case seems to be in better agreement with the SOWFA results, when comparing it to the other two stability cases. However in neutral conditions, the velocity deficit seems to be slightly overestimated for a larger area by the wake model. The unstable case however does not seem to be in agreement. The most important observation for the unstable case, is that in SOWFA the wake center is not aligned with the center of the turbine. This could be due to the wake meandering. The averaging time was taken the same for each case, which was 50 rotations of the turbine, which amounts to 330s. It could be that the periodic movement of the wake meandering did not complete a integer number of periods, resulting in a time-averaged velocity that seems to have a yaw angle. What is also observed that at 4D the unstable and neutral case, seem to have the same velocity deficit, however the unstable case recovers faster when comparing the velocity deficit at 7D.

**Table 5.5:** Initial conditions for each stability conditions

Parameter	Value	Unit
$U_0$	8	[m/s]
$D$	126	[m]
$C_T$	0.80	[-]
$Z_0$	0.002	[%]

**Table 5.6:** Initial parameters used to compute the turbine wake according to the extended Jensen-Gaussian elliptical wake model

Stability	$\alpha$	$\phi$	$\sigma_x$	$I_{stability}$
Unstable	0.02	0	$2.2\sigma$	0.25
Neutral	0.12	34	$2.3\sigma$	0.21
Stable	0.34	71	$2.9\sigma$	0

(a)  $\alpha$  vs rotation angle  $\phi$ (b)  $\alpha$  vs semi-major axis  $\sigma_x$ (c)  $\alpha$  vs added stability turbulence intensity  $I_{stability}$ **Figure 5.18:** Curve fits for  $\alpha$  vs the extended Jensen-Gaussian elliptical wake parameters

## 5.5 Conclusion

It can be concluded that using the ALM in SOWFA for an uniform flow case results in a wake that has an axi-symmetrical shape. The results obtained from the analytical Jensen-Gaussian wake model is in good agreement for the uniform flow case. However it is important to include the ambient T.I. and added T.I. to achieve better results. It can also be concluded that SOWFA is capable of simulating different ABL stabilities. It is however important to use different b.c. during the precursor simulation to obtain the different stability cases. In the stable case a rate of change of temperature at the wall is required, while in the neutral and unstable cases a wall temperature flux is needed. Also proper initial velocity and temperature profiles are required during the precursor simulation. When including the different stability characteristics of the ABL in SOWFA, the wake has a different shape and rate of recovery in comparison to the uniform case. It can be concluded that the stability of the ABL has an important effect on the wind turbine wake development. First thing noticed is, that the more stable the ABL is the longer it takes to recover. This is due to the fact that turbulence intensity becomes higher for more unstable ABL. Comparing the uniform case with all three of the stability cases, it can be seen that the turbine wake does not have an actual circular shape, but it has an elliptical shape. This could be explained by the difference in T.I., in the spanwise and vertical direction. But also due to the presence of the ground. There also seems to be a rotation angle  $\phi$  of the ellipse, which depends on the stability. The rotation angle  $\phi$  could be attributed to the velocity profile of each stability case. The rotation of the wind turbine causes the high potential energy to mix with the low potential energy in the lower region. The more stable the case, the bigger the difference is between the lower part and upper part of flow across the turbine. Using the extended Jensen-Gaussian wake model yields decent results when comparing it to the results obtained from SOWFA. However for the unstable case it was difficult to get the results in good agreement, because of problems with finding a suitable averaging time.

# Wind Farm Layout Optimization

In this chapter the empirical model that was derived in chapter 5 is implemented in a Wind Farm Layout Optimization (WFLO) algorithm. First the optimization algorithm will be discussed, second the case for which the wind farm will be optimized will be described, third the empirical model will be used to compute the optimal wind farm layout and finally the results for each stability case will be discussed.

## 6.1 Optimization algorithm

The optimization algorithm that will be used is the mixed-discrete Particle Swarm Optimization (MDPSO) algorithm with explicit diversity-preservation developed by Chowdhury et al [9]. The optimization algorithm written by Chowdhury tries to minimize a certain variable. The objective is to reduce the power loss of the wind farm. The power produced by the most upfront wind-turbine is the reference value for which the power efficiency of the downstream wind turbines are calculated. According to the incoming flow velocity at hub height the power is computed by using the NREL-5MW power curve. The power curve can be found in figure 6.1.

The MDPSO chooses a layout depending on the domain size, number of wind turbines and minimum distance between turbines. The total wind farm power will depend on the wind rose direction, wind speed for the wind rose directions, type of wind turbine, wake model and introduced in this thesis, the stability condition. For a given layout the turbines are sorted from most upfront till most downstream turbine, and are numbered one till  $n$  number of turbines. The most upfront turbine depends on the direction of the incoming wind. First for the most upfront wind turbine, which is not affected by any turbine wakes, the power output is calculated with figure 6.1. For the remaining downstream turbines the velocity deficit due to the upfront turbine needs to be computed. It is first checked whether they are inside the wake of this turbine or not. If a turbine is inside the wake of an upfront turbine, it needs to be computed how much of the turbine area is inside the wake. The calculation of the overlap area can be performed analytically by direct integration

of the area between the elliptical shaped wake and circular turbine. However, due to the difficulty of analytically computing the overlap area and to reduce the computational cost, the area is computed numerically. It is chosen to discretize the circular turbine and elliptical shaped wake in pixels and using pixel counting to compute the overlap area. With the following algorithm the pixels in the overlap area are computed and the area weighted velocity is calculated. It is known that equation 6.1 holds for coordinates inside an ellipse and equation 6.2 for a circle:

$$\frac{y^2}{a^2} + \frac{z^2}{b^2} < 1, \quad (6.1)$$

$$y^2 + z^2 < r^2. \quad (6.2)$$

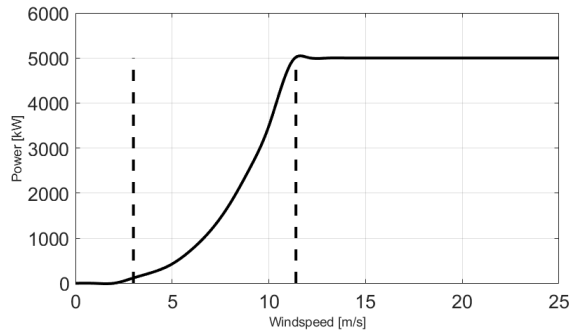


**Figure 6.1:** NREL-5MW power curve:  $P - U$ , where the dashed lines represent the cut-in speed and rated speed.

The turbine rotor area is discretized according to the findings in chapter 4.2.1. The coordinates of the turbine rotor area are put into a matrix and using equations 6.1 and 6.2, each entry is flagged one when it is inside the circle and ellipse, zero otherwise. To compute the total overlap area the matrix is summed and multiplied with the pixel area. The ratio between the overlap area and total turbine area is computed. Zero being no overlap and one being fully in the wake. The velocity deficit at hub height is then computed using the analytical wake model. The area overlap ratio is then multiplied by the velocity deficit at hub height and is then used as the velocity deficit due to the upfront turbine. It should be noticed that this method is derived from using the Jensen wake model, where a top hat profile is used. However in this case the wake has neither a top hat or axis-symmetrical shape. However it is chosen to use this method since it is used in most of the optimization algorithms, due to its fast computation time. This process is iterated until the velocity deficit at each downstream turbine has been computed. The algorithm then computes the velocity of the second upstream turbine and the power generated. This power is divided by the power generated of the most upfront turbine to calculate the power efficiency. The above described process is iterated until the power of each wind turbine has been computed. This process is repeated for each wind direction in the wind rose, with a given wind speed and wind frequency. This is weighted and averaged according to the frequencies of each wind sector to compute the total wind farm power efficiency for the given layout. The MDPSO then optimizes the layout and the process is repeated for a

given amount of iterations. The optimization flow chart can be found in appendix B. The most global optimal layout is then given based upon the total power efficiency.

## 6.2 Results optimization: Horns REV OWF

As described in chapter 5.4.4, it was chosen to simulate the ABL precursor for the Horns Rev offshore wind farm. This results in a roughness length ( $z_0$ ) of 0.002 m as initial condition for the ABL precursor simulation. The optimization algorithm takes into consideration the different flow velocities at hub height and wind flow directions during the yearly cycle of the ABL. The wind speed and weights were measured by remote sensing observation and reported by Hasager [23]. The wind speed and weights can be seen relatively in figures 6.2 and 6.3. Horns Rev has 80 wind turbines on a oblique rectangle of 5km by 3.8km. However to reduce computation time it is chosen optimize for a smaller domain of the wind farm. It is chosen to use 1.5km by 2.2km for 12 turbines. Which almost amounts to the same area per wind turbine available. The optimization problem is ran first for the analytical Jensen-Gaussian wake model to find the optimal layout according to the MDPSO algorithm. The optimization algorithm is repeated for the extended Jensen-Gaussian wake model, which takes into account the different stabilities of the ABL. These four layouts should be the optimal layout for respectively their own wake model. For each of these four different layouts the averaged total wind power is computed with the four different wake models: Jensen-Gaussian, stable Jensen-Gaussian, neutral Jensen-Gaussian and the unstable Jensen-Gaussian wake model. Using equations 2.44 and 5.11 with the parameters in table 5.6, the wake deficit and thus power output can be computed with respectively the Jensen-Gaussian model and extended Jensen-Gaussian model. Using the MDPSO algorithm the layouts are computed and these are plotted in figure 6.4. For these layouts the total power is computed for each wind direction and weighted with the values found in figures 6.2 and 6.3. Using these weights the total power is averaged and the results can be found in table 6.1 and 6.2.

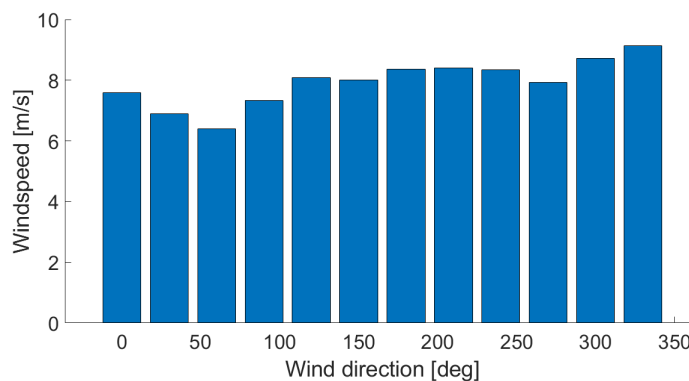


**Figure 6.2:** Annual wind speeds for different wind direction in Horns Rev

Before discussing the results it should be noted that in the ideal situation, each wake model should have the highest averaged total output for their own optimized wind farm layout. It can be noticed that is the case for each model, except for the stable wake model. The optimal layout for the Jensen-Gaussian and neutral wake model, yields a better result

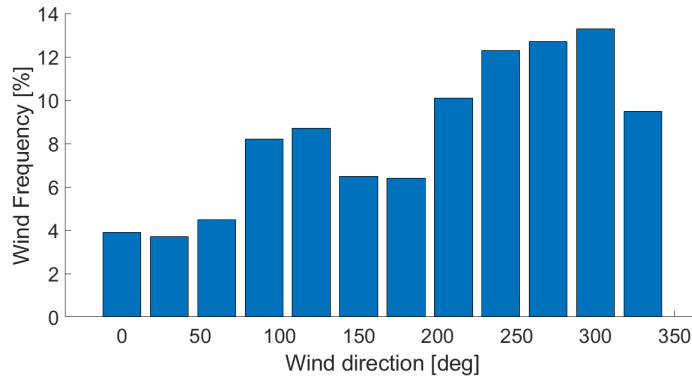


**Figure 6.3:** The annual percentages for each wind sector in Horns Rev

for the stable wake model. It can be seen that the Jensen-Gaussian layout almost has the same power output, however there is a difference of 0.04%. This difference is insignificant in comparison to the uncertainties. In contrast there is 1.4% difference when using the neutral layout. An increase of 1.4% in power output can be significant for a whole wind farm. However due to uncertainties in for example, the computation of the power output using the power curve it can't be known how accurate this increase in total power output is. Also the optimization algorithm should have found the same optimal layout that was found for the neutral wake model. This could indicate that the MDPSO algorithm has its shortcomings. It can be noticed that in case of an unstable wake model the difference in power output for different layouts does not have a significant impact. This could have been expected, since a unstable wake has the fastest recovery. The wind turbines are expected to be located further away in the other cases, however do to faster recovery in the unstable case this difference does have a significant impact. In contrast the optimal unstable layout has does make a difference when used for the other wake models. Because for the unstable wake model, the turbines can be placed much closer to each other due to this faster recovery of the wake.

**Table 6.1:** Wind farm power output [ $kW \cdot 10^6$ ]

Wake-model \ Layout	Layout			
	JensenG	Stable	Neutral	Unstable
JensenG	4.3215	4.3069	4.3204	4.2697
Stable	4.2252	4.2232	4.2842	4.1459
Neutral	4.3000	4.2798	4.3439	4.2488
Unstable	4.3318	4.3558	4.3707	4.3710

### 6.3 Conclusion

It can be concluded that using the different wake models does yield different optimal layouts. However the impact of these different models and layouts on the total power output, needs to be put in perspective. First thing is that optimization algorithm does

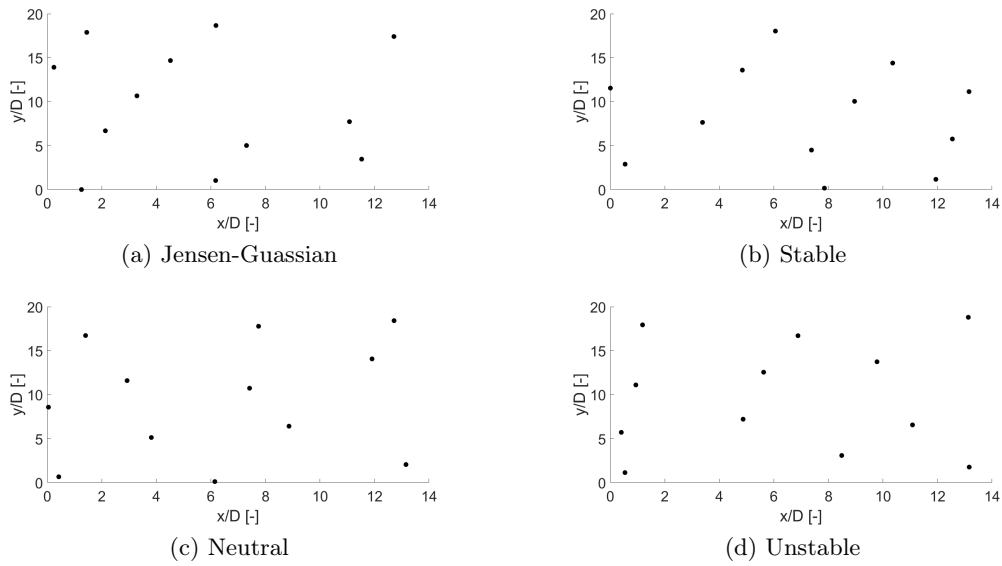


**Figure 6.4:** Optimal layout for the different stability wake models

**Table 6.2:** Wind farm power output percentage difference %

Wake-model \ Layout	JensenG	Stable	Neutral	Unstable
JensenG	-	-0.3378	-0.0255	-1.1987
Stable	0.0474	-	1.4444	-1.8304
Neutral	-1.0106	-1.4756	-	-2.1893
Unstable	-0.6968	-0.3477	-0.0069	-

not always find the optimal layout for the chosen wake model, which is the case for the stable wake model. In this case the Jensen-Gaussian and neutral optimal wind farm layout resulted in a higher averaged total power output than its own optimal layout. The optimization algorithm should have been able to find this optimal layout for the stable wake model. This could indicate that the optimization algorithm stays at a certain local optimum. Another thing is that this difference between the total power output is relatively small when comparing it to the Jensen-Gaussian layout. In contrast a 1.4% power output improvement is found when using the stable model on the neutral layout. This is significant when this is actually achieved in a wind farm. However the power output is computed using the power curve and the computed velocity at hub height. The background and thus reliability of the power curve can be questioned. For actual turbines the power curve is made by measuring the flow velocity on hub height on site and the power of the wind turbine is measured. This is done a repeated a number of times and the power curve is constructed. This means that power curve is based upon the velocity at hub height, however the whole velocity profile over the wind turbine needs to be measured to get a more accurate power curve. What also can be concluded is that the unstable optimal layout does have a negative impact for the other three wake models. While in contrast the other three layouts do not have a great impact on the results for the unstable wake model.

Important is to note that on off-shore wind farms the ABL is much longer stable. The more stable the wake is, the longer it takes to recover. Thus it will be more important to take the layout that is optimized with the stable or neutral wake model for OWF, than optimized with the unstable model. In conclusion the accuracy of the total power output is questionable. To ensure that the results are valid, the power output of the different layouts with different stabilities should be validated using SOWFA. This however requires a lot of computational resources, which is not available at this time but should be carried out in future work.

# Conclusion

### 7.1 Conclusions

The purpose of this thesis was to identify important physical phenomena in a wind farm that could play a role in the optimization of the wind farm layout. During the literature study it was found that wake meandering, yawing are some of the physics that play a role in the computation of the wake. However it was concluded that the stability effect of the atmospheric boundary layer will play a more important role on the wake computation. It was concluded that the Jensen-Gaussian model was most suitable to be extended to include these effects. Due to the fact that it is widely used in preliminary wind farm layout optimization and is computational inexpensive.

Using the parameters and initial conditions encountered on off-shore wind farms the wake was computed with SOWFA. During the analysis of the stability effects on the single turbine wake it was found that there were important differences between the original analytical Jensen-Gaussian wake model and the wake simulated in SOWFA. The wake model was extended to include the effects, such as the faster recovery rate the unstabler the ABL becomes. It was also found that the wake seems to be elliptical and not circular. This could be due to the fact that the turbulence intensity in each direction was different and the presence of the ground obstructing the vertical expansion of the wake. These effects were included in the Jensen-Gaussian wake model.

Using the mixed-discrete Particle Swarm Optimization, the optimal wind farm layouts were computed for an off-shore wind farm. The different layouts were then used to compute the averaged total power for the wake model with different stabilities. It was found that the difference using the unstable optimal layout yielded the largest difference for the other wake models. This difference ranged between 1% and 2%, which in real wind farms could be significant. In contrast the other layouts did not have much impact when using the unstable wake model. The stable wind farm layout did not yield the best result for the stable wake model. The neutral and Jensen-Gaussian optimal layout yielded a better result for the stable wake model. However the difference between the Jensen-Gaussian and stable layout were insignificant. The results obtained when using the neutral optimal

layout with the stable wake model was around 1.4%. This could indicate that either the optimization algorithm does not always find the optimal layout or that it can get stuck at a local optimum. In conclusion it can be said that the stability of the ABL has an important effect on the wake computation and thus the wind farm layout optimization. However the accuracy of the computed total power output for a wind farm layout is questionable. Due to the fact that the power is computed using the power curve. And also due to the fact that the optimization algorithm found a layout for the neutral conditions that yielded better results for the stable wake. It should also be noted that the stability changes during the day. On off-shore wind farms the stability is more stable than on-shore wind farms, thus reducing the effect of the unstable wake model. All in all it is important to take the stability effects on the wake into consideration when designing the optimal layout. Especially for off-shore wind farms, where the ABL is more stable, thus the wake takes longer to recover. This will affect the total output power, which needs to be validated in SOWFA in future work.

## 7.2 Recommendations for future work

There are a couple of uncertainties that have a significant impact on the results of the thesis. The first is that during the validation of the wake model in a wind farm and during the wind farm layout optimization, use is made of the so called power curve. However the background and the derivation of the power curve is not known for each wind turbine. The different layouts and wake models are compared with respect to the total power output, thus uncertainties in the power curve influences the results and thus the conclusion made in this thesis. It is recommended that in future work, when comparing the impact of the different ABL stabilities on the turbine wake, to validate the power curve with the power obtained from SOWFA. This can reduce the error of uncertainty of the computed total power of the wind farms. Another recommendation is to also investigate the turbine wake for multiple aligned wind turbines and miss-aligned wind turbines in SOWFA. One of the shortcomings of this paper is that lack of turbine-wake-turbine investigation. Only the stability effect on a single turbine wake is analyzed and parameterized in the extended Jensen-Gaussian wake model. The last recommendation is to use different optimization algorithms when optimizing for the wind farm layout, this way the effect of the algorithm on the results can be minimized. It was seen that the stable wake model did not yield the best result for its own optimized wind farm layout. This indicates that the optimization algorithm either gets stuck at a certain local optimum or that it does not converge to the right optimum.

---

## References

- [1] Mahdi Abkar and Fernando Porté-Agel. The effect of atmospheric stability on wind-turbine wakes: A large-eddy simulation study. *J. Phys.: Conf. Ser.*, 524:012138, jun 2014.
- [2] Mahdi Abkar and Fernando Porté-Agel. Influence of atmospheric stability on wind-turbine wakes: A large-eddy simulation study. *Physics of Fluids*, 27(3):035104, mar 2015.
- [3] J. F. Ainslie. Wake modelling and the prediction of turbulence properties. *Proceedings of the 8th British Wind energy Association*, 1986.
- [4] J.F. Ainslie. Calculating the flowfield in the wake of wind turbines. *Journal of Wind Engineering and Industrial Aerodynamics*, 27(1-3):213–224, jan 1988.
- [5] R. J. Barthelmie, K. Hansen, S. T. Frandsen, O. Rathmann, J. G. Schepers, W. Schlez, J. Phillips, K. Rados, A. Zervos, E. S. Politis, and P. K. Chaviaropoulos. Modelling and measuring flow and wind turbine wakes in large wind farms offshore. *Wind Energ.*, 12(5):431–444, jul 2009.
- [6] Majid Bastankhah and Fernando Porté-Agel. A new analytical model for wind-turbine wakes. *Renewable Energy*, 70:116–123, oct 2014.
- [7] Sukanta Basu, Albert A. M. Holtslag, Bas J. H. Van De Wiel, Arnold F. Moene, and Gert-Jan Steeneveld. An inconvenient “truth” about using sensible heat flux as a surface boundary condition in models under stably stratified regimes. *Acta Geophysica*, 56(1):88–99, nov 2007.
- [8] Leonardo P. Chamorro and Fernando Porté-Agel. A wind-tunnel investigation of wind-turbine wakes: Boundary-layer turbulence effects. *Boundary-Layer Meteorol.*, 132(1):129–149, apr 2009.
- [9] Souma Chowdhury, Weiyang Tong, Achille Messac, and Jie Zhang. A mixed-discrete particle swarm optimization algorithm with explicit diversity-preservation. *Structural and Multidisciplinary Optimization*, 47(3):367–388, dec 2012.

- [10] Matthew Churchfield. Nawea 2017 training session, September 2017.
- [11] Matthew J. Churchfield, Sang Lee, John Michalakes, and Patrick J. Moriarty. A numerical study of the effects of atmospheric and wake turbulence on wind turbine dynamics. *Journal of Turbulence*, 13:N14, 2012.
- [12] A. Crespo and J. Hernandez. Turbulence characteristics in wind-turbine wakes. *Journal of Wind Engineering and Industrial Aerodynamics*, 61(1):71–85, jun 1996.
- [13] Martin de Maré and Jakob Mann. Validation of the mann spectral tensor for offshore wind conditions at different atmospheric stabilities. *J. Phys.: Conf. Ser.*, 524:012106, jun 2014.
- [14] L.; Crespo A.; Enevoldsen P.; Gómez-Elvira R.; Hernández J.; Højstrup J.; Manuel F.; Thomsen K. Frandsen, Sten Tronæs; Chacón. *Measurements on and modelling of offshore wind farms*. Forskningscenter Risoe, 1996.
- [15] Sten Frandsen. On the wind speed reduction in the center of large clusters of wind turbines. *Journal of Wind Engineering and Industrial Aerodynamics*, 39(1-3):251–265, jan 1992.
- [16] Sten Frandsen, Rebecca Barthelmie, Sara Pryor, Ole Rathmann, Søren Larsen, Jørgen Højstrup, and Morten Thøgersen. Analytical modelling of wind speed deficit in large offshore wind farms. *Wind Energ.*, 9(1-2):39–53, jan 2006.
- [17] Xiaoxia Gao, Hongxing Yang, Lu Lin, and Prentice Koo. Wind turbine layout optimization using multi-population genetic algorithm and a case study in hong kong offshore. *Journal of Wind Engineering and Industrial Aerodynamics*, 139:89–99, apr 2015.
- [18] Xiaoxia Gao, Hongxing Yang, and Lin Lu. Study on offshore wind power potential and wind farm optimization in hong kong. *Applied Energy*, 130:519–531, oct 2014.
- [19] Xiaoxia Gao, Hongxing Yang, and Lin Lu. Optimization of wind turbine layout position in a wind farm using a newly-developed two-dimensional wake model. *Applied Energy*, 174:192–200, jul 2016.
- [20] M. Gaumont, P.-E. Réthoré, S. Ott, A. Peña, A. Bechmann, and K. S. Hansen. Evaluation of the wind direction uncertainty and its impact on wake modeling at the horns rev offshore wind farm. *Wind Energ.*, 17(8):1169–1178, may 2013.
- [21] Torben J. Larsen Gunner C. Larsen, Helge Aa. Madsen and Niels Troldborg. *Wake modeling and simulation*. Wind Energy Division, 2008.
- [22] M.O.L Hansen. *Aerodynamics of windturbines*. Earthscan, 2008.
- [23] Charlotte Bay Hasager, Alfredo Pena, Merete Bruun Christiansen, Poul Astrup, Morten Nielsen, Frank Monaldo, Donald Thompson, and Per Nielsen. Remote sensing observation used in offshore wind energy. *IEEE Journal of Selected Topics in Applied Earth Observations and Remote Sensing*, 1(1):67–79, mar 2008.

- [24] Bo Hu. Design of a simple wake model for the wind farm layout optimization considering the wake meandering effect. Msc. thesis, Technical University Delft, 2016, May 2016.
- [25] W. Musial J. Jonkman, S. Butterfield and G. Scott. Definition of a 5-MW Reference Wind Turbine for Offshore System Development . Technical report, National Renewable Energy Laboratory, 02 2009.
- [26] N.O. Jensen. *A note on wind generator interaction*. DTU, 1983.
- [27] I. Katic, J. Højstrup, and N.O. Jensen. *A Simple Model for Cluster Efficiency*, pages 407–410. A. Raguzzi, 1987.
- [28] Matthew Lackner and Christopher Elkinton. An analytical framework for offshore wind farm layout optimization. *Wind Engineering*, 31(1):17–31, jan 2007.
- [29] G.C. Larsen. *A simple wake calculation procedure*. Ris/o-M. Risø National Laboratory, 1988.
- [30] Gunner Larsen. *Dynamic wake meandering modeling*. Risø National Laboratory, Roskilde, 2007.
- [31] P. B. S. Lissaman. Energy effectiveness of arbitrary arrays of wind turbines. *Journal of Energy*, 3(6):323–328, nov 1979.
- [32] Amin Niayifar and Fernando Porté-Agel. A new analytical model for wind farm power prediction. *J. Phys.: Conf. Ser.*, 625:012039, jun 2015.
- [33] Alfredo Peña and Ole Rathmann. Atmospheric stability-dependent infinite wind-farm models and the wake-decay coefficient. *Wind Energ.*, 17(8):1269–1285, may 2013.
- [34] Alfredo Peña, Pierre-Elouan Réthoré, and M. Paul van der Laan. On the application of the jensen wake model using a turbulence-dependent wake decay coefficient: the sexbierum case. *Wind Energ.*, 19(4):763–776, may 2015.
- [35] Samina Rajper and Imran J. Amin. Optimization of wind turbine micro-siting: A comparative study. *Renewable and Sustainable Energy Reviews*, 16(8):5485–5492, oct 2012.
- [36] Douwe J. Renkema. Validation of wind turbine wake models. Msc. thesis, Technical University Delft, 2007, june 2007.
- [37] B. Sanderse. Aerodynamics of wind turbine wakes. *Energy research Centre of the Netherlands*, 2015.
- [38] R.C. Storey, J.E. Cater, and S.E. Norris. Large eddy simulation of turbine loading and performance in a wind farm. *Renewable Energy*, 95:31–42, sep 2016.
- [39] Jacob Berg Søren Ott and Morten Nielsen. *Linearised CFD Models for Wakes*. Wind Energy Departmen, 2011.

- [40] G.J. Taylor, National Power (Firm), Department of Energy, Energy Technology Support Unit (Great Britain), National Power Technology, and Environment Center. *Wake Measurements on the Nibe Wind-turbines in Denmark: Data collection and analysis*. Number dl. 2 in Contractor Report. National Power, Technology and Environment Centre, 1990.
- [41] Sorensen T. Nielsen P. Grotzner A. Thogersen, M. L. and S. Chun. *Introduction to wind turbine wake modelling and wake generated turbulence*. DNV/Risø, 2nd ed.: Risø National Laboratory, EMD International A/S (2006).
- [42] Jared Thomas, Eric Tingey, and Andrew Ning. Comparison of two wake models for use in gradient-based wind farm layout optimization. In *2015 IEEE Conference on Technologies for Sustainability (SusTech)*. Institute of Electrical & Electronics Engineers (IEEE), jul 2015.
- [43] Linlin Tian, Wei Jun Zhu, Wen Zhong Shen, Ning Zhao, and Zhiwei Shen. Development and validation of a new two-dimensional wake model for wind turbine wakes. *Journal of Wind Engineering and Industrial Aerodynamics*, 137:90–99, 2015. This work is supported by the National Basic Research Program of China (the “973” program. 2014CB046200), NSFC (grant 91130030) and the Danish Research Council for Strategic Research (DSF sagsnr. 10-094544).
- [44] L.J. Vermeer, J.N. Sørensen, and A. Crespo. Wind turbine wake aerodynamics. *Progress in Aerospace Sciences*, 39(6-7):467–510, aug 2003.
- [45] P. E. J. Vermeulen. An experimental analysis of wind turbine wakes. In H. S. Stephens and C. A. Stapleton, editors, *3rd International Symposium on Wind Energy Systems*, pages 431–450, 1980.
- [46] Rados K Voutsinas S and Zervos A. On the analysis of wake effects in wind parks. *J. Wind Eng.*, 1990.
- [47] Yu-Ting Wu and Fernando Porté-Agel. Atmospheric turbulence effects on wind-turbine wakes: An LES study. *Energies*, 5(12):5340–5362, dec 2012.

---

# Appendix A

---

## NREL-5MW

This appendix contains the steady state respons of the NREL-5MW wind turbine used in SOWFA.

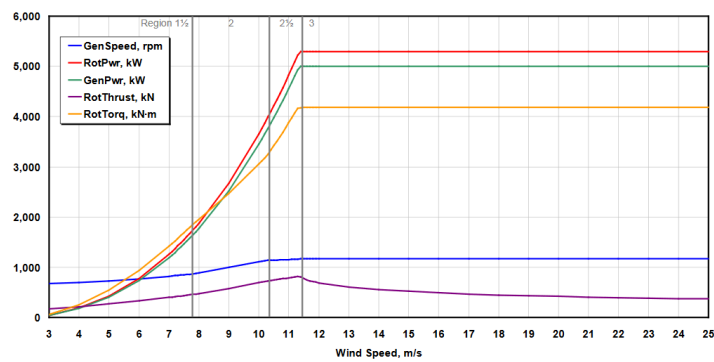


Figure A.1

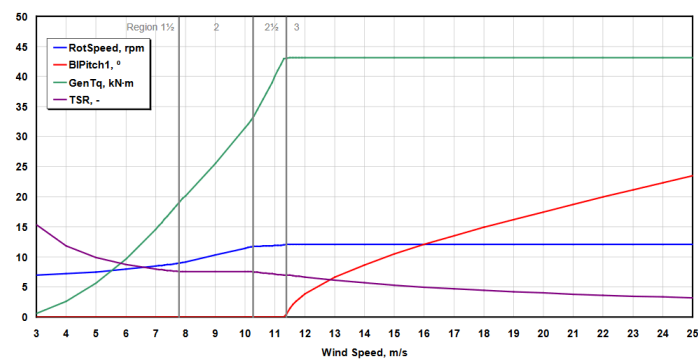


Figure A.2



---

## Appendix B

---

# Flowchart: Optimization algorithm

This appendix contains the flowchart to compute the Optimized Wind Farm Layout.

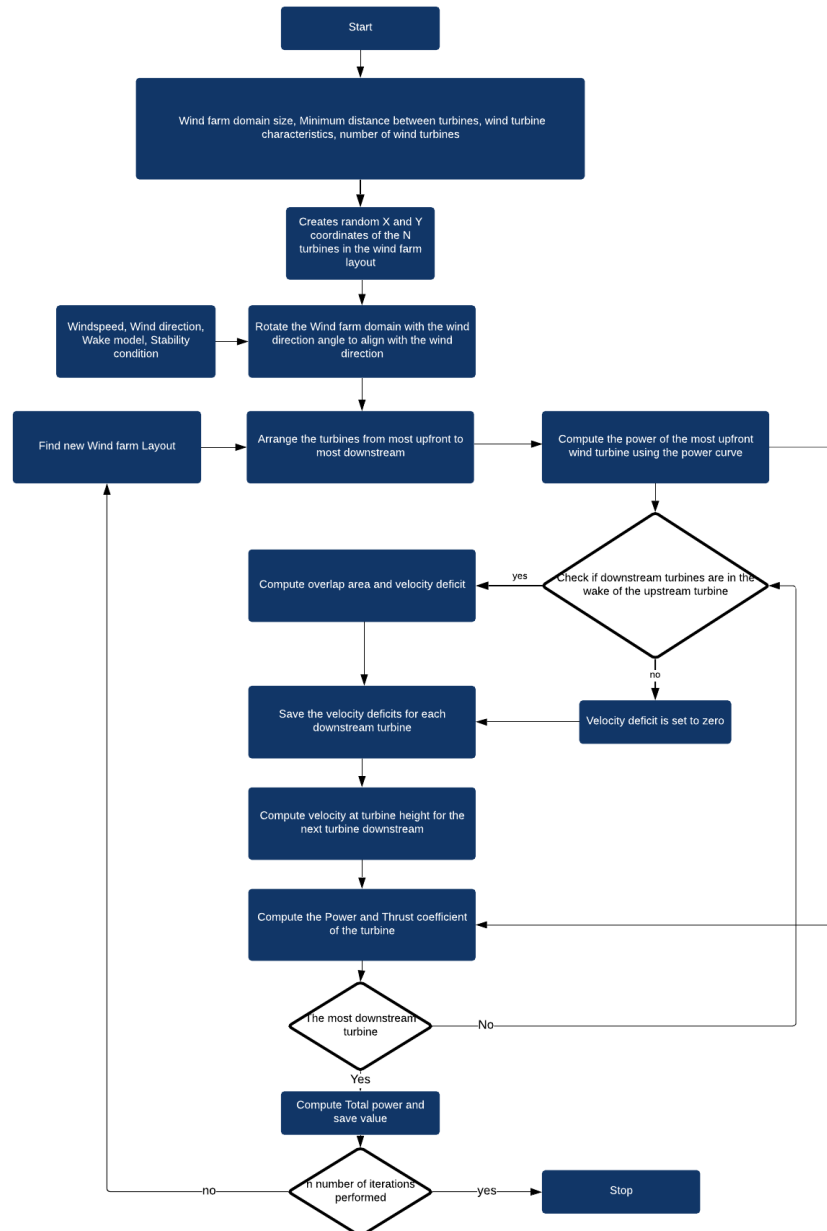


Figure B.1